CHARACTERIZING THE IMPACT OF ASYMMETRIES ON TROPICAL CYCLONE RAPID INTENSITY CHANGES

A Dissertation

Submitted to the Faculty

of

Purdue University

by

SaiPrasanth Bhalachandran

In Partial Fulfillment of the

Requirements for the Degree

of

Doctor of Philosophy

December 2018

Purdue University

West Lafayette, Indiana

THE PURDUE UNIVERSITY GRADUATE SCHOOL
STATEMENT OF DISSERTATION APPROVAL

Dr. Ernest Agee, Examination Chair

Department of Earth, Atmospheric, and Planetary Sciences

Dr. Daniel R. Chavas, Co-advisor

Department of Earth, Atmospheric, and Planetary Sciences

Dr. Frank D. Marks Jr., Co-advisor

Hurricane Research Division, NOAA/AOML

Dr. P. Suresh C. Rao

Department of Civil Engineering and Department of Agronomy

Approved by:

Dr. Linda S. Lee

Head, ESE Interdisciplinary Graduate Program

This dissertation and everything little success of mine that isn't on record is dedicated to my parents, my amma and appa.

ACKNOWLEDGMENTS

In the summer of 2014, a month before I landed at Purdue, my father contracted an illness for which we had no cure or explanation. I seriously began questioning the meaning of my pursuit of a Ph.D. when I should probably be staying home in India to look after my parents. Just before my prelims, there was yet another extreme shock that threatened to rock the boat. During these times, it was only because of my parents' personal sacrifices, repeated assurance, and unwavering support that I have been able to persist and pursue this Ph.D. till the very end. Thank you, amma and appa.

I would be lying if I did not acknowledge that it has truly taken a village to raise me. I cannot adequately express my gratitude to my research advisors: Frank and Dan, who took me under their wings and guided me to the very end. Every day, I reminded myself of the standards that Frank set for me and that was a prime motivation for me to push the boundaries of what I knew constantly. I cannot thank Dan enough for establishing a truly conducive environment for me to simply focus on science. His devil's advocacy has taught me to be cautious before jumping into conclusions; A much needed lesson.

My committee member, Suresh, was my first real introduction to trans-disciplinary science. From Suresh, I learnt to view the world through the lens of Complex Systems, and translate my understanding to systems other than Tropical Cyclones. I also benefited immensely from Ernie's wisdom during my committee meetings.

I also had the wonderful privilege of working with Ziad and Svetla from JPL. I am grateful for the way they embraced me as one of their own and provided me with an observational perspective. I am also thankful to the late T. N. Krishnamurti. I immensely benefited from his boundless wisdom during my visit to FSU and my

exchanges with him and his post-doc, Sarvesh, paved the way for a key portion of my thesis.

I will be ever grateful to Linda, the Head of my graduate program at Purdue (ESE). Her strength and support for the students of ESE are remarkable and have left an indelible mark on me. I can only hope to be a fraction of the human being that she is.

I wish to thank Gopal for introducing me to this field of tropical cyclones and rapid intensity changes; and for inviting me to HRD. I am grateful to the Indo-US Science and Technology Forum for initiating a working nexus between scientific communities in India and US. I've tremendously benefited from the collaborations that sprung from this. I wish to specifically thank Krishna, Raghu, and U. C. Mohanty for their collaborations. I am also grateful to Dev for accepting me into Purdue and for introducing me to a wonderful team of research mentors and collaborators.

I specifically wish to thank Rob Rogers, Gus Alaka, Mike Montgomery, Kerry Emanuel, Michael Riemer, Vijay Tallapragada, and Dave Ryglicki among others for taking the time out to respond to my calls and emails. They have all played a major role in my growth as a hurricane researcher.

My partner, Anamika, has offered me nothing but wholehearted support at every step of my journey. She was my emotional pillar when the going got really tough, my sounding board as we took breezy walks around the engineering fountain, and my design expert whenever I need to add an aesthetic finesse to one of my figures. I am also grateful to my band mates, my room mates, my lab mates, class mates, and teachers at Purdue for their wonderful company. I am also thankful to Christal and Deirdre from ESE, and Kathy and Stacie from EAPS for their administrative support. A special shout out to Matt Huber for his generous office space in which I've worked, slept, and played and experienced the best days of my Ph.D.

Finally, I acknowledge the gracious financial support of the Lynn Fellowship (2014-2015), the NASA Earth Science Fellowship (2015-2018), and the Bilsland Dissertation Fellowship (2018).

TABLE OF CONTENTS

Page

LIST OF TABLES . . . viii

LIST OF FIGURES . . . x

ABSTRACT . . . xix

1 PROBLEM INTRODUCTION . . . 1
1.1 Scientific Motivation . . . 1
1.2 Societal Implications . . . 7
1.2.1 Forecasting Challenges . . . 8
1.3 Case Study: Phailin and Lehar (2013) . . . 9
1.4 Objectives . . . 10

2 MODEL DESCRIPTION . . . 12
2.1 Numerical Simulation of TCs Phailin and Lehar (2013) . . . 13

3 SPATIAL DISTRIBUTION OF ASYMMETRIES . . . 16
3.1 Externally induced asymmetries . . . 25
3.1.1 Thermodynamic aspects . . . 26
3.1.2 Dynamic aspects . . . 34
3.2 Intrinsic asymmetries . . . 41
3.2.1 Thermodynamic aspects . . . 41
3.2.2 Dynamic aspects . . . 48

4 SPECTRAL CHARACTERISTICS OF ASYMMETRIES . . . 54
4.1 Power spectral Analysis . . . 54
4.2 Scale Interactions . . . 57
4.2.1 Generation of APE . . . 59
4.2.2 Conversion from APE to KE . . . 60
4.2.3 Mean to eddy kinetic energy transfer . . . 61
4.2.4 Eddy to eddy kinetic energy transfer . . . 63
4.2.5 Order of magnitude analysis . . . 65
4.3 Summary . . . 67
4.4 Appendix: Pertinent Equations for Scale Interactions . . . 69

5 PARSIMONIOUS DIAGNOSTIC MODELS . . . 79
5.1 Empirical model: Computation of the relative roles of factors influencing rapid intensity changes . . . 79
5.1.1 Background . . . 79

Page
5.1.2 Data 82
5.1.3 Low Wavenumber Reconstruction 85
5.1.4 Computation of Linear Discriminants and Projection on to Principal Component space 90
5.1.5 Results of the Discriminant Analysis 92
5.1.6 Generic markers and their relative importance 95
5.1.7 Discussions and Conclusions 99
5.1.8 A note on available observations and limitations 102
5.1.9 Future work 104
5.2 Stochastic model 105
5.2.1 Stochastic Model description 106
5.2.2 Results and Discussion 109

6 SYN-THESIS 113
6.1 Epilogue 114
6.2 Specific Recommendations 117
6.3 Future Work 120
6.4 Applicability to complex systems outside tropical cyclones 122

REFERENCES 124

VITA 136

LIST OF TABLES

Table Page

5.1 The selected list of tropical cyclones (TCs) over the Bay of Bengal. Also, the dates and times of initialization (cycles) of the TCs in the numerical model are provided. The length of each simulation was 72 hours. A 'case' constitutes a set of vortex and environmental state variables extracted from model outputs at an instance in time (say, t = t1) that precedes a rapid intensity change in the next 24 hours (From t1 to t1 + 24). In other words, for a 72-hour simulation, the intensity change between t1 + 24 and t1 is computed as t1 varies from the first hour to the 48th hour. If the magnitude of intensity change between t1 + 24 and t1 is greater than 30 knots, the case is selected for diagnosis. Thus, within the 33 simulations, there are 48 possibilities (33x48=1584 total possibilities) for a rapid intensity change. While we understand that there may be some overlap between the cases taken within a single TC for times that are close, each case still represents a unique combination of the state variables within the vortex and in the environment. 84

5.2 Details of the Weather Research and Forecasting model set-up. 85

5.3 List of variables after low wavenumber reconstruction. Notes: (i) The precipitation variable used here is a 2D variable (integral quantities for each grid cell). (ii) While the WN 0 represents the azimuthal average of a variable, the asymmetric representation of variables indicated as WN 0+1 are averaged in an azimuthal quadrant centered around the phase vector pointing towards the maximum or minimum WN1 asymmetry. (iii) The variables are either averaged within the radius of maximum wind (RMW), in the rain band region, within the entire vortex, or in the environmental annulus. 88

5.4 Covariance matrix of the final set of variables computed across all the 1000 training subsets. Here, the above serial numbers (1 - 10) stand for the below variables: 1. 350 - 200 mb (upper-level) horizontal wind divergence (environment) 2. WN 0 of rain within RMW 3. Angle of the driest air from the direction of shear (environment) 4. WN 0 of 1000 - 850 mb horizontal moisture flux convergence (within RMW) 5. WN 1 of 850 - 700 mb horizontal moisture flux convergence (rain band region) 6. Magnitude of environmental vertical wind shear 7. Number of convective bursts within the RMW 8. Phase overlap between WN 1 of inflow, vertical velocity and RH within the boundary layer (vortex) 9. WN 1 of rain (rain band region) 10. Angle of WN1 of rain in the rain bands from the shear direction (vortex)97

LIST OF FIGURES

Figure Page

1.1 Observational evidence of asymmetries in tropical cyclones. (a) Asymmetries in the inner-core of Hurricane Florence on 12th September 2018. Courtesy: Alexander Gurst, International Space Station. (b) Radar imagery showing the asymmetric distribution of Hurricane Maria as it engulfs Puerto Rico. Courtesy: Brian McNoldy. (c) Aircraft imagery of the organization of clouds in the inner-core of Hurricane Florence. Courtesy: Nick Underwood, NOAA, aboard P3. (d) GOES-16 imagery of the inner-core of Hurricane Michael taken on October 18th, 2018. Courtesy: NOAA GOES-EAST/NASA SPORT. 3

1.2 Schematic indicating a change in the state (characterized by variables such as intensity) of the TC vortex as a result of multiple external or intrinsic sources and sinks acting at each time. The schematic illustrates that there are multiple pathways possible for the TC vortex. The extremes viz. rapid intensification and rapid weakening are also highlighted. 5

1.3 Schematic illustrating that multiple convective organizations may lead to RI and RW at later times. Starting from isolated, asymmetric convection at individual clouds, depending on the sources and sinks, the spatial organization may be symmetric or asymmetric in nature and either of these configurations may result in intensification (the extreme being rapid intensification, RI) or weakening (extreme being rapid weakening, RW) making it a challenging problem. The block arrows indicate that the convective organization may transition between symmetric and asymmetric or between organized and disorganized scales during the life-cycle of a TC. 6

2.1 Comparison of model-simulated tracks (a) Phailin initialized at 12 UTC, 09 October 2013 and (b) Lehar initialized at 00 UTC, 26 November 2013. BOB: Bay of Bengal. 14

2.2 Time-series plot of intensity for (a) Phailin (initialized on 2013100912) (b) Lehar (initialized on 2013112600). The solid line represents the forecast from HWRF and the dots represent the best track intensities. The RI periods are shown as red, shaded periods; the RW periods are illustrated as blue, shaded periods and the landfall times are indicated as dashed lines. 14

Figure Page

2.3 Contrasting primary and secondary circulations and convective activities in Phailin and Lehar. (a, b) show the Hovmoller plots of azimuthally averaged tangential velocities (shaded) and radial velocities (contours). . . 15

3.1 (a, b) are plots of (vortex-removed) streamlines at 500 mb for Phailin and Lehar, showcasing the position of the subtropical high. (c,d) present a snapshot (t=24) of the environmental zonal wind, meridional wind, and the wind vector magnitude, computed at each level for Phailin and Lehar. The highlighted portion indicates the presence of an upper-level anticyclone (positive and clockwise tangential velocity) in Lehar's environment and the absence of it in the case of Phailin. (e,f) serve to compare the deep (200 - 850 mb) and mid (500 - 850 mb) bulk-shear values within the vortex (the winds at each level are first domain averaged in an 2°x 2° box) and in the environment (the vortex is removed and the domain averaging of winds at each level is done within an 8.5°x 8.5° box). 19

3.2 (a) Mean position of the subtropical high calculated from August to December as per climatology. Computed using ECMWF reanalysis. (b) Withdrawal isochrones of southwest monsoons in the year 2013 highlighting the delay in withdrawal during the lifetime of Phailin. Adapted from the publicly available withdrawal isochrones generated by the India Meteorological Department (c) Streamlines averaged between 200 - 400 mb from GFS indicating the position of the subtropical high during Phailin's time period and the position of the subtropical high for the other between years 1978-2016 computed using reanalysis. 20

3.3 ((a,b,c,d) Hodographs of winds computed within the vortex (domain averaged in an 2°x 2° box at each vertical level) and in the environment (domain averaged in a 8°x 8° box after vortex removal at each vertical level) for Phailin just before the RI (t=27) and for Lehar just before the RW (t=27). The shear magnitudes are vector differences between domain averaged winds computed at the vertical levels indicated. (e,f): Time series of vortex tilt (difference in circulation centers at various levels from the circulation center at 1.5 km) for Phailin and Lehar. 1 m/s = 1.943 knots. 22

3.4 (a,b) Plot of Geopotential heights at 300 mb for Phailin and Lehar, highlighting the pressure gradient in the meridional direction before the start of weakening and intensification. (c,d) Plots of 500-850 mb integrated specific humidity in g/kg. (e,f,) Plots of antecedent soil moisture (top-layer) in volume fraction (g,h) Plots of antecedent soil temperature (top-layer) (K) 24

Figure Page

3.5 Plan view of the near-surface θ_e (averaged within 2km from the surface) for Phailin (a) and Lehar (b) three hours prior to the start of the rapid intensity change. The four quadrants - downshear right (DSR), downshear left (DSL), upshear left (USL) and upshear right (USR) are marked in b. Figures c-f present the quadrant averaged, radial-height plots of θ_e for Lehar at t = 24. 27

3.6 Lehar's Azimuth-height plots of θ_e(shaded) and vertical velocity contours (updrafts in golden and downdrafts in black) at two times: t=24 (3 hours before RW) and t=27 (start of RW) (panels a, b respectively). Panels c and d show the corresponding azimuth-height curtains for radial velocity (shaded) and vertical velocities (contours) for Lehar at the same times. . . 28

3.7 (a,b) Radial flux of θ_e anomaly ($u\theta_e'$) within the boundary layer (vectors, colored according to θ_e' (azimuthal mean is subtracted) where blue indicates negative θ_e' and red indicates positive θ_e'). The θ_e' is averaged from the surface to 1.5 km in the vertical to represent the θ_e distribution within the boundary layer. Additionally, the downward flux of θ_e' (-1*$w\theta_e'$) through the top of the boundary layer (assumed to be at 1.5 km) is indicated as dashed contours. These plots are shown at two times: t = 24 (just before RW) and t = 27 (start of RW) and the shear vector is indicated by the black arrow. (c) Time-series of the magnitudes of $u\theta_e'$ and $w\theta_e'$ where a Heaviside function is used to ensure that only the inflow, downdrafts, and negative θ_e' are considered in the computation. The times when the the magnitudes of the vertical and radial fluxes of low θ_e peak together are highlighted and shown in the context of the timing of the rapid weakening. (d) Back-trajectories of low θ_e' (θ_e less than 342 K) air within 30 km radius. The radial extents for panels a, b, and d are 0 to 90 km. 29

3.8 Radius-height plots of the terms of the tangential momentum ($\langle v \rangle$) budget time-averaged during the initial period of Lehar's RW (24 - 36 hours). (a) Mean radial vorticity flux ($V_{m\zeta}$) (b) vertical advection of tangential momentum by the mean secondary circulation (V_{mv}) (c) the eddy radial vorticity flux ($V_{e\zeta}$), (d) the eddy vertical advection of tangential momentum (V_{ev}) (e) Residual terms (f) Net tendency in $\langle v \rangle$ over the period of interest. Units for all panels is $ms^{-1}h^{-1}$ and the contour intervals are 0.5 $ms^{-1}h^{-1}$. The dotted lines represent the $\langle v \rangle$ contours and the yellow dashed line represents the radius of maximum $\langle v \rangle$ at each height. 37

Figure Page

3.9 Lehar's plan view (r-θ) plots of (a) eddy relative vorticity (shaded) and radial velocity (contours, black represents inflow and golden represents outflow) averaged between 6-10 km (mid-levels) in the vertical, 0 - 120 km radius and 24-36 hours (b) Same as (a) except that the shading represents eddy moist entropy (θ_e). (c) is the same as (a) except that it is vertically averaged within the BL (0 - 2 km). (d) shows the plot of eddy moist entropy (shaded) and vertical velocity (dashed contours) within the BL. Highlighted, are the regions where the inflow carries the positive eddy vorticity (a) and negative eddy θ_e (b) in the mid-levels. Also highlighted is the region within the BL where the inflow contours are juxtaposed with negative eddy vorticity (c), negative eddy moist entropy and downdrafts (d).39

3.10 (a,b) Azimuth-height plots of Phailin's θ_e (shaded) and vertical velocities at t = 27 (six hours before the RI) and at t=33 (start of RI). Panels c and d present the azimuthal-averaged, radial-height cross-section of Phailin's radial velocities for the same times. Also highlighted are the radii of maximum winds at each height. 42

3.11 (a) Time-series plot of the 10-m radius of maximum winds (RMW) for Phailin. Highlighted, are times: 27 to 33 where there is an eyewall replacement cycle. (b) RMW computed at each height at various times as the storm intensifies. These Figures serve to illustrate the expansion of Phailin's RMW during its intensification. 43

3.12 Inward motion of Phailin's angular momentum surfaces as it intensifies. Radius-Height plots of azimuthally-averaged angular momentum at times t=27, t=36, t=60 hours. 45

3.13 Time-series plots (averaged in the azimuthal, radial and vertical directions) for Phailin. (a) Vertical Mass flux in kg/s (b) Inertial stability, I^2 within the radius of maximum winds (s^{-2}) (c) Static stability, N^2 within the radius of maximum winds (s^{-2}) (d) Generation of available potential energy (m^2s^{-3}) (e) Conversion from potential to kinetic energy (m^2s^{-3}). . 46

Figure Page

3.14 Plot of vertical velocities (shaded, in m/s) and equivalent potential temperature anomalies (contours, in K) highlighting the updrafts and downdrafts at the start of intensification (t = 33 hours) for Phailin and at the start of weakening (t = 27) for Lehar. The intense red spots indicate the vortex-scale deep convective updrafts. The moderate red regions indicate the moderate, mesoscale upward motion. The moderately blue regions indicate the downward motion. This Figure serves to illustrate the importance of the upper level configuration for the wrapping of convection. While the upper level configuration was conducive for the wrapping of convection in Phailin (a), the destruction of the upper level features due to shear in Lehar (b) do not allow for the development of these pockets of convection. 48

3.15 Radius-height plots of the terms of the tangential momentum ($\langle v \rangle$) budget time-averaged during the initial period (27 - 39 hours) of Phailin's RI. (a) Mean radial vorticity flux ($V_{m\zeta}$) (b) vertical advection of tangential momentum by the mean secondary circulation (V_{mv}) (c) the eddy radial vorticity flux ($V_{e\zeta}$), (d) the eddy vertical advection of tangential momentum (V_{ev}) (e) Residual terms (f) Net tendency in $\langle v \rangle$ over the period of interest. Units for all panels is $ms^{-1}h^{-1}$ and the contour intervals are 0.5 $ms^{-1}h^{-1}$. The dotted lines represent the $\langle v \rangle$ contours and the yellow dashed line represents the radius of maximum $\langle v \rangle$ at each height. 50

3.16 Phailin's plan view plots of (a) eddy relative vorticity (shaded, positive regions represent cyclonic direction) and eddy radial velocity (contours, black contours represent inflow and pink represents outflow) (b) eddy vorticity (shaded) and vertical velocity (contours, red contours represents upward motion). These plots are averaged between 4 and 12 km in the vertical for the RI period (27-39 hours) corresponding to Figure 3.15c. The dashed arrows highlight the regions of positive correlation between eddy inflow, cyclonic eddy vorticity and upward vertical velocity. Units of eddy vorticity are $10^{-4}s^{-1}$. 52

4.1 (a,b) Plot of Phailin's vertically integrated cloud-water mixing ratio (Q_r) at t = 15 during a disorganized phase (a) and at t = 72 during its peak intensity. (c,d) present a power spectra of Q_r as a function of wave number (WNs 1 to 180) corresponding to panels (a) and (b) averaged radially between 0-200 km (inner region) and 200-300 (outer rain band region). (e,f) show a power spectra of kinetic energy for the times corresponding to (c,d). The axes are plotted in a logarithmic scale to show the differences in the order of magnitude across the wavenumbers. 55

Figure Page

4.2 Time-series of the domain-averaged (up to a radius of 300 km, up to 20 km in the vertical) available potential energy (a,b) generated at axisymmetric mean (wavenumber 0), low order (wavenumber 1-2) and higher order wavenumbers (wavenumbers ¿2). (c,d) represents the conversion from available potential energy generated to kinetic energy. The left panels are for Phailin and the right panels are for Lehar. The RI period is shaded in red and the RW period is shaded in blue. The landfall time is marked by a dashed, gray line. 71

4.3 Phailin: Radius-height plots of the conversion from eddy potential to eddy kinetic energy for WNs 1,2 (a,c) and WNs 3 and higher (b,d). The RI and RW periods in Phailin correspond to the red shaded region in Figure 4.2c. 72

4.4 (Left) Radius-height plots of the barotropic exchange between the mean and low-wavenumber asymmetries for TC Phailin and Hurricane Harvey during their RI phases, and for TC Lehar during its RW phase. (Right) Corresponding plots of rainwater mixing ratio (in g/kg) to illustrate the symmetric or asymmetric nature of convection during the highlighted periods.73

4.5 Radius-height plots of the barotropic exchange between the mean and short scales (WNs 3 and higher) for TC Phailin (2013) during its RI and RW phase. 74

4.6 (a) Time-series plot of Phailin's (domain-averaged) rate of change of kinetic energy of long waves due to eddy-eddy interactions with the cloud scales. In this figure, an increase represents an upscale transfer of KE from short to long and a decrease represents a downscale transfer of KE from long to short. (b) and (c) Radius-height plots of the same quantity time-averaged during the Phailin's RI period (highlighted in red in (a)) and RW phase (highlighted in blue in (a)) respectively. 75

4.7 Time-series of the *net* change of KE in WNs 0,1,2,≥3 (blue, red, green and brown solid lines) in Phailin compared against the rate of change in intensity (black dashed line) over the course of its life-cycle. This figure serves to illustrate that due to the existence of multiple modes of energy exchanges that influence the KE at a particular scale, it is entirely possible that the energies at the mean and the eddies grow at the same time (t= 10 to 30 hours) or that the eddies grow at the expense of the mean (t = 65 to 75 hours). 76

4.8 Order of magnitude analysis for the various energy transactions over the course of TC Phailin's life-cycle. 77

Figure Page

4.9 Summary of the insights from scale-interactions during RI and RW phases. In this figure, the weight of the arrow corresponds to the magnitude of the energy exchange and the change in color and direction represents a change in the direction of transfer of energy. Double-sided arrows indicate that the energy transaction can be either way during RI and RW. 78

5.1 (a) Time series of intensity (maximum 10-meter tangential winds) for TCs Phailin and Lehar forecast by the model. The rapid intensification phase of Phailin and the rapid weakening phase of Lehar are denoted as 'RI' and 'RW' respectively. (b) Low wavenumber reconstruction of TC Phailin's intensity at t=12 (before the start of RI) used to identify the RMW, the rainband region, the bounds of the vortex, and the environmental annulus. (c) The horizontal cross-section of Phailin's radial wind averaged between the surface and 850 mb represented in storm-centric, cylindrical coordinates. (d) Same as (c) except that the asymmetric variable is reduced to its lowest wavenumbers. The shear vector and the phase vector of WN 1 are highlighted. 83

5.2 The percentage of variance in 10m tangential velocity (intensity) explained by azimuthal harmonics (wavenumbers) 1 to 10 for TC Lehar (2013) just before the start of its rapid weakening (t = 24, initialization: 2013112600). The computation is performed within a 3 x3 degree box around the center of circulation. This figure serves to illustrate that the majority of the eddy (wavenumbers greater than 0) variance is contained in wavenumber 1 and hence, the low wavenumber reconstruction is justified. Under rare scenarios, the percent of variance explained by the higher wavenumbers is much larger. Nonetheless, the idea is to simplify the complex asymmetric field into one symmetric (WN 0) and one asymmetric (WN 1) component. 89

5.3 (a) Coefficients of the linear discriminant analysis (LDA) performed iteratively using a 1000 different training sets chosen from the superset of cases and the *initial* variable list projected on to principal component space. (b) Same as (a) but using only the consistent variables (after the removal of outliers). 92

5.4 Results of the linear discriminant analysis. (a) Magnitude of discriminants computed for the RI and RW cases using only the vortex variables (b) Same as (a) except that the computation is done only using the environmental variables (c) Same as (a) except that the computation is done using both vortex and environmental variables together. The threshold (S) is marked by a horizontal line. Also highlighted are the estimated and true probabilities.93

Figure Page

5.5 Coefficients of the discriminants for the cases that projected on the extreme ends in PC space. The serial numbers of the variables correspond to Table 5.3. Highlighted, are the variables whose coefficients fluctuate several orders of magnitude when the training data subsets are varied. These highlighted variables are treated as outliers and are removed from the analyses hereafter. For the data analyzed here, the variables related to the environmental relative humidity were identified as outliers. 94

5.6 Same as Figure 5.5 except that at this juncture, the highlighted variables in 5.5 are removed. Note the immense reduction in axes bounds. A further round of screening is performed where the variables whose coefficients fluctuate in sign (but are still of same order of magnitude) when the training data subsets are varied. Finally, the covariance of the different variables was observed across the training period and a core of ten variables with little covariance amongst themselves, and whose magnitude and sign are consistent regardless of the chosen data subset are selected for further analyses. 95

5.7 (a) Bar graph showing the weights (results of the LDA) that represent the relative importance of the environment and vortex variables. The purple bars show the results of the computation when all the variables are taken together; the golden bars show the results of LDA when only the vortex variables are taken together, and the green bars show the results of LDA when only the environment variables are taken together. (b) Same as (a) except that the bars indicate the results of LDA when only the precipitation variables within the vortex are considered. 96

Figure Page

5.8 Demonstration of the selection of thresholds for the discriminant computed using coefficients averaged across the 1000 data subsets. Once the average coefficients are computed from the various subsets, the threshold (S) is varied between three standard deviations below to three standard deviations above. At each threshold, the estimated versus true probabilities of RI and RW for the mean discriminant are computed for all the cases. The threshold that produces the best combination of true positives and true negatives is selected. (a) Plot of the probabilities of the correct diagnosis of RI (true positives, pr (estimated RI — true RI)) for various thresholds. (b) Plot of probabilities of correct diagnosis of RW (true negatives, pr (estimated RW — true RW)) for various thresholds. (c) Plot of probabilities of correct diagnosis of RW (x-axis) versus probabilities of correct diagnosis of RI (y-axis) (d) Plot of probability of incorrect diagnosis of RI (false negative, pr (estimated RI — true RW)) versus probability of correct diagnosis of RI (true positive, pr (estimated RI — true RI)). The dashed regions and lines serve to illustrate that a threshold of 0.9 yields the best combination of true positives (91 percent) and true negatives (96 percent) corresponding to Figure 5.4c (all variables taken together). . . . 98

5.9 Simulations of aggregate kinetic energy (sum of kinetic energy across all wavenumbers; spatially averaged through the depth of the vortex and between 0-300 km radii) for (a) Phailin (b) Lehar. The gray lines represent individual realizations with the addition of stochastic forcing. The dashed, red line represents the aggregate kinetic energy computed without any stochastic addition. 111

5.10 A violin plot of the probability density function (PDF) of aggregated KE (across all ensembles) at each time. The red dots indicate the median of the PDF at each time. 112

ABSTRACT

Bhalachandran, SaiPrasanth Ph.D., Purdue University, December 2018.
Characterizing the Impact of Asymmetries on Tropical Cyclone Rapid Intensity Changes. Major Professors: Daniel Chavas, Frank Marks Jr.

A tropical cyclone (TC) vortex is an immense, coherent, organized-convective system. Beneath this large-scale organization, are a multitude of azimuthally asymmetric convective motions that exist on a spectrum of scales. These asymmetries are especially dominant during periods when the vortex undergoes critical transitions in its intensity and structure. However, the precise nature of influence of the organization of asymmetries on TC intensity change remains an enigma. The inherent difficulty in predicting their behavior is because asymmetries may arise due to different external or intrinsic sources and occur at different spatial and temporal scales while several complex mechanisms act near-simultaneously to dictate their evolution in time. As a result, multiple pathways are possible for a TC vortex that is influenced by these asymmetries. Our preliminary investigations using numerical models made it apparent that there wasn't a single, unifying way to address this problem. In this thesis, I outline multiple novel techniques of diagnosing and predicting which of the many pathways are likely for a TC vortex that is influenced by azimuthal asymmetries.

First, using three-dimensional numerical simulations of a pair of sheared and non-sheared vortices, I demonstrate the diagnostic potential of the juxtaposition in the azimuthal phasing of: (i) the asymmetrically distributed vertical eddy flux of moist-entropy across the top of the boundary layer, and the radial eddy flux of moist-entropy within the boundary layer; and (ii) eddy relative vorticity, eddy moist-entropy, and vertical velocity throughout the depth of the vortex.

Second, I introduce an energetics-based diagnostic framework that computes the energy transactions occurring at asymmetries across various length-scales in the wavenum-

ber domain. By applying it to select cases, this thesis uncovers the relative importance of all the energy pathways that support or disrupt the growth of asymmetries within the vortex. Contrary to the traditional explanations of convective aggregation/disaggregation and axi/asymmetrization through barotropic mean-eddy transactions, my thesis reveals that the growth or disruption of asymmetries are predominantly due to (i) the baroclinic conversion from available potential to kinetic energy at individual scales of asymmetries and (ii) the transactions of kinetic energy across asymmetries of different length scales.

Finally, this thesis introduces two further diagnostic frameworks targeted at tackling the problem of real-time forecasting of TC rapid intensity changes. The first is an empirical framework which examines symmetric and asymmetric convection and other state variables within the vortex, and in the environment across a suite of TCs and identifies a set of 'important' variables that are significantly different during time periods that precede a rapid intensification as opposed to a rapid weakening. My framework then ranks the variables identified based on how significantly they influence a rapid intensity change in a TC and the amplification factor of any associated variability. We recommend that future observational, and consequent TC modeling and data assimilation efforts prioritize the highest ranked variables identified here.

The second is a stochastic model wherein a scale-specific stochastic term is added to the equations describing the energy transactions within the TC vortex. By simulating a stochastic forcing that may arise from any scale, I compute the probability of the vortex transitioning into a rapidly intensifying or a rapidly weakening configuration across an ensemble of scenarios.

In summary, this thesis introduces and applies a variety of diagnostic techniques that help determine the impact of azimuthal asymmetries on TC intensity evolution.

1 PROBLEM INTRODUCTION

1.1 Scientific Motivation

Let's begin where a mathematically inclined humorist once left off. With a *spherical* cow. While the phrase was originally intended to take a dig at oversimplification and reductive fallacy, it also captures the essence of how we go about attempting to understand complex phenomena in nature. In fact, without toy-models, zeroth-order approximations, and parsimonious physics, we would often not know where to begin. However, the societal, engineering and economic implications of such complex natural phenomena demand that we do the best we can no matter the inadequacy in our current state of knowledge. For example, if fluid dynamicists waited until they solved turbulence, no airplanes would fly, and no weather would be forecast [1].

Tropical Cyclones (TCs) are examples of such naturally occurring complex systems that have captivated and confounded scientists and forecasters for decades. TCs are large-scale, organized convective phenomena that emerge from energy exchanges between three major complex systems: the atmosphere, ocean, and land. What we see as the immense, coherent structure of a TC is really a manifestation of highly complex, nonlinear dynamical processes at and across multiple spatial and temporal scales. For this reason, even today, forecasting TC characteristics such as intensity (defined by the National Hurricane Center (NHC) as the *maximum* near-surface wind magnitude), trajectory, and vortex-structure (flow field in three dimensions) is a challenging task [2–5].

As a first step, researchers began by modeling the TC as a vortex with a ***horizontal symmetric circulation about a central axis*** (referred to as the primary circulation) on which is superimposed a transverse (secondary) circulation. The transverse circulation comprised of air parcels that spiraled inward at low-levels picking

up energy from the warm ocean, elevated upwards and then diverged outwards at the upper-levels [6]. While the framework was insightful in describing a few fundamental components of TCs [7], it was certainly simplistic as it only described the first-order behavior of TCs. Advancements in airborne radar technologies [8,9], satellite remote sensing [10], and high-resolution 3D modeling [11–13], have revealed that strong *azimuthal asymmetries* (hereafter, just asymmetries) are inherent to the flow evolution of the TC vortex (Figure 1.1). These asymmetric features are typically present during all phases of a TC's life cycle and are most predominant every time a TC undergoes a significant change in its organization of convection (e.g., genesis, rapid intensity changes, and landfall) [12]. Given these recent advancements and the existing bed of axisymmetric theories, it is important to understand if the accounting of additional asymmetric effects can improve the predictability and our fundamental understanding of TC behavior. If so, to what extent and at what cost?

Asymmetries may arise via two distinct pathways: (i) asymmetries generated when the vortex comes in contact with an external source such as environmental vertical wind shear (hereafter "shear") or land interactions (ii) asymmetries generated via the intrinsic, vortex dynamics itself. To a good approximation, the TC vortices on a *system-scale* [1] exist in balance with the environment (thermal wind balance). When the vortex encounters a significant change in the environmental flow-field, a series of dynamic-thermodynamic readjustments take place within the vortex in an attempt to nudge the vortex back in balance with the environment [14,15]. These readjustments reflect as coherent asymmetries in the flow field, moist-entropy, and convection within the vortex.

On the other hand, even without the external influence, prior research has shown the existence of several *local*, intrinsic asymmetric features within the TC vortex. These are a result of instabilities on multiple scales, i.e., baroclinic, barotropic, convective, etc. For example, deep, isolated moist-convective updrafts that cover

[1]The boundary layer and regions within the inner-core are examples of regions that are not in gradient wind balance due to the dominance of friction and diabatic forcings.

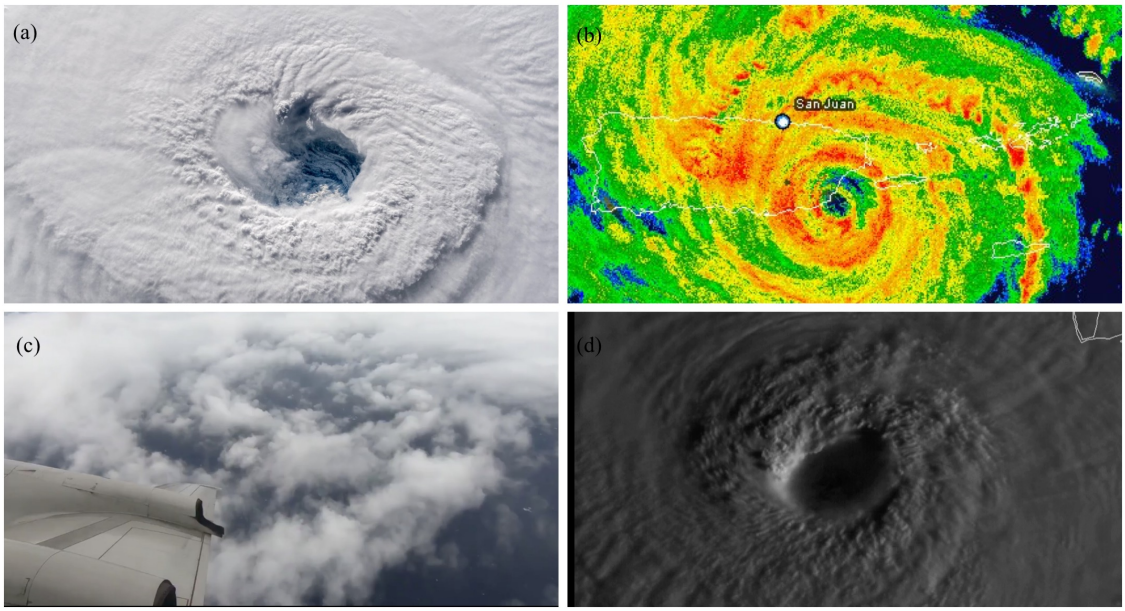

Figure 1.1. Observational evidence of asymmetries in tropical cyclones. (a) Asymmetries in the inner-core of Hurricane Florence on 12th September 2018. Courtesy: Alexander Gurst, International Space Station. (b) Radar imagery showing the asymmetric distribution of Hurricane Maria as it engulfs Puerto Rico. Courtesy: Brian McNoldy. (c) Aircraft imagery of the organization of clouds in the inner-core of Hurricane Florence. Courtesy: Nick Underwood, NOAA, aboard P3. (d) GOES-16 imagery of the inner-core of Hurricane Michael taken on October 18th, 2018. Courtesy: NOAA GOES-EAST/NASA SPORT.

only a small portion of the inner-core were shown to contribute to a majority of the upward mass transport [16]. These updrafts were christened "vortical hot towers" [13, 17–19]. The emergent collective understanding from recent studies on this topic is that the changes in intensity and structure are strongly influenced by the dynamics of asymmetries, rather than the gradual change associated with axisymmetric circulations [12,16,18,20]. The gradients associated with the asymmetric distributions within the vortex further result in eddy fluxes and wave asymmetries that serve to redistribute various quantities such as vorticity, momentum, moist-entropy [21–25]. Ultimately, the dominance of the intrinsic or externally-induced asymmetries is a function of the strength and nature of the environmental flow field; and the vortex's resilience to an external forcing.

Asymmetries are generated and can exist at a multitude of spatial and temporal scales. The convective entities within a TC vortex range from individual clouds (length scales ≤ 5 km) to coherent, mesoconvective entities organized at length scales of the order of hundreds of kilometers [2, 26]. The mesoconvective vortical structures are essentially the result of individual deep convective cloud elements organized with other cloud elements along the azimuth. The behavior of these mesoscale entities can be drastically different from an individual cloud [27]. The mesoconvective entities are associated with larger spatial and temporal scales while the individual convective entities are more transient and stochastic in nature [28].

Asymmetries have traditionally been believed to be associated with the *weakening* of TCs [29–31][2]. However, recent studies [31–33] have shed light on the fact that

[2]Recall that by definition, asymmetries are the deviation from the (azimuthal in this case) mean field. For example, following a Reynolds' decomposition, $u = \bar{u} + u'$, where $\bar{u}$ represents the azimuthal mean, u' represents the deviation from the mean, and u represents the velocity vector at a given point in radius, azimuth (r, θ) space. The growth of the asymmetries may be perceived as growth at the *expense* of the mean, so it may be intuitive for some to associate asymmetries with the weakening of the TC. Note that this is analogous to a socialist viewpoint where *given a fixed, limited amount of resources*, the growth of an individual is seen as growth at the expense of others. Alternatively, a capitalist viewpoint (that does not view the net amount of resources as fixed) is that if every individual grows, then the *net amount of resources* increases and this need not be viewed at the expense of others. Likewise, the growth of asymmetries (u') may also contribute to the increase in the net quantity of a field (u) even if the mean field ($\bar{u}$) does not grow. It is important to remember that intensity, as per NHC definition, is the *maximum* near-surface tangential wind. Not the mean

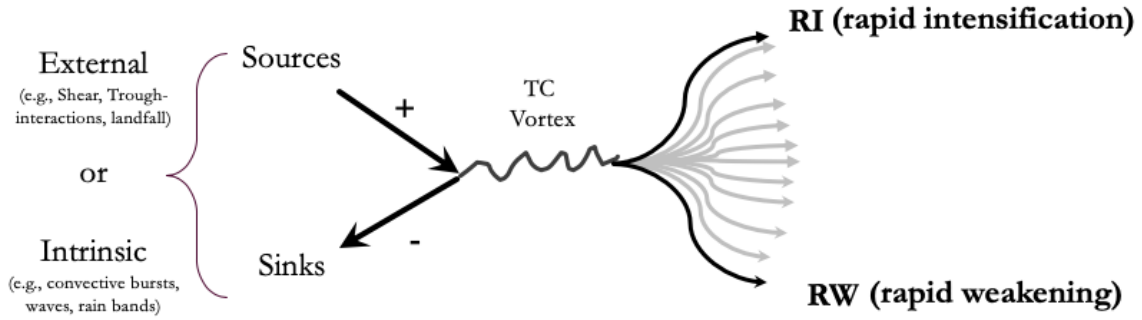

Figure 1.2. Schematic indicating a change in the state (characterized by variables such as intensity) of the TC vortex as a result of multiple external or intrinsic sources and sinks acting at each time. The schematic illustrates that there are multiple pathways possible for the TC vortex. The extremes viz. rapid intensification and rapid weakening are also highlighted.

asymmetries can have a positive or negative role towards TC intensity changes. A natural question that follows such a conclusion is: What are the scenarios under which asymmetries act to positively influence a change in TC intensity and what are the alternative scenarios under which they aid in the demise of the TC? Such an enigma exists because asymmetries can arise from different sources, occur at different spatial and temporal scales, and their evolution in time is influenced by several mechanisms occurring nearly simultaneously. As a result, when such asymmetries are present within the TC vortex, there are multiple possible pathways for the TC vortex (Figure 1.2) and many configurations that can result in either intensification or weakening (Figure 1.3). At present, minimal work has been done to understand these details of asymmetries. My current research seeks to bridge this gap in our understanding and investigate the various aspects of asymmetries through multiple lenses and examine their impact on TC intensity changes.

tangential wind. By this reasoning, we may begin to see that asymmetries need not act to weaken the intensity. Disclaimer: This does not reflect my personal political views.

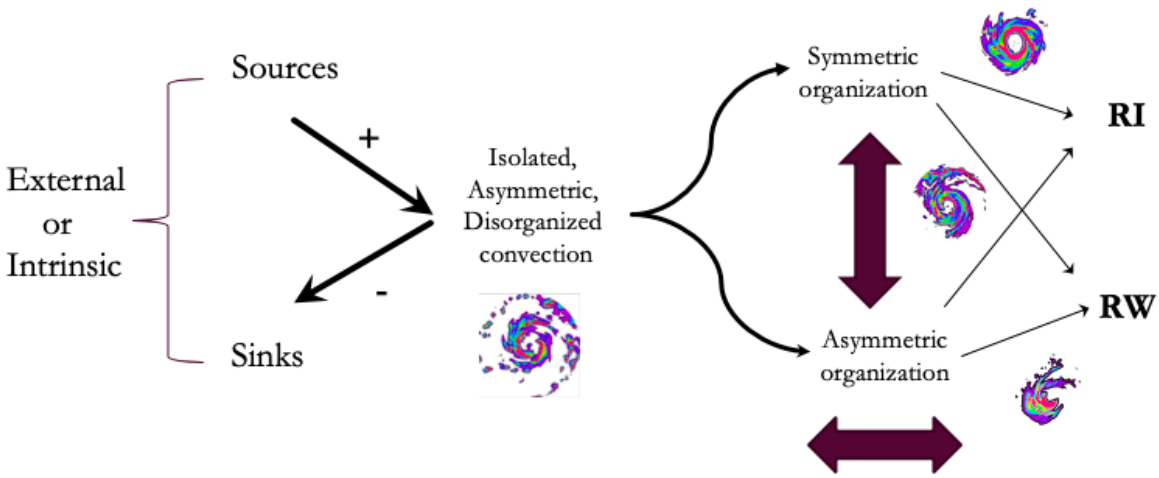

Figure 1.3. Schematic illustrating that multiple convective organizations may lead to RI and RW at later times. Starting from isolated, asymmetric convection at individual clouds, depending on the sources and sinks, the spatial organization may be symmetric or asymmetric in nature and either of these configurations may result in intensification (the extreme being rapid intensification, RI) or weakening (extreme being rapid weakening, RW) making it a challenging problem. The block arrows indicate that the convective organization may transition between symmetric and asymmetric or between organized and disorganized scales during the life-cycle of a TC.

1.2 Societal Implications

The Bay of Bengal basin is distinct from its Atlantic or Pacific counterparts in that the ocean is warmer [34, 35], less deep, and smaller in size. As a result, the atmospheric environment plays a dominant role in dictating TC behavior [36]. TCs over the Bay of Bengal are known to experience vastly different environments within a relatively short period of time [37]. As a result, we expect that the TC vortices in this region will be good case studies for the investigation of externally-induced as well as intrinsic asymmetries. In addition to the scientific motivation, there is a strong societal motivation to focus on TCs across the Bay of Bengal.

The east coast of India is extremely vulnerable and disaster-prone to a variety of threats such as tropical cyclones, heatwaves, floods, and droughts. The recurrent nature of these shocks has significantly impeded the capacity of the coastal communities to recover from these threats. Of these disasters, TCs are the most impactful [38] and pose a grand challenge to the forecasting and disaster response teams.

The TC season over the Indian Monsoon region has two peaks annually pre-monsoon (April-May) and post-monsoon (October to early December). The post-monsoon season is known to be susceptible to more intense TCs [39]. Annually, the Bay of Bengal is hit by four to six TCs with two to three of them turning very severe ($\geq$ 64 knots). Since the Bay of Bengal basin is relatively small in size, intense TCs take only about 3-4 days to reach the land [40]. As per the recent census, approximately 370 million people across a coastline of over 8000 km are exposed annually to TC related risks in India [38]. Unfortunately, the rate of increase in coastal vulnerability is far greater than the rate at which our ability to predict TCs in advance is advancing [4, 41]. Additionally, an increase in the number of severe cyclones in the post-monsoon season over the Bay of Bengal of 65 percent (in the period between 1950-2012) was noted in a recent study [42]. With increasing severity of the approaching TCs, increasing vulnerability of the coastal population, and given that TCs over the Bay of Bengal only take two to three days to turn severe, the

need for improved prediction and communication of the potential risks associated with TCs in advance is stronger now more than it has ever been. Early and accurate forecasts and warnings can help prepare disaster response teams in advance and save thousands of lives and property, and every step towards an improved fundamental understanding of the mechanisms driving these intensity changes goes a long way in ensuring the same.

1.2.1 Forecasting Challenges

There are at least four major components to the TC forecasting problem: forecasting (i) the track, (ii) intensity, (iii) rainfall, and (iv) surge. Of the above, the prediction of the TC's intensity is arguably the most challenging [43]. This is because a change in a TC's intensity is the result of various dynamical and thermodynamical processes interacting at and across multiple scales through the depth of the troposphere. These processes range from the large-scale circulations in the TC atmospheric environment, the mesoscale organized convective processes at the vortex-scale, down to the sub-grid scale microphysical processes [2, 4, 5, 28, 44]. Accurate forecasts of a TC's intensity requires an integration of satellite and aircraft observations with numerical models that are initialized with the help of such observations. However, there has been relatively slow progress in our understanding of TCs over the Indian Monsoon Region compared to the other basins, due to the geography, economic constraints, and lack of sufficient observations [41, 45].

Rapid intensity changes in TCs are a special subset of the already baffling intensification problem where forecasting failures are more likely and can have dire consequences. They comprise of Rapid Intensification (RI) and Rapid Weakening (RW) and are defined as an intensity change of ± 30 knots or greater within 24 hours [36, 46, 47]. Rapid intensity changes has been the subject of focus for several major organizations including the World Meteorological Organization (WMO) [48], the Hurricane Research Division (HRD/NOAA) [4], the India Meteorological Division (IMD) [49],

and NASA [50, 51]. Recent initiatives by the Governments of India and the United States led to a collaborative agreement and the formation of the Indo-US Science and Technology Forum (IUSSTF). Such a venture has triggered collaborations amongst universities, scientists, and forecasters in India and the US, creating an opportunity for a region-specific study that addresses rapid intensity changes in TCs over the Bay of Bengal.

1.3 Case Study: Phailin and Lehar (2013)

During the early hours of 10 October 2013, Tropical Cyclone (TC) Phailin began rapidly intensifying across the Bay of Bengal (BoB). Over the next 24 hours, there was an increase in maximum surface wind speed from 45 knots to 115 knots (23.15 m/s to 59.1 m/s) and a central pressure drop from 996 hPa to 940 hPa. Phailin's rapid deepening presented a major challenge to the response teams as a massive evacuation of approximately a million people had to be coordinated [52]. Only six weeks later, TC Lehar reached an intensity of 75 knots (38.5 m/s, Very Severe Cyclonic Status) and concerns similar to Phailin were raised as the storm approached land. However, over the next 18 hours, Lehar went on to weaken rapidly to ∼30 knots, well before landfall. Such contrasting rapid changes in TC intensity are a nightmare to forecasters and policymakers. When evacuations of this scale are at stake, erring on the safe side is not a welcome option since false alarms tend to reduce the credibility of the forecasts and subsequent response from the public.

In the aftermath of these storms, the details of the mechanisms and processes that resulted in such contrasting behavior within a period of five to six weeks remained unclear. How different were the environments experienced by the two TCs? And how did that impact the vortex-scale symmetric and asymmetric convective organization? What were the relative roles played by the external environment and the intrinsic vortex dynamics? These are some of the questions that will be investigated in this thesis with Phailin and Lehar as the case study of interest.

The broader impact of the findings presented herein includes the translation of the understanding obtained here to the scientific and forecasting teams in the form of timely and reliable products (R20 or Research to Operations) and decision support tools that guide scientists in providing early warnings (guidance-on-guidance) in disaster-prone regions.

1.4 Objectives

This work seeks to achieve the following objectives:

(i) Examine the various spatial, spectral, and temporal characteristics of convective asymmetries in TC vortices and outline the different means to diagnose and potentially predict their impact on TC vortex-scale rapid intensity changes.

(ii) Quantify the relative importance of the various energy pathways that support or disrupt the growth of asymmetries within the vortex during periods of rapid intensity changes.

(iii) Quantify the relative importance of symmetric and asymmetric convection within the vortex in the context of other intrinsic and external state variables that precede or lead to rapid intensity changes.

Chapter 2 describes the Hurricane Weather and Research Forecasting (HWRF) model that is used in this study. Using the case-studies of Phailin and Lehar, Chapter 3 explores the question: What determines the spatial distribution of externally-forced and intrinsic convective asymmetries within a vortex and how does that impact the TC intensity? This is addressed for a thermodynamical as well as dynamical standpoint. Using the same case-studies as Chapter 3, Chapter 4 investigates the energetics of asymmetries at different spatial and temporal scales in spectral space.

From a real-time forecasting standpoint, there is also the challenge of the large dimensionality of the problem. Present-day TC forecast models and observations provide high-resolution information in four dimensions - radius (r), azimuth (θ), height

(z), and time (t), and it is important to segregate the most essential information that is relevant to our specific task of diagnosing the impact of asymmetries on RI and RW. To tie it all back to where we began, we may recall Einstein's classic message: 'Everything should be made as simple as possible, *but no simpler*'. With our evolving knowledge, we are continually evaluating how the various puzzle pieces fit together and asking ourselves: What is the simplest manner in which I can approach this problem and at the same time, not oversimplify the problem such that the essence is lost? With this objective, Chapter 5 focuses on parsimonious diagnostic techniques applied to a suite of TCs aimed at reducing the problem dimensionality whilst retaining just the most critical information required to estimate the probability of critical transitions in TC vortices to considerable accuracy. Chapter 6 concludes with a synthesis of the key findings and their implications across all chapters, lists recommendations, and explores future opportunities.

2 MODEL DESCRIPTION

The Hurricane Weather and Research Forecasting Model (HWRF) is the model using in this thesis. HWRF is the operationally adopted, 3D (non-axisymmetric), near cloud-resolving framework, that allows us to disentangle and visualize the impact of the processes of interest associated with TCs [53]. Simulations are performed using HWRF v3.5 that has three nested domains with 27, 9, and 3 km grid-spacing respectively. There are 43 vertical levels, including 11 levels below 850 hPa for adequate resolution of the hurricane boundary layer. The model is non-hydrostatically mapped on a rotated latitude-longitudinal, Arakawa E-staggered grid with a storm centered hybrid (sigma-p) coordinate in the vertical direction. This model was developed by the National Centers for Environmental Prediction (NCEP) and the Hurricane Research Division (HRD) and is annually updated. Recent updates include improved surface and microphysics schemes and a new shallow convective parameterization scheme. The combination of Geophysical Fluid Dynamics Laboratory (GFDL) surface physics, Slab (thermal diffusion) model, a simplified Arakawa-Schubert scheme for cumulus parameterization, and Ferrier cloud microphysics along with GFS planetary boundary layer scheme is used here. Further details can be found in Tallapragada et al. (2015) [53]. The initial and boundary conditions come from the Global Forecast System (GFS) model.

The outer-domain simulation of HWRF is used to study the large-scale features and the inner-domain outputs are used to observe vortex-scale and local convective scale features. The HWRF outputs for the high-resolution, inner-domain simulations are then transformed to a storm-centric, cylindrical coordinate system (using a monotonic bi-cubic interpolation) with a grid spacing of $\Delta r = 1$km and $\Delta\theta = 1\,\mathrm{deg}$. We use a surface-minimum pressure centroid at each time to calculate the center of the

cylindrical coordinate system. The radial extent of the transformed inner domain was 300 km.

At this juncture, it is also important to define and differentiate the vortex and the environment. Such a delineation has been a subject of several studies in the past and continues to be an elusive problem in TC research [54, 55]. In this study, the environment is defined as the region beyond the radius at which the 10-m tangential wind drops below 8 m/s (Note that as per IMD's definition, the minimum wind speed that qualifies as a weak depression is 8.75 m/s or 17 knots). Alternatively, we use an adapted version of Kurihara's filter [56] to remove the vortex from the flow field. The notable difference between our method and Kurihara's being the use of 10m winds, as opposed to the 850 mb winds in the original documentation. Approximately, 200 passes of the filter were required to remove the vortex from the environmental field.

2.1 Numerical Simulation of TCs Phailin and Lehar (2013)

HWRF simulations of Phailin and Lehar were performed (details in the Methods section) with GFS initial conditions that provided the best forecast and captured the rapid changes in intensity (12 UTC, 9 October 2013 for Phailin, and 00 UTC, 26th November 2013 for Lehar). Figure 2.2 compares the HWRF simulations of Phailin and Lehar against observations from Indian Meteorological Division (IMD). The vortex initialization was provided by Joint Typhoon Warning Center (JTWC) TC Vitals.

Figure 2.2 underscores Phailin's RI between 24 - 60 hours simulation time and Lehar's RW between 27 - 51 hours. Both of these rapid intensity changes were over the ocean. Phailin made landfall with an intensity of 120 knots and its rapid decay began six hours post-landfall. Figure 2.3 shows the Hovmoller (Time-radius) plots of the azimuthally-averaged 10-m tangential and radial wind. The rapid intensification of Phailin is evidenced by the strengthening of the tangential winds with time, which is accompanied by an increase in the inflow (Figure 2.3a). The RW of Lehar is illustrated by the weakening of the tangential winds after 24 hours (Figure 22.3).

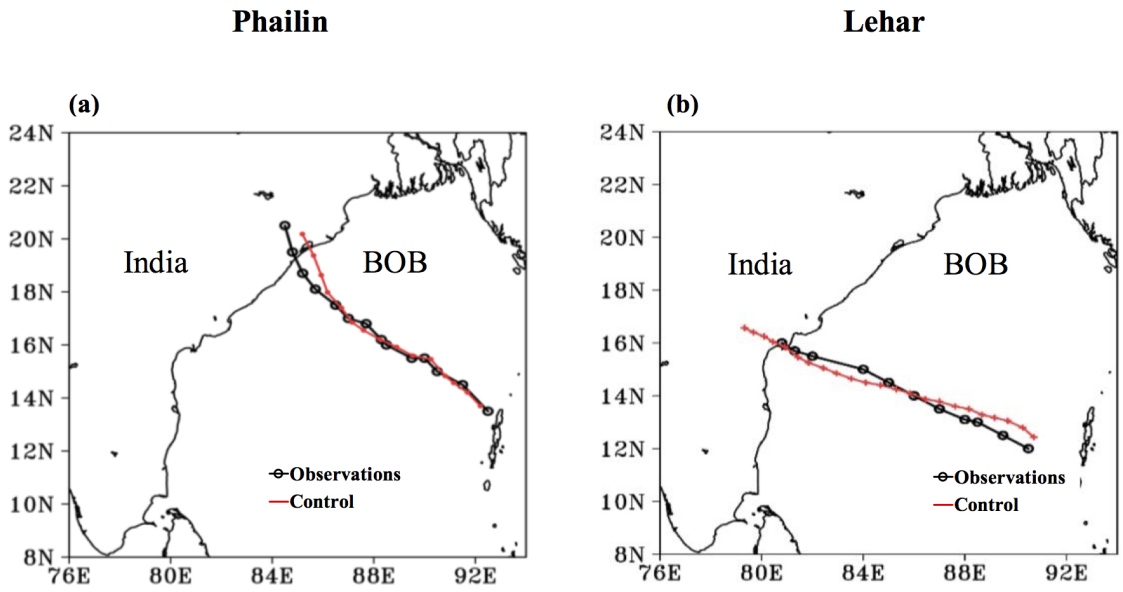

Figure 2.1. Comparison of model-simulated tracks (a) Phailin initialized at 12 UTC, 09 October 2013 and (b) Lehar initialized at 00 UTC, 26 November 2013. BOB: Bay of Bengal.

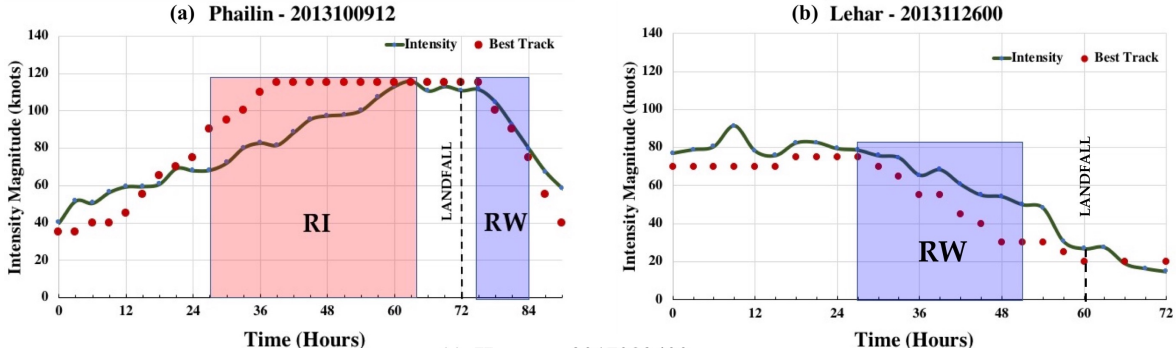

Figure 2.2. Time-series plot of intensity for (a) Phailin (initialized on 2013100912) (b) Lehar (initialized on 2013112600). The solid line represents the forecast from HWRF and the dots represent the best track intensities. The RI periods are shown as red, shaded periods; the RW periods are illustrated as blue, shaded periods and the landfall times are indicated as dashed lines.

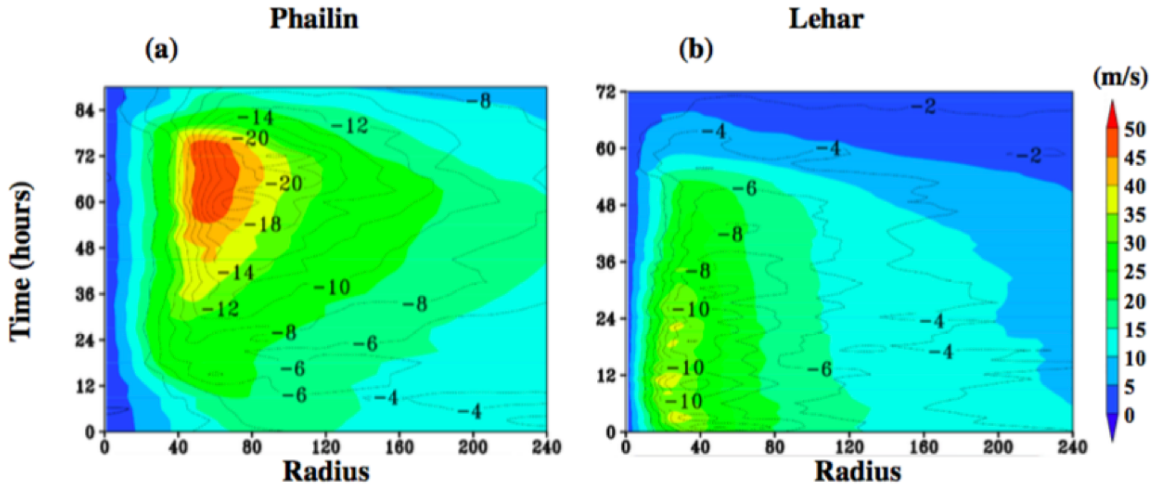

Figure 2.3. Contrasting primary and secondary circulations and convective activities in Phailin and Lehar. (a, b) show the Hovmoller plots of azimuthally averaged tangential velocities (shaded) and radial velocities (contours).

While the inflow is seen to peak at about 72 hours in the case of Phailin, the inflow weakens after peaking during the first 24 hours in the case of Lehar (maximum mean tangential winds 38 m/s or 75 knots). In the case of Phailin, the increase in the radial and tangential winds are nearly simultaneous. While a similar behavior is observed in the case of Lehar for the first 24 hours, the tangential component weakened quicker than its radial counterpart.

In the following chapter, the spatial (symmetric and asymmetric) convective organization in Phailin and Lehar will be examined in the context of their respective large-scale environments.

3 SPATIAL DISTRIBUTION OF ASYMMETRIES

(A version of this chapter is published in Scientific Reports)

What dictates the symmetric or asymmetric distribution of convection within a TC vortex? What is the consequent impact of the convective organization on the TC intensity change? These are the questions that are the primary focus of this chapter.

Convection is a transient phenomena [12]. The sustenance and growth, or disruption of convection is a function of the local environment within the vortex, i.e., the vertical profiles of the moist-entropy and wind in which it is embedded. These local environments are modulated by the large-scale (atmospheric, oceanic, and land surface when applicable) environmental conditions [57,58]. Furthermore, convection acts to transport the mass, momentum, and moist-entropy from the near-surface regions to the upper-portions of the vortex. The mass flux transported directly impacts the near-surface radial pressure gradient and influences the radial and tangential winds above and within the boundary layer. As a result, the spatial organization in convection is strongly linked to the intensity changes [43].

When a TC vortex encounters significant changes in its environmental flow field (e.g., when it experiences shear), internal instabilities are triggered and there is a subsequent readjustment of various dynamic-thermodynamic fields. Past numerical [14, 59] and observational examinations [60, 61] of sheared vortices have revealed that when the vortex tilts downshear, a series of thermal and vertical motion anomalies occur to restore thermal wind balance (upward motion and cold anomaly downshear, and downward motion and warm anomaly upshear). In essence, shear establishes the preferred azimuthal location of convection such that the updrafts are predominant in the downshear quadrants and the downdrafts are dominant in the upshear quadrants [59,62–64]. In addition to shear, the storm motion magnitude and direction [65,66], as

well as air-sea temperature and moisture disequilibrium, may also act simultaneously to influence the radial and azimuthal distribution of convection [67–70].

With constant feedback from the vortex to the environment, the environment also evolves in parallel with the TC vortex. While TCs have traditionally known to weaken in a sheared-environment, recent studies [32, 59, 71–74] have articulated different possibilities of how TCs can intensify in a sheared environment. Under such scenarios, the surrounding moist entropy, vortex resiliency, depth of the vortex, stage of the storm, storm motion vector, and the vertical structure of shear, all help in ultimately determining the fate of the storm.

This chapter will focus on aspects of asymmetries induced externally as well as intrinsically within the vortex. As a first step, a comparison of the evolution of the large-scale environments experienced by Phailin and Lehar is presented. Next, the dominance of externally-induced asymmetries in Lehar's vortex due to shear-vortex interactions and the lack of thereof in Phailin is highlighted. The remaining portions of this chapter focus on the thermodynamic and dynamic aspects of the (a)symmetric convective organization and how they impact the TC's intensity evolution.

Comparison of TC environments for Phailin and Lehar

Figure 3.1 compares the large-scale environmental winds of Phailin and Lehar at the times when the storms began to diverge in their intensities. The plot of 500 mb streamlines (vortex-removed) at t = 27 (start of RI) for Phailin (Figure 3.1a), reveals a large subtropical anticyclonic ridge over the Tibetian-Himalayan region (Lat 27-40°). The mean position of the subtropical high shifts southward each month between July and February (Figure 3.2a) and its trajectory is in synchronization with the propagation of the monsoonal heat low (cf. Figure 5.4 Krishnamurti et al. 2013 [75]). In the case of Phailin, the subtropical high was anomalously north, and comparable to what is expected in September, as per climatology (Figure 3.2c). This anomalous position of the subtropical high is potentially linked to the variability in

the withdrawal of the monsoons in the year 2013. An active period in late September-October 2013, delayed the withdrawal by ∼3 weeks, with the withdrawal isochrones differing by ∼10-15° during the time that Phailin (the first post-monsoon tropical cyclone of 2013) traversed across the Bay of Bengal [76] (Figure 3.2b).

On the other hand, the dominant anticyclonic ridge had moved southward and away from the Himalayas (∼Lat 17-22°) by mid-November (Figure 3.1b). This is consistent with the post-monsoon, early-winter climatology (Figure 3.2a). Apart from the seasonal progression of the subtropical ridge within six-weeks, Lehar's environment was potentially influenced by its predecessors Phailin and Helen (not explored in this study). Figure 3.1b indicates that the north-south pressure gradients on either side of the ridge were large, causing the ridge to be compressed around its center. Figures 3.1c and 3.1d compare the depth and intensity of the environmental winds impacting the TC vortex. Figure 3.1d indicates the presence of an upper-level anticyclone, extending to about 400 mb, six hours before the start of rapid weakening. While the Figure only shows a snapshot in time, analysis of these streamlines with depth across several times, indicated a tilted ridge, extending down to 650 mb at certain times. Further, the ridge presented as two bifurcated centers at the start of Lehar's lifecycle and then went to evolve into a giant anticyclone by the end of its life-cycle (not-shown). The proximity (∼10° from the TC), intensity, and depth of the upper to mid-level anticyclone cause the upper portions of the vortex to experience a different environmental forcing as compared to the lower portions of the vortex. This manifests as shear in Lehar's environment. Overall, the intensity and magnitude of the winds impacting Phailin (Figure 3.1c) are much less than that of Lehar (Figure 3.1d).

Figures 3.1e and 3.1f show the comparison of the evolution of local (bulk) shear and environmental (bulk) shear. The motivation behind differentiating behind the environmental and local shear is two-fold. First, the differentiation allows us to move away from the traditional consideration of shear as a one-way forcing from the environment onto the vortex, and acknowledge that the vortex is feeding back

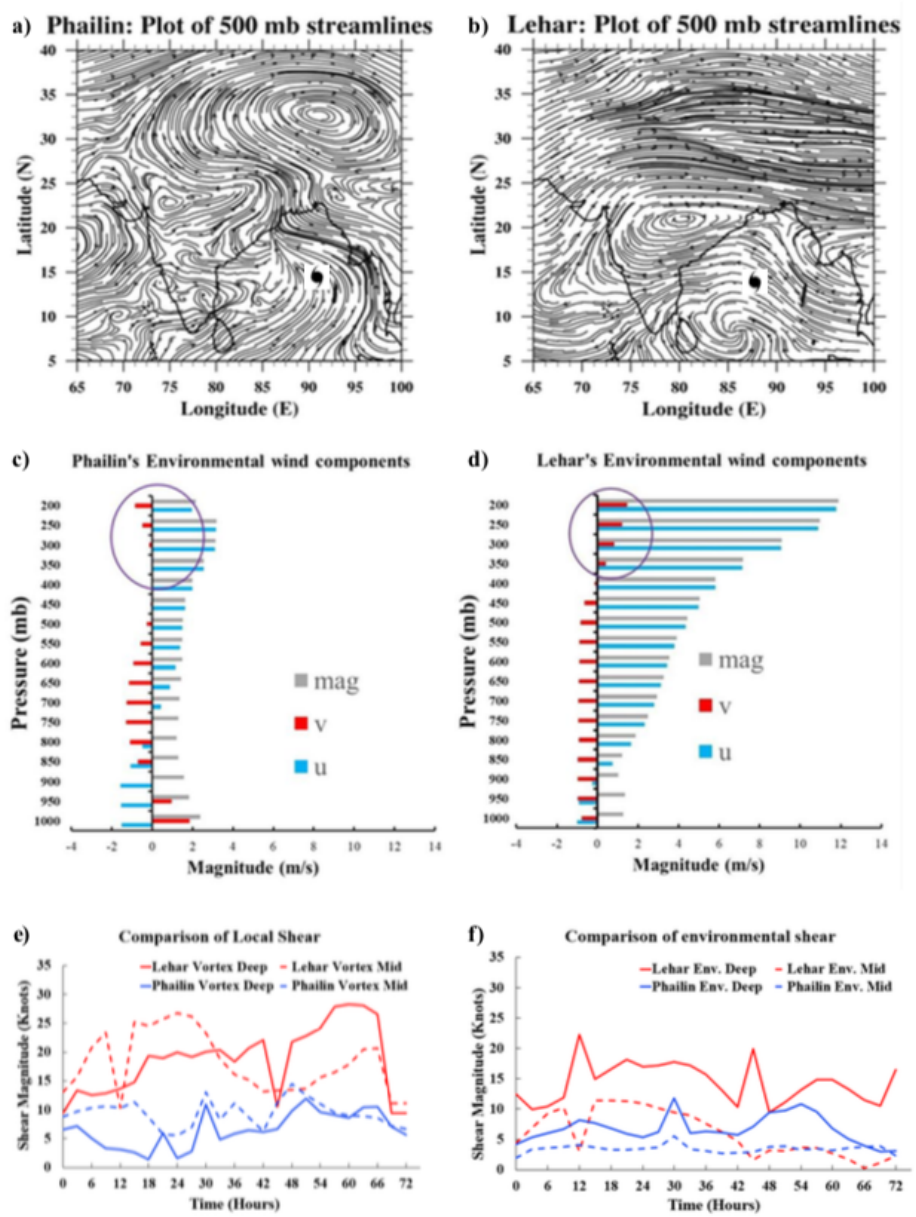

Figure 3.1. (a, b) are plots of (vortex-removed) streamlines at 500 mb for Phailin and Lehar, showcasing the position of the subtropical high. (c,d) present a snapshot (t=24) of the environmental zonal wind, meridional wind, and the wind vector magnitude, computed at each level for Phailin and Lehar. The highlighted portion indicates the presence of an upper-level anticyclone (positive and clockwise tangential velocity) in Lehar's environment and the absence of it in the case of Phailin. (e,f) serve to compare the deep (200 - 850 mb) and mid (500 - 850 mb) bulk-shear values within the vortex (the winds at each level are first domain averaged in an 2°x 2° box) and in the environment (the vortex is removed and the domain averaging of winds at each level is done within an 8.5°x 8.5° box).

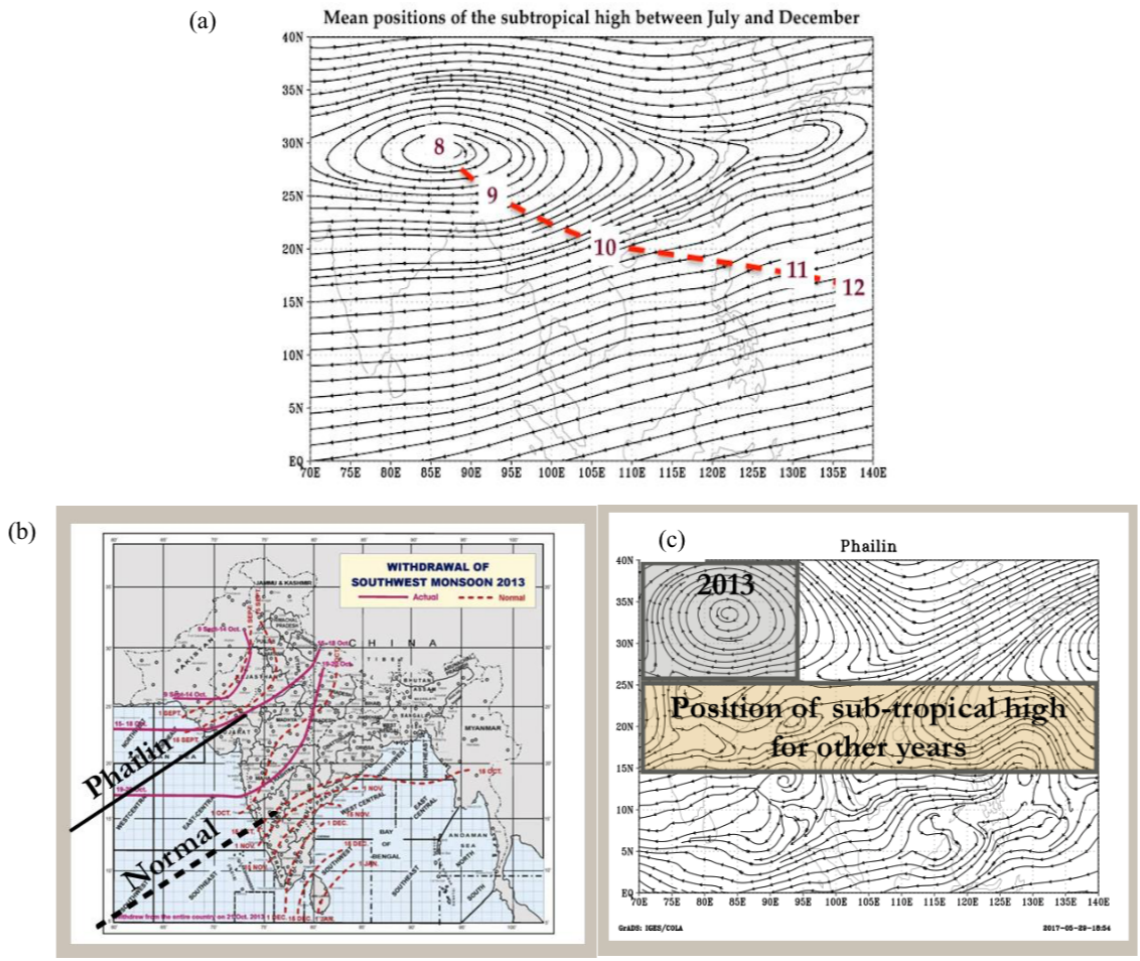

Figure 3.2. (a) Mean position of the subtropical high calculated from August to December as per climatology. Computed using ECMWF reanalysis. (b) Withdrawal isochrones of southwest monsoons in the year 2013 highlighting the delay in withdrawal during the lifetime of Phailin. Adapted from the publicly available withdrawal isochrones generated by the India Meteorological Department (c) Streamlines averaged between 200 - 400 mb from GFS indicating the position of the subtropical high during Phailin's time period and the position of the subtropical high for the other between years 1978-2016 computed using reanalysis.

onto the environment and (potentially) modifying its own local shear. Second, there are multiple definitions of shear in use within the TC community while conducting shear-vortex experiments (e.g., the 120 km domain used in Riemer et al. (2010) [77] v/s the vortex-removed, 500 km domain in Chen and Gopalakrishnan (2015) [71]). These differences are due to an implicit understanding within the community that the shear experienced by the vortex, is possibly different from the environmental shear (Personal communication with Riemer, M., Ryglicki, D., and Rogers, R).

Figure 3.1e shows that the deep-shear of Lehar was persistently between 15-20 knots before and during the period of rapid weakening (16-40 hours) and $\geq$20 knots as Lehar approaches land, and post-landfall (48-72 hours). Furthermore, Figure 3.1e reveals that the mid shear was particularly high ($\sim$25 knots) between 12-30 hours when the rapid weakening was initiated. On the other hand, Phailin's local shear was consistently below 10 knots, except for a modest increase towards the end (45-66 hours) when the storm was at peak intensity. Figures 3.1e and 3.1f also indicate clear differences between the environmental shear and local shear, despite structural similarities. For example, the magnitudes of mid-shear within the vortex are nearly double the magnitudes in the environment between 12-42 hours, despite similarities in their trends. The magnitudes of Lehar's environmental shear are comparable to that of its local shear magnitudes between 12-42 hours when the storm rapidly weakened but are much lower between 48-72 hours. While Phailin's environmental deep-shear values are slightly higher than its local counterpart, its environmental mid-shear values are almost half of its local shear values.

The traditionally used bulk-shear estimates (the difference between wind vectors at 200 mb and 850 mb for deep-shear, and 500 mb and 850 mb for mid-shear) might under-represent the structural complexity of the vortex and the environmental flow-field in three dimensions. For this purpose, we present the hodographs of winds computed within the TC vortex and in an annulus outside the vortex, representative of the environment (Figures 3.3a - 3.3d) right before the start of the rapid change in intensity, for each of the TCs. The domain averaging removes the wavenumber 0

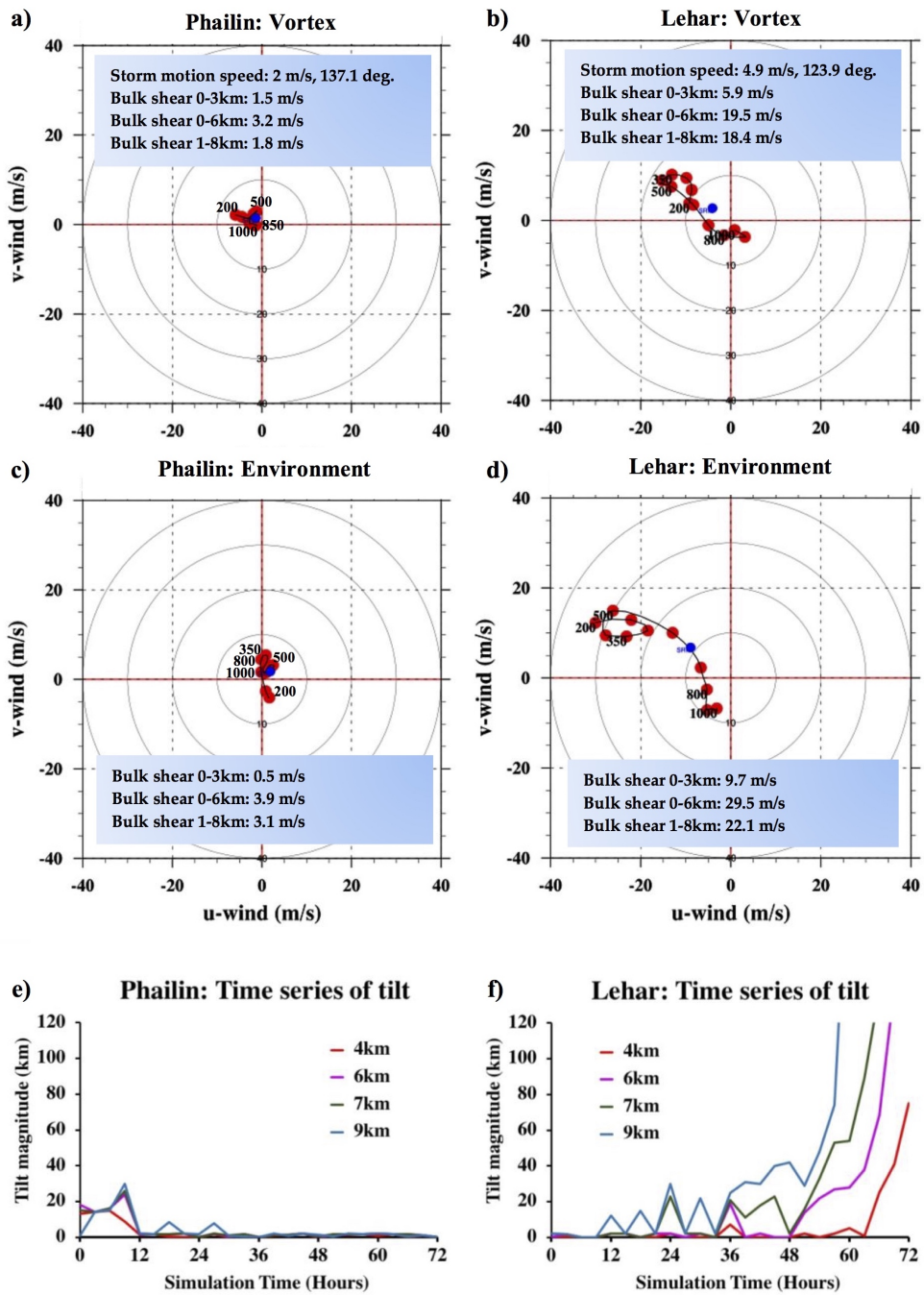

Figure 3.3. ((a,b,c,d) Hodographs of winds computed within the vortex (domain averaged in an 2°x 2° box at each vertical level) and in the environment (domain averaged in a 8°x 8° box after vortex removal at each vertical level) for Phailin just before the RI (t=27) and for Lehar just before the RW (t=27). The shear magnitudes are vector differences between domain averaged winds computed at the vertical levels indicated. (e,f): Time series of vortex tilt (difference in circulation centers at various levels from the circulation center at 1.5 km) for Phailin and Lehar. 1 m/s = 1.943 knots.

component from the TCs. Also highlighted are the storm motion speed and direction, and the bulk-shear computed at different levels. Figures 3.3a and 3.3b indicate an extremely organized vortex, with very low shear within the vortex and the environment (cf. Figures 3.1e and 3.1f at t =24). Compared to Phailin, Lehar's wind magnitudes are more than twice as greater within the vortex, and close to four times greater in the far environment, and the flow-field is far more complex (Figures 3.3b and 3.3d). Figure 3.3b serves to illustrate that the bulk-shear estimate using the difference between 200 and 850 mb might be under-representing the actual shear in the vortex. For example, at t=24 (just before the start of the weakening), the maximum shear is between 350 mb ($\sim$8 km) and 850 mb at 18.4 m/s or 35.76 knots.

Figure 3.3b is indicative of the intense ($\geq$ 20 m/s or 38.8 knots), southeasterly winds between 200 and 500 mb due to the proximate ridge. Figures 3.3e and 3.3f are plots of the time-series of the vortex tilt between the circulation centers at 1.5 km with various heights. Phailin's time-series shows that after an initial wobble (fluctuation in the vertical alignment of the vortex) with tilt magnitudes extending to $\sim$30 km, the amplitude drops considerably at around 12 hours. After this, the tilt magnitude is negligible. On the other hand, Lehar's plot of tilt indicates an increasing discordance between the circulation centers at different heights, until a point where it wobbles out of phase with itself ($\sim$36 hours). As suggested in Reasor et al. (2004) [78], there is a clear oscillation of the TC vortex in pursuit of dynamic equilibrium with its environmental forcing. While the frequency of the oscillation seems steady at around 6 hours, the amplitude of the oscillation increases as the ability of Lehar's vortex to realign vertically reduces with time. As the tilt extends to various depths of the vortex, like a feebly spinning top conserving angular momentum, the amplitude gradually increases until the vortex weakens.

Figure 3.4 further serves to explain the differences in the environments of the two TCs, before they diverged to intensify/weaken. Figures 3.4a and 3.4b show the geopotential heights of the respective storm environments at 300 mb. In the case of Phailin, the peak geopotential heights are found over the Himalayas, and

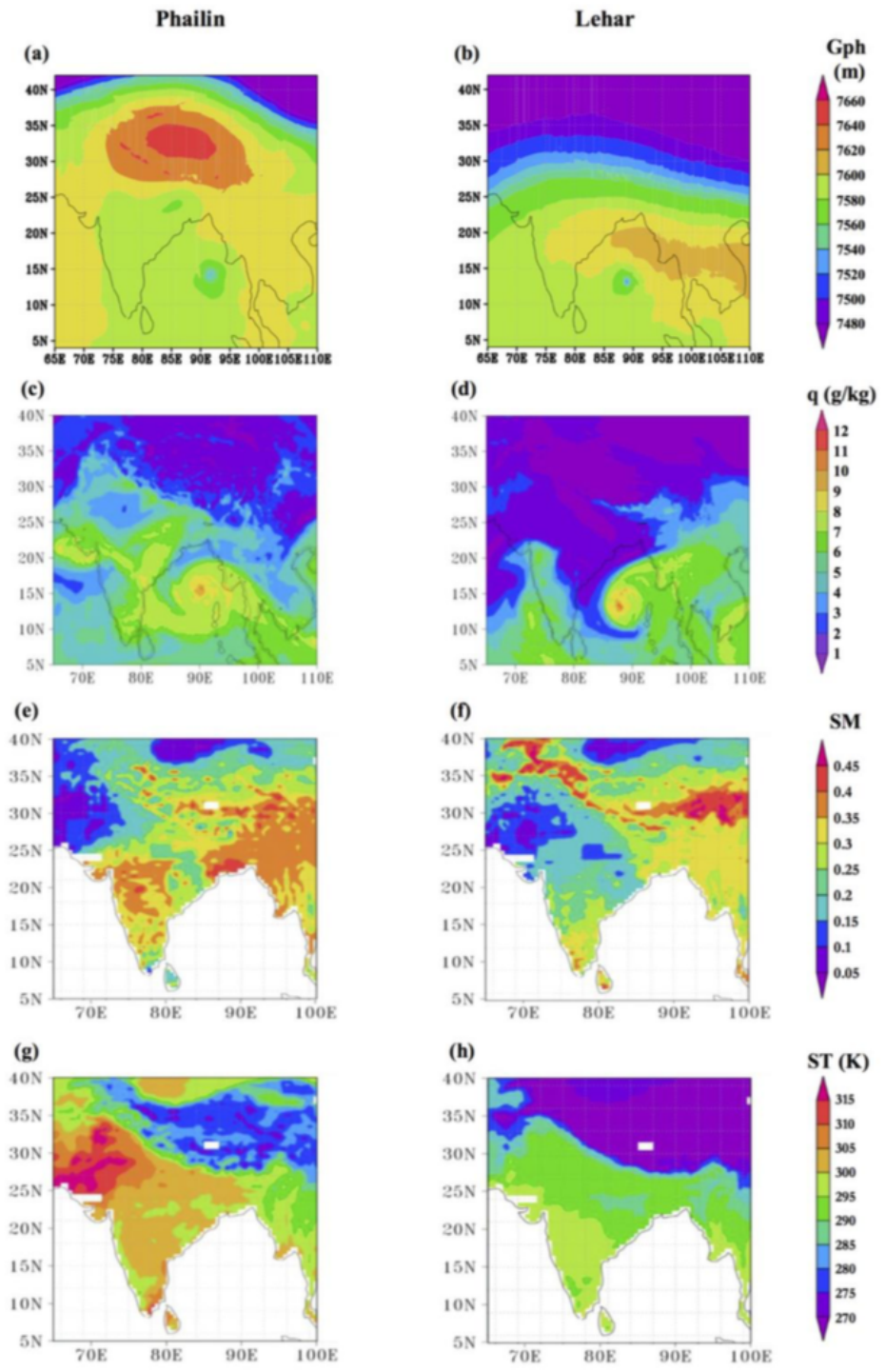

Figure 3.4. (a,b) Plot of Geopotential heights at 300 mb for Phailin and Lehar, highlighting the pressure gradient in the meridional direction before the start of weakening and intensification. (c,d) Plots of 500-850 mb integrated specific humidity in g/kg. (e,f,) Plots of antecedent soil moisture (top-layer) in volume fraction (g,h) Plots of antecedent soil temperature (top-layer) (K)

minimal gradients are found in the proximity of the storm. On the other hand, Lehar's environment is much more baroclinic, with noticeable pressure gradients in the North-south (meridional) direction. These gradients compress the flow field on either side of the ridge (cf. Figure 3.1b) and drive the shear experienced by Lehar. Figures 3.4c and 3.4d show the vertically integrated specific humidity in the storm environments. Figure 3.4c indicates that the cold, dry continental air was restricted to the Himalayan region and the environment in the vicinity of Phailin was moisture-rich. However, over the next six weeks, the cold and dry, continental air was drawn south into the flow field of the ridge and Lehar. In addition to the seasonality, there is a possibility that Lehar's two preceding TCs - Phailin, and Helen, drew a lot of moisture from their environments and altered the synoptic environments for Lehar (not explored in this study). Due to the delayed withdrawal of monsoons at the time of Phailin, the antecedent soil moisture was higher, and the soil was warmer (Figure 3.4e, Figure 3.4g). In contrast, due to the onset of winter by late November, Lehar's antecedent soil temperatures were colder (Figure 3.4f) and despite rainfall from TC Helen (landfall location 15N, 80E) during the same time that Lehar was traversing across the Bay of Bengal, the net soil moisture content was markedly lower than Phailin's (3.4h).

In summary, Phailin and Lehar experienced remarkably different environments within a relatively short period of time. We will now explore how the convective organizations of these two TCs are strongly tied to the evolution of the environments that they encounter.

3.1 Externally induced asymmetries

The objective here is to investigate the weakening of Lehar's sheared vortex and diagnose the aspects of its asymmetric convective organization that led to it.

To investigate the local environments within the vortex that determine the development of convection, first, a plan view of the near-surface boundary layer equivalent

potential temperature (θ_e, also referred to as moist-entropy) is shown for Phailin and Lehar (Figures 3.5a and 3.5b respectively) for the purpose of contrast. While a symmetric envelope of high θ_e is present around Phailin's eyewall (Figure 3.5a), an azimuthally asymmetric distribution of Lehar's θ_e, with the highest near-surface θ_e concentrated in the downshear right quadrant (DSR) (Figure 3.5b). This asymmetric distribution of θ_e is consistent with prior observational [61, 79] and modeling studies [77] of sheared vortices.

3.1.1 Thermodynamic aspects

To further understand the spatial distribution of θ_e and convection (comprising of updrafts and downdrafts), the radius-height plot of each of the quadrants highlighted in Figure 3.5b is shown at the start of the weakening process (Figures 3.5c-f). The deep convection (we define this as the upward motion in which the convective mass flux is transported to at least 8 km in the vertical) is concentrated mostly in the downshear quadrants (Figures 3.5c and 3.5d) around 40-60 km radius. In the upshear-left quadrant (USL), the upward motion is located $\sim$40 km radius between regions of strong downward motion on either side. Consistent with prior documentation [71], strong, convective-scale downdrafts that are maximized around 8-10 km in the vertical are present in the downshear-left (DSL) and USL quadrants, albeit within the eyewall region (radii $\leq$ 40 km). However, these downward motions within the eyewall region are unlikely to play any role in bringing the environmental low θ_e air into the storm vortex, since the eyewall is thermodynamicly protected by deep convection and dynamicly by the strong tangential winds at the radius of maximum winds (30 - 40 km). As articulated in Riemer and Montgomery (2011) [80], a combination of downward motion and cross-vortex (storm-relative, radial) flow is needed for the environmental air to intrude into the vortex core.

Just outside the eyewall region between 40-80 km radii, deep downdrafts in the upshear quadrants (upshear left (USL) and upshear right (USR) in Figures 3.5e,3.5f)

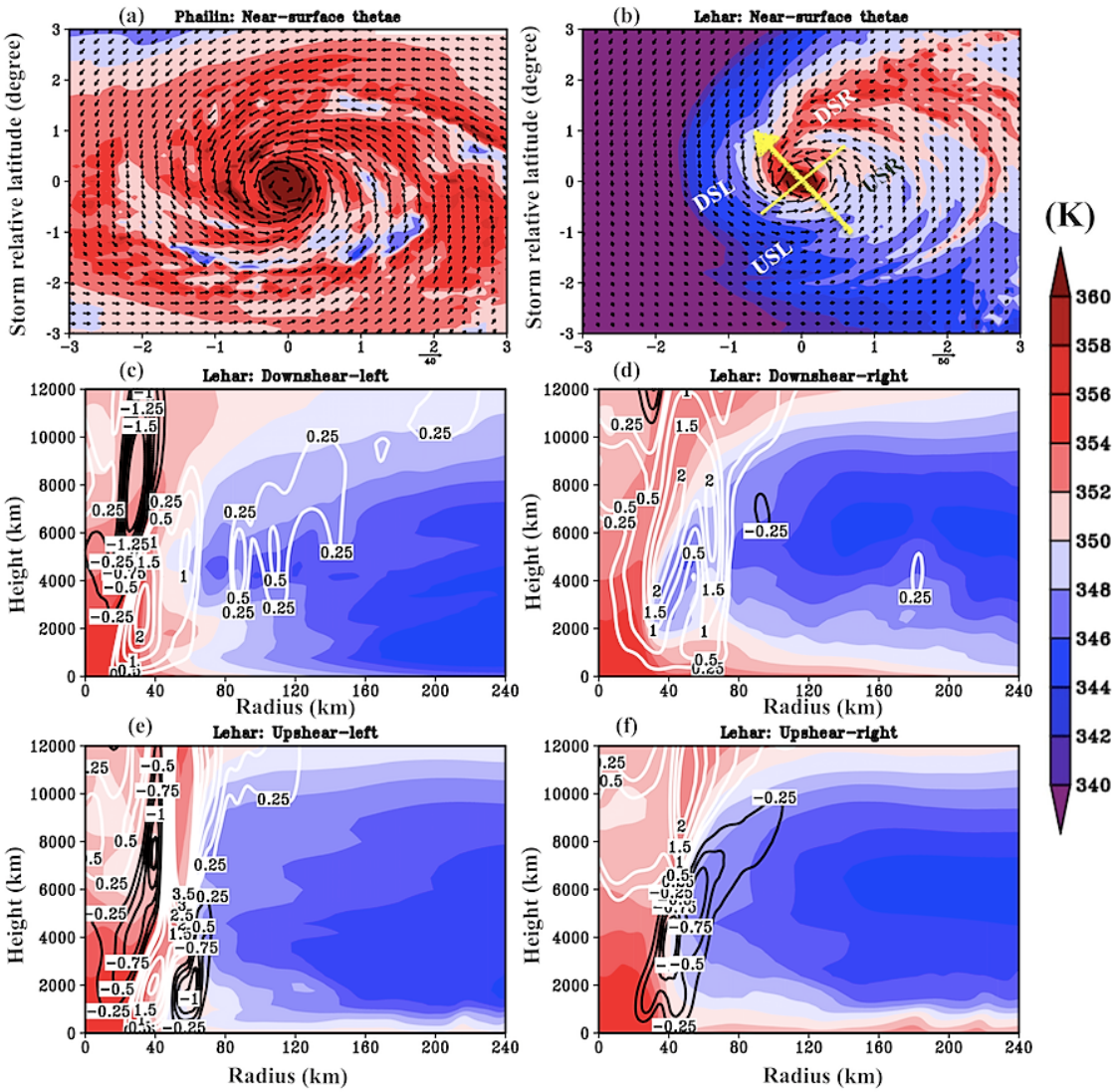

Figure 3.5. Plan view of the near-surface θ_e (averaged within 2km from the surface) for Phailin (a) and Lehar (b) three hours prior to the start of the rapid intensity change. The four quadrants - downshear right (DSR), downshear left (DSL), upshear left (USL) and upshear right (USR) are marked in b. Figures c-f present the quadrant averaged, radial-height plots of θ_e for Lehar at t = 24.

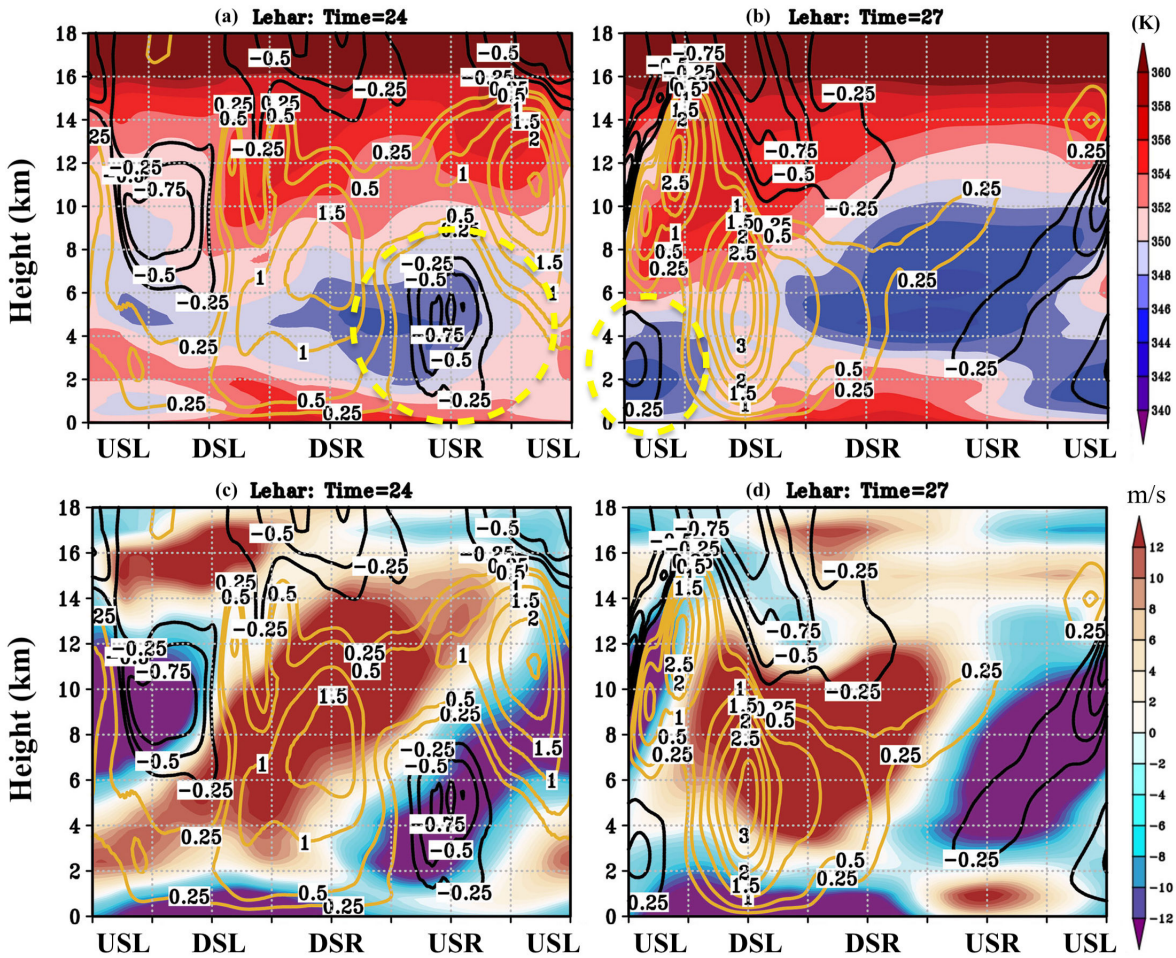

Figure 3.6. Lehar's Azimuth-height plots of θ_e(shaded) and vertical velocity contours (updrafts in golden and downdrafts in black) at two times: t=24 (3 hours before RW) and t=27 (start of RW) (panels a, b respectively). Panels c and d show the corresponding azimuth-height curtains for radial velocity (shaded) and vertical velocities (contours) for Lehar at the same times.

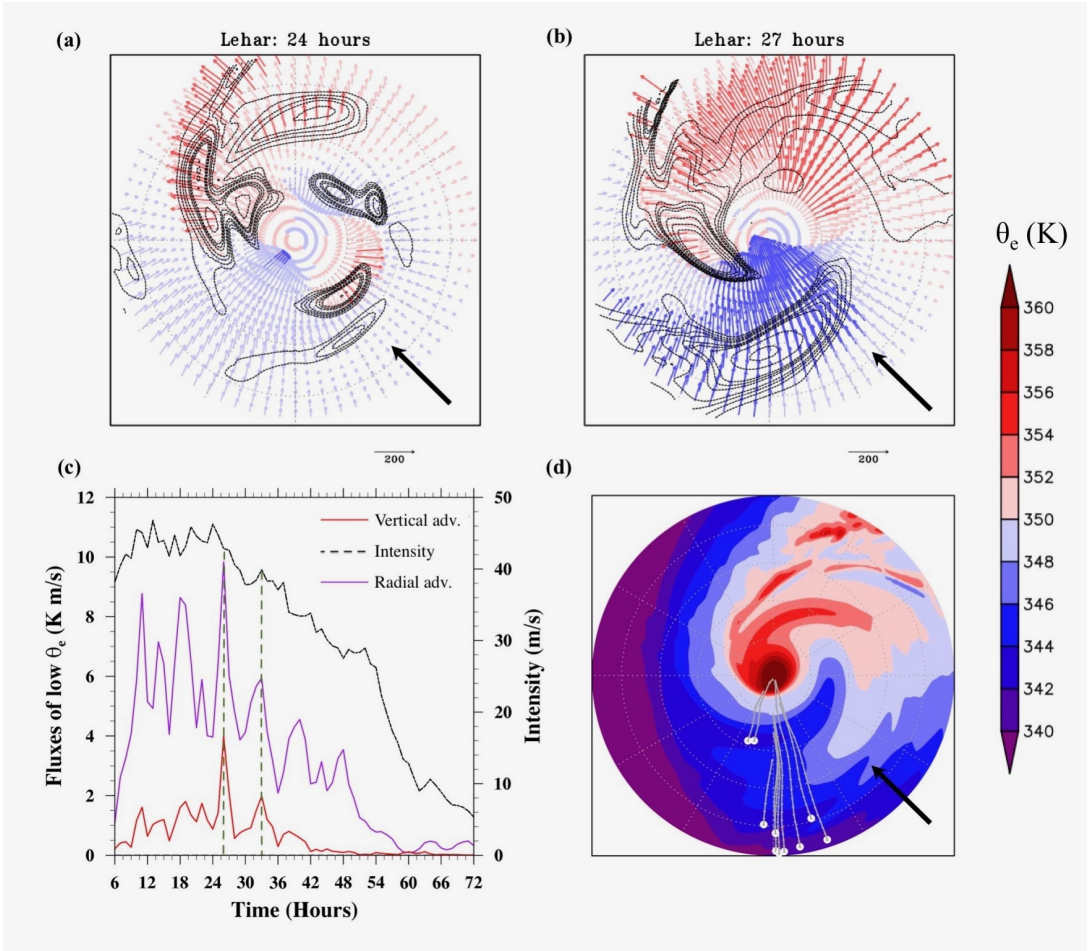

Figure 3.7. (a,b) Radial flux of θ_e anomaly ($u\theta_e'$) within the boundary layer (vectors, colored according to θ_e' (azimuthal mean is subtracted) where blue indicates negative θ_e' and red indicates positive θ_e'). The θ_e' is averaged from the surface to 1.5 km in the vertical to represent the θ_e distribution within the boundary layer. Additionally, the downward flux of θ_e' (-1*$w\theta_e'$) through the top of the boundary layer (assumed to be at 1.5 km) is indicated as dashed contours. These plots are shown at two times: t = 24 (just before RW) and t = 27 (start of RW) and the shear vector is indicated by the black arrow. (c) Time-series of the magnitudes of $u\theta_e'$ and $w\theta_e'$ where a Heaviside function is used to ensure that only the inflow, downdrafts, and negative θ_e' are considered in the computation. The times when the the magnitudes of the vertical and radial fluxes of low θ_e peak together are highlighted and shown in the context of the timing of the rapid weakening. (d) Back-trajectories of low θ_e' (θ_e less than 342 K) air within 30 km radius. The radial extents for panels a, b, and d are 0 to 90 km.

are seen reaching the surface. These downdrafts are present underneath moderate to strong updrafts (vertical velocities between 0.5 to 1.5 m/s) and are in the proximity of low θ_e air. When the precipitation from these updrafts falls through these dry (low θ_e) unsaturated regions, it is expected to evaporate. The downdrafts (sinking motion) seen in the upshear quadrants are most likely a result of the consequent cooling that occurs when the latent heat of evaporation is subtracted from the surrounding environment as addressed in several previous studies [70, 77, 81–84]. Riemer et al. (2010, 2013) [77, 85] noted in their idealized experiments that such downdrafts might act to bring the low θ_e from outer radii (e.g. radii greater than 80 km in this case) into the boundary layer and near-surface regions.

However, both the upshear quadrants contain such downdrafts. This begs the question: Which of the two upshear quadrants present a likely configuration for the intrusion of low moist entropy air? The answer to this depends on the relative location of the downdrafts carrying low θ_e air (through the top of the boundary layer) with respect to the location of the inflow (within the boundary layer). We present an azimuth-height plot in Figure 3.6 while radially averaging between 20-80 km, keeping in mind that the radial location of these downdrafts was between 40-80 km (3.5e, 3.5f) and that the radius of maximum winds (at the surface) was at 30 km. Figures 3.6a and 3.6b show Lehar's θ_e (shaded) and vertical velocities (contours) at two times: t=24, that is three hours before the weakening and at t=27, when the rapid weakening began. Likewise, Figures 3.6c and 3.6d show the radial velocity (shaded) and vertical velocities (contours) for the same times as 3.6a and 3.6b. The θ_e, the vertical velocities, and the radial velocities are all extremely asymmetric in the azimuthal direction, consistent with the behavior of sheared storms in Marks et al. (1992) [9], Rogers et al. (2016) [61], and Reimer et al. (2013) [85]. Additionally, in Lehar's case, the storm motion vector was coincident with the shear vector. While we know that a combination of these vectors dictates the azimuthal distribution of inflow [65, 66], the asymmetries due to motion and those due to shear may interfere destructively or

constructively, and a comprehensive understanding of their nonlinear interplay is yet to be reached (a topic not explored in this study).

As expounded in the previous sections, the vertical structure of the environmental winds might be much more complex than that indicated by the bulk-shear vectors. From that perspective, while we have a general understanding that downdrafts (updrafts) occur in the upshear (downshear) side and that inflow (outflow) occurs in the upstream/downshear (downstream/upshear) side [9, 14], our prior knowledge based on the bulk (deep) shear vector might fail to capture the complexity in the spatial distribution of the downdrafts, inflow, and θ_e for specific cases.

Azimuthal phasing in the upshear-left quadrant

In Figures 3.6a and 3.6b, the downdrafts carrying low θ_e air are maximized in the USR (NE-E-SE) quadrant at t=24 but move to USL (SE-S-SW) by t=27. These azimuth-height 'curtain' plots may be understood along the direction of the flow, i.e., cyclonic (DSR-DSL-USL-USR-DSR or NE-NW-SW-SE in this case; cf. Figure 3.6b). Given that these plots are snapshots in time, they must be cautiously interpreted as a spectrum of updrafts and downdrafts that combine to produce a net effect indicative of updrafts or downdrafts. Single updrafts/downdrafts are not tracked here, and it is possible that individual downdrafts exist in the presence of mean upward motion and vice versa. At t=27, the updrafts can be seen to begin in the DSR quadrant (NW-NE-E) and maximize in the DSL quadrant (SW-NW). Further, upper-level updrafts overlay a low-level downdraft in the USL region (S-SW, between 6-16 km in Figure 5b). This is very consistent with the observations in Rogers et al. (2016) [61] and Nguyen et al. (2017) [86] where an updraft was seen to initiate DSR, mature DSL, ascend USL, whilst overlaying low-level downdrafts, before terminating USR.

The convective patterns at t=24 is a little more complicated, possibly because we are taking a snapshot when the convection is at different stages. At this time, there is a strong updraft in the DSR (W-NW-N-NE) quadrant, a weak mid-to-upper-

level downdraft DSL/USL (W-SW-S-SE), a weak updraft USL (SW-S) and a strong downdraft USR as mentioned above. Between the two times, the inflow structure remains almost the same (Figures 3.6c and 3.6d). A low-level inflow is prevalent in the S-SW-W-NW or USL-DSL-DSR region, and an upper-level slanted outflow is present in the W-NW-N-NE or DSL-DSR regions. Further, a more azimuthally confined region of low-level outflow is prevalent in the NE-SE (USR) quadrant. While there is a slight extension of the low-level outflow in the SE-S (USL) quadrants at t=24, the low-level outflow is confined to the USR quadrant (NE-SE) at t =27, and low-level inflow occupies the USL quadrant (SE-S-SW).

The distribution of θ_e within the boundary layer is dictated by the vertically downward (mean and eddy) fluxes through the top of the boundary layer, the radially inward (mean and eddy) fluxes within the boundary layer and the surface fluxes [79, 83, 84]. Our focus in this section (Figures 3.6 and 3.7) is specifically on the downward and radially inward eddy (azimuthal mean field is subtracted) fluxes of low θ_e. At t=24, when the downdrafts are maximized in the USR quadrant (Figure 3.6a), the vertical flux of low θ_e air through the top of the boundary layer is juxtaposed predominantly with the radially outward flux of low θ_e within the boundary layer (Figure 3.7a, 3.6c). Under such a scenario, one would expect that the low θ_e air flushed into the boundary layer by the downdrafts simply exits the region without penetrating into the eyewall. On the other hand, at t=27 when the downdrafts are in the USL quadrant (Figure 3.6b), they are collocated with inflow within the boundary layer (Figure 3.6d). In other words, the vertical eddy flux of low θ_e air through the top of the boundary layer is juxtaposed with radially inward eddy flux of low θ_e air within the boundary layer (Figure 3.7b). Such a juxtaposition in the upshear left quadrant creates a configuration that is conducive for the low θ_e air from the environment to penetrate into the boundary layer and then into eyewall region (as evidenced by the blue, radially inward vectors reaching inner radii).

Figure 3.7c provides a time-series of the (azimuthally and radially averaged) magnitude of vertical and horizontal fluxes transporting low θ_e air. Figure 3.7c illustrates

that in addition to the collocation in the azimuthal phasing evidenced in Figures 3.6a-d and 3.7a-b, there was synchronization between the peaks of *magnitudes* of the vertical and radial fluxes of low θ_e air. Finally, Figure 3.7d shows the back trajectories of air parcels whose θ_e values were below 342 K within the radii of 30 km. The trajectories are through the USL quadrant, the quadrant where the maximum juxtaposition is observed in Figure 3.7b.

In summary, we have identified the upshear-left quadrant in Lehar as a region that is vulnerable to the adverse, external influences and must be monitored for early warning signals of rapid weakening.

Prior studies [79, 84, 87] demonstrated and addressed the issue of TC intensity change as a competition between the surface fluxes that serve to refurbish the boundary layer with warm and moist air from the ocean, and the above-mentioned fluxes that transport low θ_e air from the environment into the TC inner core. From that perspective, the weakening of Lehar may be interpreted as a scenario where the surface fluxes fail to refurbish the deficit in θ_e within the TC boundary layer created by the synergistic action of the downward and radially inward eddy fluxes.

It is important to note that at the time that the weakening is triggered, a reasonably strong (as well as azimuthally aligned with downdrafts) inflow is necessary to facilitate the intrusion of low θ_e air. Over time, as the low θ_e air intrudes into the vortex core and the air-sea instability reduces, the radial pressure gradient within the boundary layer begins to drop. When this occurs, the strength of the inflow also decreases as the TC weakens (cf. Figure 2.3). This whole series of events is apparent only in an azimuthally *asymmetric* point of view. If this is purely viewed from an azimuthally axisymmetric perspective (as in Figure 2.3b), only the 'effect' viz. strong inflow when the TC is intense, and weak inflow when the TC weakens, is visible. The background θ_e, as well as the generation of pathways for the mixing of environmental θ_e into the TC core by shear, makes all the difference in this case.

Summary

In Lehar's sheared vortex, the thermodynamic and dynamic environments within the vortex upon which the convection is embedded upon are asymmetric. Under such a scenario, while the demise of a vortex is the result of a series of events, we demonstrate here that the *trigger* of Lehar's RW occurs when the azimuthal phasing of the vertical flux of low θ_e air through the top of the boundary layer and the radial flux of low θ_e within the boundary layer synchronize. Such a juxtaposition occurs in the USL quadrant between 40-80 km radii and creates a pathway for the environmental air to intrude into the eyewall region. This is an extension of the PBL flushing mechanism proposed by Riemer et al. (2010, 2013) [77, 85]. We add an asymmetric component here and argue that the boundary layer flushing mechanism becomes operative only when the azimuthal phasing of the inflow is favorable to the downward flux of low moist entropy air from the downdrafts. Since convection is an intrinsic and stochastic process that occurs in response to air-sea instability, the identification of the local pockets (upshear left in Lehar's case) within the vortex that are disruptive to the growth and sustenance of deep convection and how this ties to the evolution of the TC's atmospheric environment is of crucial importance.

Given the complexities of the shear profiles and the asymmetric distribution of the various fields within the vortex, the collocation in the azimuthal phasing and magnitude of the boundary layer inflow, vertical velocities, and low θ_e, may be used as a diagnostic to detect rapid intensity changes. We speculate that in a sheared TC that goes on to intensify, there will be a collocation in the azimuthal phasing between the boundary layer inflow, updrafts, and positive θ_e anomaly. This aspect is not explored in this thesis.

3.1.2 Dynamic aspects

Having examined the thermodynamic aspects, in this section, we investigate the weakening of Lehar's tangential winds as a response to various forces terms from a

dynamic perspective. We begin with the analysis of the azimuthally-averaged tangential momentum budget where the instantaneous (or time-averaged) quantities are partitioned into azimuthal mean and eddy terms (an approach similar to Reynolds-averaging in fluid dynamics).

$$\frac{\partial\langle v\rangle}{\partial t} = -\langle u\rangle\langle f+\zeta\rangle - \langle w\rangle\frac{\partial\langle v\rangle}{\partial z} - \langle u'\zeta'\rangle - \langle w'\frac{\partial v'}{\partial z}\rangle + \langle\frac{1}{\rho r}\frac{\partial p'}{\partial\theta}\rangle + F_r. \tag{3.1}$$

Here in Eq. 3.1, the azimuthal mean quantities are represented within angular brackets and the azimuthally asymmetric terms are represented as primes. The storm-relative radial, tangential, and vertical velocities are represented as u, v, and w respectively. ζ represents the vertical component of relative vorticity and f is the Coriolis parameter. The density and pressure are represented as ρ and p respectively. Finally, r represents the radius, and θ, the azimuthal angle. The force terms that contribute to a rate of change in the azimuthally-averaged tangential velocity include the mean radial vorticity flux (Term 1 on the right), the vertical advection of tangential momentum by the mean secondary circulation (Term 2), the eddy radial vorticity flux (Term 3), the eddy vertical advection of tangential momentum (Term 4), the pressure perturbation term (Term 5) and the frictional term (Term 6, F_r).

This terminology is consistent with Persing et al. (2013) [31] and Smith et al. (2017) [32] except for the treatment of the residual term. Here, the frictional term and the pressure perturbation term are not explicitly computed. Instead, a residual term is computed merely as the difference between the net tendency in $\langle v\rangle$ and the sum of terms 1-4 (similar to the treatment in [88]).

Persing et al. [31] noted a few sources of errors that might result in differences between the tendency of the tangential velocity computed as the sum of the force terms and the tendency computed directly as a finite difference between the two times. We acknowledge the errors from sampling rate (1 hourly outputs), the error associated with finite difference schemes used in place of the derivatives and the choice of a surface-based pressure center regardless of the magnitude of the variation in the circulation centers at different heights within the vortex. Thus, in addition to the diffusion term and the pressure perturbation term, errors from the above-mentioned

sources are contained in the residual term. However, while these errors are implicit in the residual term, the effect of these errors is not to reverse the overall sign of the other tendency terms. Our primary intent in this analysis is to understand the roles played by the specific terms in the budget equation in contributing to a positive or negative spin-up in $\langle v \rangle$ at a *system-scale*. Smith et al. (2017) [32] and Leighton et al. (2018) [33] offer very insightful analyses of Earl, a sheared, intensifying storm. This study seeks to complement the existing body of literature by offering an analysis of a sheared, rapidly weakening TC.

When a vortex is subject to external shear, eddies in addition to the intrinsic eddies addressed in the previous section are introduced. Shear-vortex interactions result in an azimuthal reorganization of the upward and downward motions, vorticity, θ_e, and the radial flow within the TC boundary layer (BL). Furthermore, a tilted vortex also excites vortex-Rossby waves. Under such scenarios, it is important to note that it is not mathematically possible to separate the intrinsic eddies from the shear-induced ones since they are nonlinearly coupled.

Figure 3.8 shows Lehar's radial-height plots of the terms from tangential momentum budget time-averaged during the early period of RW (t=24 to 36 hours). The net tendency term (Figure 3.8f) indicates a clear weakening trend within the radius of maximum wind (RMW). We wish to specifically focus on the influence of the eddy terms towards this trend. Figure 3.8c shows a strong concentration of positive eddy vorticity flux straddling the RMW, in the mid-levels between 4-12 km in the vertical. Under this pocket of positive eddy vorticity flux is a region of negative eddy vorticity flux whose structure corresponds well with the low-mid level (0-8 km in the vertical) weakening belt within the RMW in Figure 3.8f.

Leighton et al. (2018) [33] had examined an ensemble of simulations conducted for Hurricane Edouard and concluded that positive eddy-vorticity flux in the mid-levels is an indicator of RI and negative eddy flux is an indicator of weakening. However, contrary to their findings, our results suggest that mid-level positive eddy vorticity flux cannot be used as a unique signature of sheared-RI storms (cf. their Figures

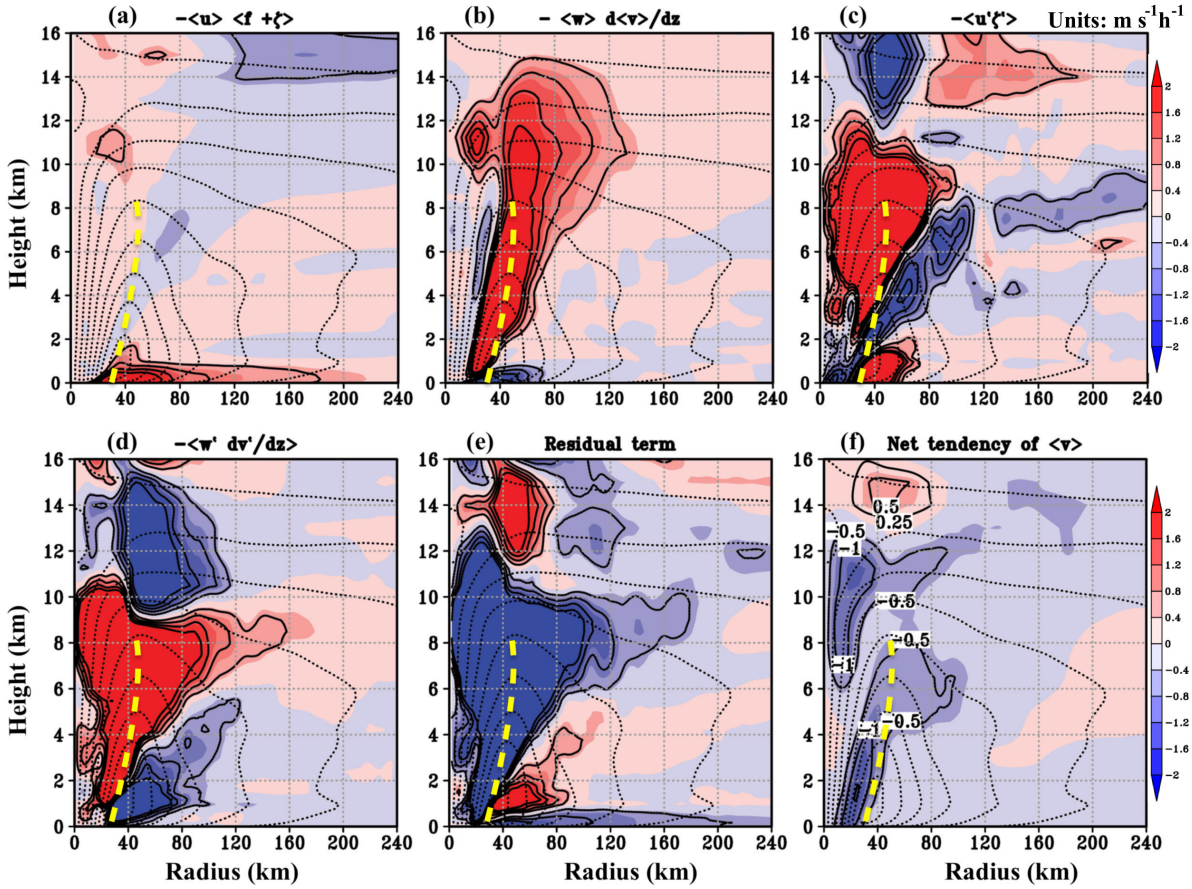

Figure 3.8. Radius-height plots of the terms of the tangential momentum ($\langle v \rangle$) budget time-averaged during the initial period of Lehar's RW (24 - 36 hours). (a) Mean radial vorticity flux ($V_{m\zeta}$) (b) vertical advection of tangential momentum by the mean secondary circulation (V_{mv}) (c) the eddy radial vorticity flux ($V_{e\zeta}$), (d) the eddy vertical advection of tangential momentum (V_{ev}) (e) Residual terms (f) Net tendency in $\langle v \rangle$ over the period of interest. Units for all panels is $ms^{-1}h^{-1}$ and the contour intervals are 0.5 $ms^{-1}h^{-1}$. The dotted lines represent the $\langle v \rangle$ contours and the yellow dashed line represents the radius of maximum $\langle v \rangle$ at each height.

8d, 9d). Rather, Lehar's budget analysis seems to suggest that such a positive eddy vorticity flux is a characteristic of sheared TCs in general and that there are other counteracting mechanisms that are possibly not captured by the present framework that differentiate a sheared TC that undergoes RI or RW.

Similar to its radial counterpart, the plot of the vertical eddy flux term also indicates a zone of strong positive tendency straddling the RMW stretching from 2-10 km in the vertical. This pocket of positive eddy vertical flux is countered by strong negative tendencies just outside the RMW (40-100 km radii) and less than 6 km in the vertical. This negative tendency is related to the downdrafts (due to evaporative cooling) that are restricted to the upshear quadrants and transport low θ_e air into the BL ([77], Section 3.1.1).

Dynamic-thermodynamic counteractions in Lehar's eddy fluxes

To further investigate the structure of eddy vorticity flux during Lehar's weakening, we examine the horizontal cross-sections of the fluxes of eddy vorticity (shaded) and eddy radial velocity (contours) on the left (Figures 3.9a, 3.9c) at the mid-levels (averaged between 6-10 km) and within the BL (averaged between 0-2 km). These plots are then compared against their thermodynamic counterparts with eddy moist-entropy (θ_e, shaded), and eddy radial and vertical velocity (contours) plotted on the right (Figures 3.9b and 3.9d respectively). These plots are also time-averaged between 24-36 hours (start of RW in Lehar). The deep-shear vector during this period points northwestward. Since the radial eddy vorticity flux is the covariance between eddy vorticity (ζ') and eddy radial velocity (u'), a positive tendency in Figure 3.8c is the result of inflow being correlated with positive vorticity or outflow being correlated with negative vorticity.

Figure 3.9a shows that in the mid-levels for radii ≤ 72 km, inflow (black contours) is strongly correlated with positive eddy vorticity in the downshear region and the negative eddy vorticity is correlated with outflow (golden contours) in the upshear region. On the other hand, Figure 3.9b shows that for the same region, the inflow is strongly correlated with *negative* eddy moist-entropy. Also, the eddy vorticity field is completely out of phase with the eddy moist entropy field. Under such a scenario, there is a destructive interference of the dynamic process by the thermodynamic

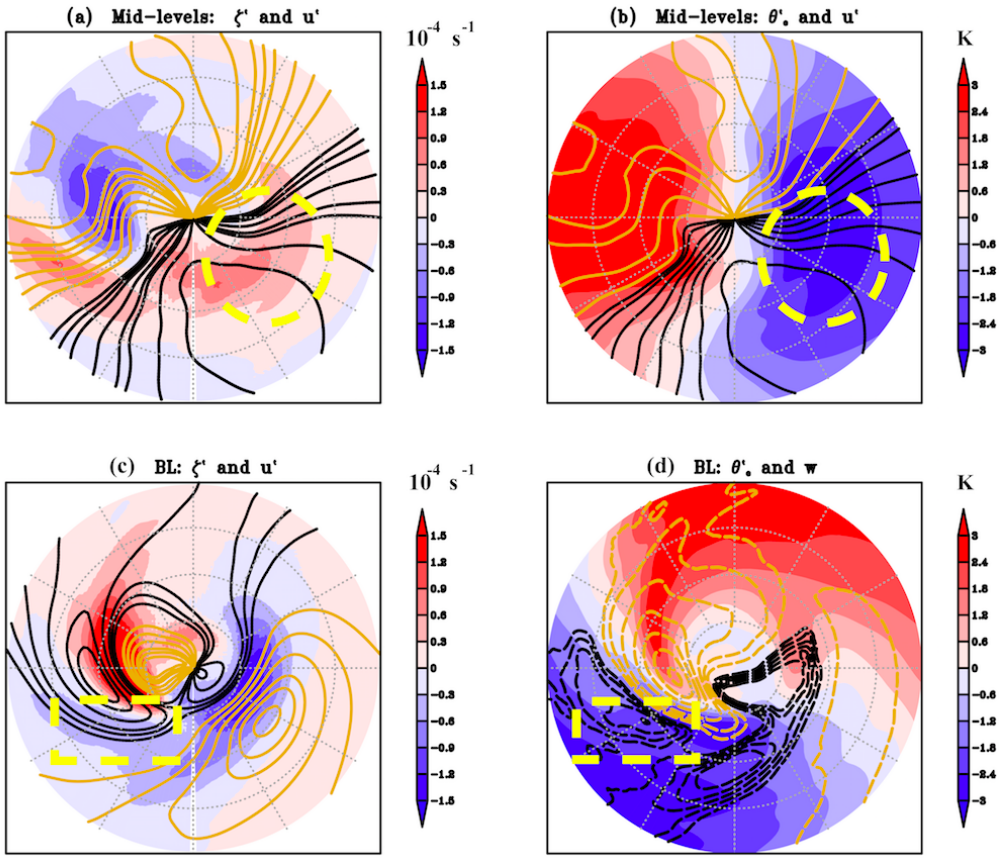

Figure 3.9. Lehar's plan view (r-θ) plots of (a) eddy relative vorticity (shaded) and radial velocity (contours, black represents inflow and golden represents outflow) averaged between 6-10 km (mid-levels) in the vertical, 0 - 120 km radius and 24-36 hours (b) Same as (a) except that the shading represents eddy moist entropy (θ_e). (c) is the same as (a) except that it is vertically averaged within the BL (0 - 2 km). (d) shows the plot of eddy moist entropy (shaded) and vertical velocity (dashed contours) within the BL. Highlighted, are the regions where the inflow carries the positive eddy vorticity (a) and negative eddy θ_e (b) in the mid-levels. Also highlighted is the region within the BL where the inflow contours are juxtaposed with negative eddy vorticity (c), negative eddy moist entropy and downdrafts (d).

processes. This is an important finding as it reveals that the rapid weakening may occur in a sheared environment even if the conditions are dynamically favorable. Within the BL, the phasing in eddy vorticity and eddy moist entropy fields are aligned.

Here, the BL inflow (black contours, highlighted region in 3.9c) is correlated with negative vorticity (blue shaded region in 3.9c), negative eddy moist entropy (blue shaded region in 3.9d), and downward motion (black, dashed contours in 3.9d). Such a configuration within the BL creates the dynamic-thermodynamic pathway for the intruding low θ_e air in the TC environment to trigger the spin-down of the vortex. Between the mid-levels and the BL, the ζ' fields are completely out of phase and the θ_e' fields are 90 degrees out of phase.

How is the thermodynamic weakening of this heat engine reflected in the kinematics of the storm?

A key takeaway from the above discussion is that as shear reorganizes the fields of vorticity, θ_e, radial velocity, and the convective upward/downward motions in the azimuthal direction, looking for signatures in the individual fields might be misleading given the competing nature of the mechanisms associated with these fields. Rather, we must attempt to understand the juxtaposition of these asymmetric fields and how their behavior evolves in the context of one another and the external environment. However, the dynamic and thermodynamic impacts of shear and the intruding low θ_e air cannot be isolated. For example, previous studies such as [77] and [83] have postulated thermodynamic pathways through which low θ_e air intrudes into the vortex of a sheared storm and acts as an anti-fuel to the heat engine, that is the TC. To this, one might ask '*But how is the weakening of this heat engine reflected in the kinematics of the storm?*' In other words, if the dynamic perspective offered in Equation 3.1 completely describes the tendency of tangential momentum, *which term of Equation 3.1 does the low θ_e air impact negatively?*

Our understanding is that the ingestion of low θ_e air acts to reduce the static stability within the BL and has a direct impact on the strength of the updrafts that transport the tangential momentum in the vertical direction. During the initial period of weakening, a reasonably strong inflow is required to transport the low θ_e air into

the vortex core. From this perspective, we speculate that the first terms to show negative tendencies of low θ_e air intrusion are the mean and eddy vertical flux terms (Terms 2 and 4 in Eq. 3.1). Since the downdrafts that transport the low θ_e air are constrained in the azimuth to specific quadrants (upshear left in the case of Lehar, see Section 3.1.1), it is likely that the negative tendency is first visible in the eddy vertical transport term (cf. Figure 3.8d - radius 40-120 km, 0-5 km in the vertical). As the radial pressure gradient reduces as a result of reduced deep convection, the strength of the inflow reduces in an azimuthally averaged sense and a negative tendency is seen in the mean radial advection of vorticity (Term 1). The above discussion serves as an example of the direction we should take in the future and bring the dynamic and thermodynamic perspectives together to account for nonlinear, competing processes that seek to act simultaneously.

3.2 Intrinsic asymmetries

TC Phailin serves as a case study of a low-sheared vortex that rapidly intensified over the ocean. We first seek to understand if the diagnostics derived from Lehar apply here. If not, what are the alternative diagnostics that link the behavior of the intrinsic asymmetries to the RI of the vortex?

3.2.1 Thermodynamic aspects

Figures 3.10a and 3.10b show the plot of θ_e (shaded) and vertical velocity contours (radially averaged on either side of the radius of maximum wind) six hours before RI (t=27) and at t=33 (start of RI). What is consistent between the two times, is the presence of relatively high θ_e when compared to Lehar (Figures 3.6a, 3.6b). At t=27, there are strong upward vertical velocities suggestive of bursts of deep convection extending up to 16 km in the west to south (W-S) quadrant and 14 km in the northeast to northwest (NE-NW) quadrant. Six hours later, this deep convection has wrapped around and extended to all the quadrants - a feature that is entirely

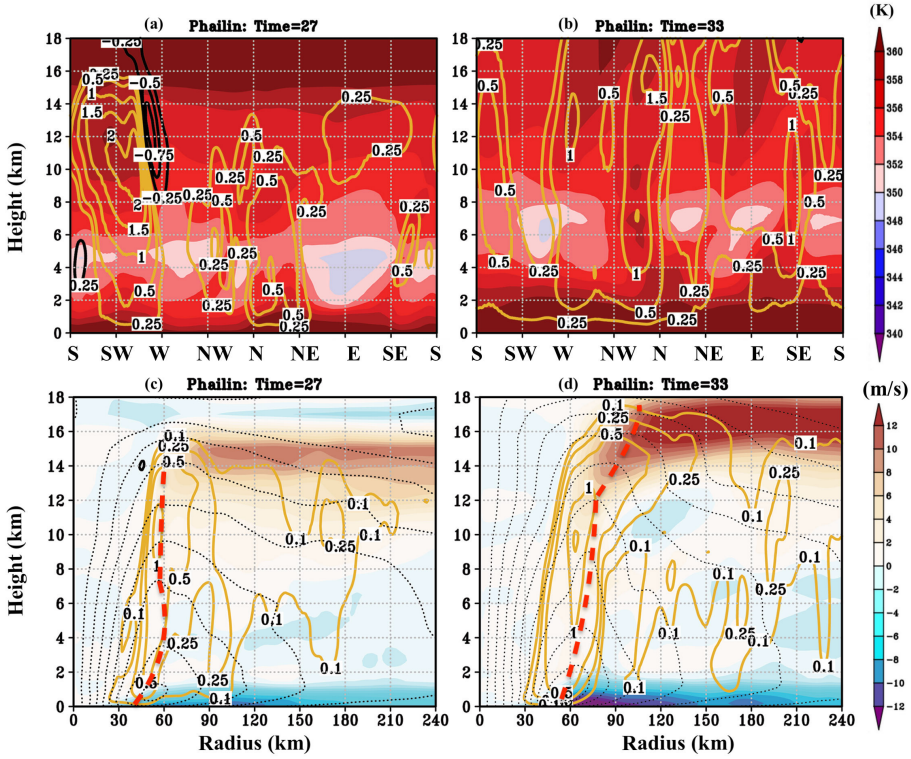

Figure 3.10. (a,b) Azimuth-height plots of Phailin's θ_e (shaded) and vertical velocities at t = 27 (six hours before the RI) and at t=33 (start of RI). Panels c and d present the azimuthal-averaged, radial-height cross-section of Phailin's radial velocities for the same times. Also highlighted are the radii of maximum winds at each height.

absent in Lehar. In Lehar, the initiated updrafts die down in the USL and USR quadrants, due to the predominance of downdrafts carrying low θ_e. This signature of deep convection wrapping around in rapidly intensifying TCs was also noted in Leighton et al. (2018) [33] and Wadler et al. (2018) [64]. At this juncture, it is important to note that unlike Lehar, when the azimuthal variations in boundary layer moist-entropy, inflow, and convection are low in Phailin's low-sheared vortex, the azimuth-height perspective does not offer much insight. This suggests that symmetry dominates in Phailin as opposed to Lehar being dominate by asymmetry.

Instead, Figures 3.10c and 3.10d present the azimuthal-averaged, radial-height cross-section of Phailin's radial velocity at times 27 and 33. They serve to illustrate

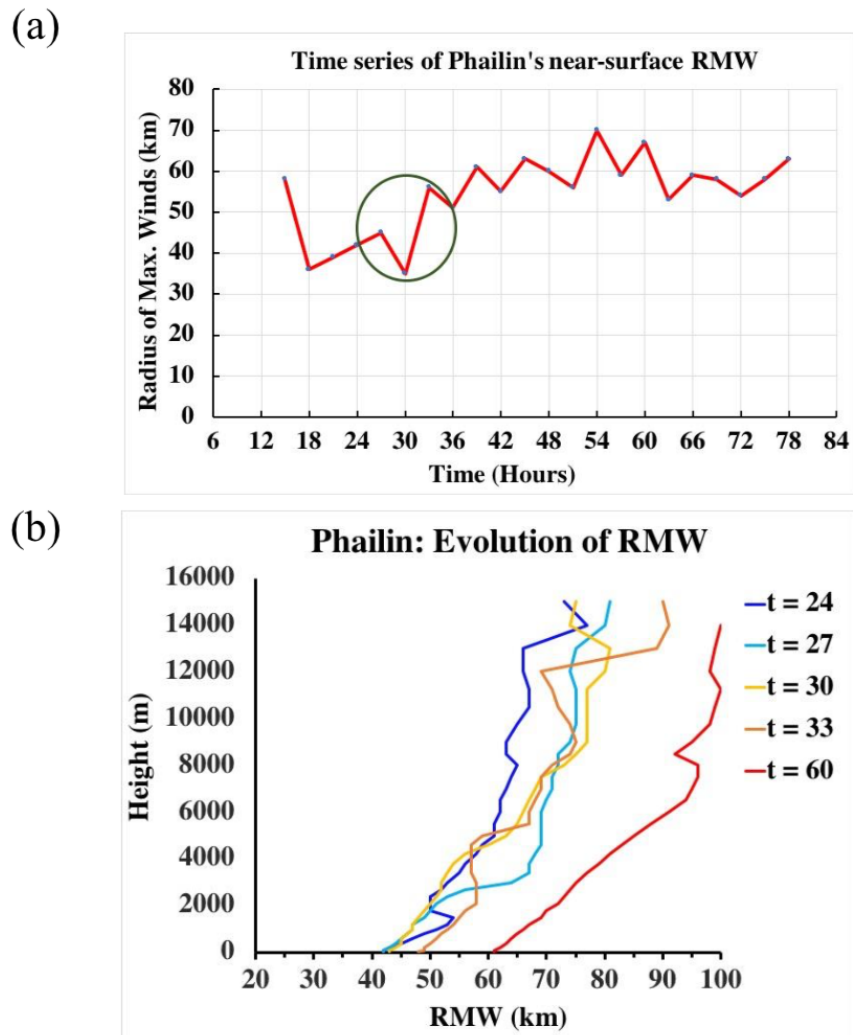

Figure 3.11. (a) Time-series plot of the 10-m radius of maximum winds (RMW) for Phailin. Highlighted, are times: 27 to 33 where there is an eyewall replacement cycle. (b) RMW computed at each height at various times as the storm intensifies. These Figures serve to illustrate the expansion of Phailin's RMW during its intensification.

the importance of the inflow magnitude and radial profile of convergence within the boundary layer. Also highlighted, is the RMW for each of the times. The time-series of near-surface RMW for Phailin (3.11) indicates that Phailin underwent an eyewall replacement cycle with the RMW fluctuating from 42 at t=27 to 35 at t=30, before rising to 56 at t=33 (See 3.11b for variation of RMW across different heights between

these times). While one might expect that the RMW shrinks during intensification in a prototypical intensification problem (following angular momentum conservation arguments), an eyewall replacement cycle can cause the RMW to expand and the TC to intensify at the same time.

According to Shapiro and Willoughby (1982) [89], either a heat source (such as convection) or a momentum source (such as inflow within the boundary layer) can cause the RMW to contract or expand. For example, if there is an additional heat source (convection) at an outer radius during a secondary eyewall formation, it is entirely plausible that the RMW expands and the tangential winds increase at the same time. Further, it must be noted that the angular momentum within the boundary layer is not conserved. Therefore, a more reliable method of understanding the intensification process is using the evolution of azimuthally-averaged, angular momentum surfaces (M-surfaces, see Figure 13 in Montgomery and Smith, 2014) [90]. Figure 3.12 serves to demonstrate that the angular momentum surfaces move inwards in the case of Phailin, as the TC intensifies regardless of the expansion in its RMW. Note that this expansion in the RMW during the RI period is consistent with the conclusions of Stern et al. (2015) [91] although their focus was mainly on the ceasing of the contraction of the RMW rather than its expansion.

A key point to note is that while Phailin's absolute radius of the location of deep convection did not vary much between t=27 and t=33, the relative location of the convection with respect to the RMW was far more radially inward at t=33 (Figure 3.10d), as compared to t=27 (Figure 3.10c). On the other hand, the radial location of the peak inflow within the boundary layer, shifted outward when the magnitude of inflow increased by about 6 m/s (Figure 3.10d). Previous studies have demonstrated that the region within the RMW offers a more conducive environment for deep convection to develop and sustain, resulting in RI [92,93]. Figure 3.13 builds on these studies and serves to explain as to why the convection occurring within the RMW is particularly effective in spinning up the vortex rapidly.

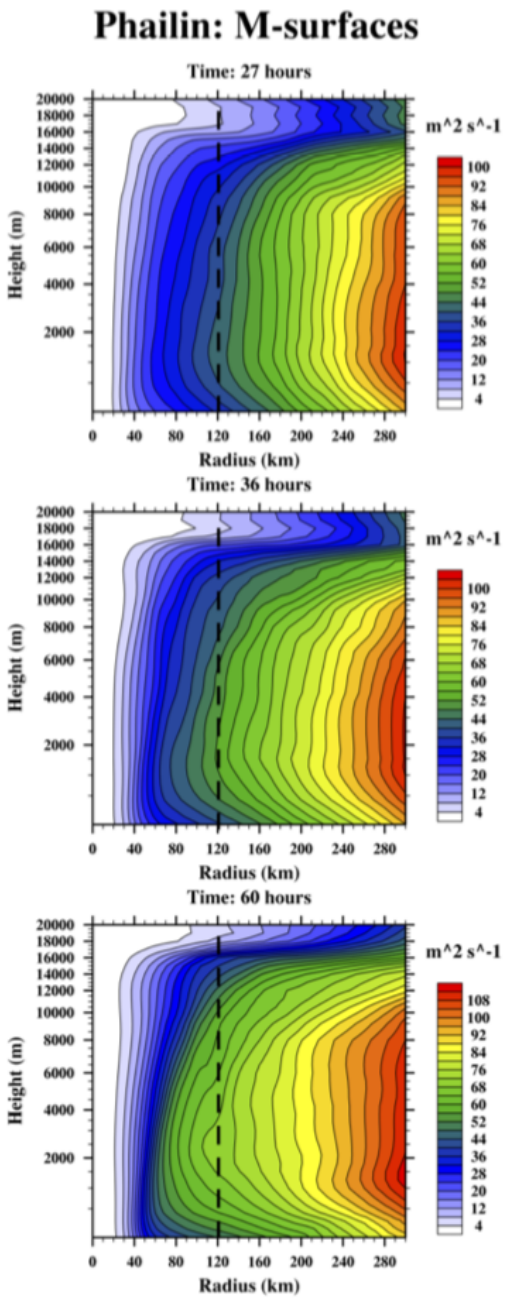

Figure 3.12. Inward motion of Phailin's angular momentum surfaces as it intensifies. Radius-Height plots of azimuthally-averaged angular momentum at times t=27, t=36, t=60 hours.

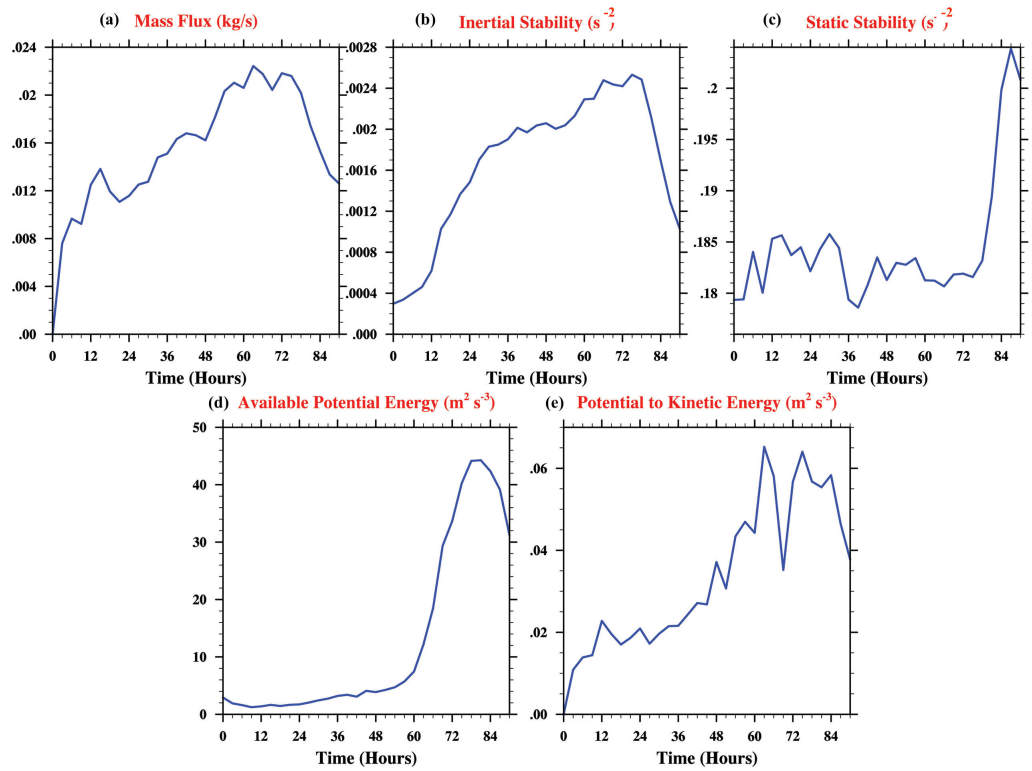

Figure 3.13. Time-series plots (averaged in the azimuthal, radial and vertical directions) for Phailin. (a) Vertical Mass flux in kg/s (b) Inertial stability, I^2 within the radius of maximum winds (s^{-2}) (c) Static stability, N^2 within the radius of maximum winds (s^{-2}) (d) Generation of available potential energy (m^2s^{-3}) (e) Conversion from potential to kinetic energy (m^2s^{-3}).

Figure 3.13a first shows the time-series of the magnitude of mass flux that is being advected upward within the RMW. As the convection wraps around (cf. Figure 3.10b), there is increased symmetry in latent heating and more mass flux is advected upwards. This increased mass flux is indicative of stronger convection (and secondary circulation) that subsequently leads to a higher radial pressure gradient within the boundary layer and stronger inflow within the boundary layer (cf. Figure 3.10d). This convergence within the boundary layer is an agradient flow and boundary layer dynamics heavily influence its magnitude and radial location [5]. A possible (but

neither definitive nor exhaustive) explanation of why the RMW might expand during the RI period might be that with increasing mass flux, the area required to support such a magnitude of mass flux must increase. Ergo, the RMW expands to support such an intensification beyond a certain stage.

Figures 3.13b and 3.13c show the time-series of inertial and static stability within the RMW respectively. Figures 3.13b and 3.13c affirm that the RMW is a region of high inertial (Figure 3.13b) and low static stability. Thus, during the RI phase, when the convection occurs in this region of high inertial and low static stability, there is a higher horizontal and lower vertical resistance for the air parcels [92, 93]. This results in increased upward motion that reflects as increased available potential energy (Figure 3.13d) and an increased conversion from potential to kinetic energy (Figure 3.13e), indicating the increase in the spin of the TC vortex.

Summary

In the case of Phailin where the azimuthal variations were low, the inflow magnitude and radial location of boundary layer convergence relative to the radius of maximum wind played a dominant role in the intensification process. Additionally, a strong coupling between various vertical levels of the vortex ensures that the momentum generated within the boundary layer is advected by deep convection in the vertical direction, as with the case of Phailin. On the contrary, if the upper portions of the vortex are destroyed (by shear, for example) as in Lehar, the three critical elements required for intensification - deep enough convection, wrapping of this convection, and the transfer of momentum from the boundary layer to the upper portions of the vortex, are absent (Figure 3.14).

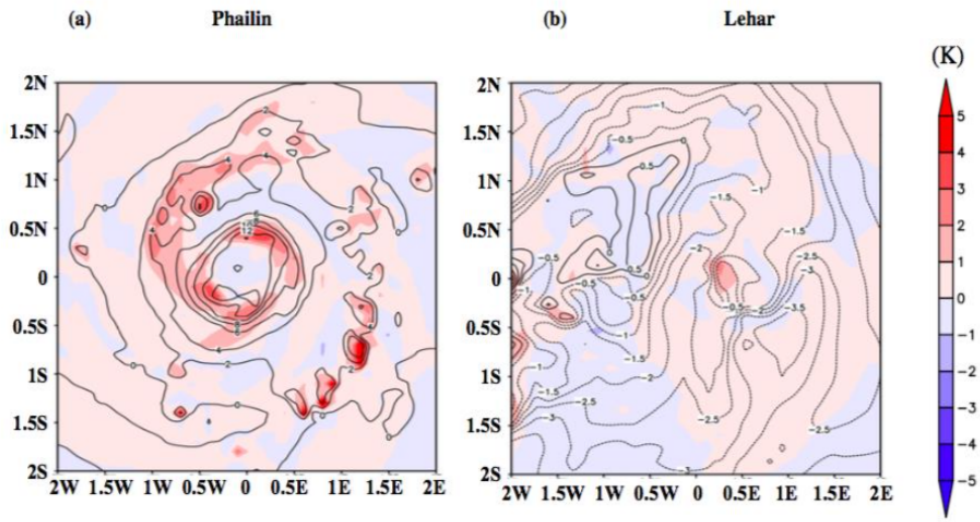

Figure 3.14. Plot of vertical velocities (shaded, in m/s) and equivalent potential temperature anomalies (contours, in K) highlighting the updrafts and downdrafts at the start of intensification (t = 33 hours) for Phailin and at the start of weakening (t = 27) for Lehar. The intense red spots indicate the vortex-scale deep convective updrafts. The moderate red regions indicate the moderate, mesoscale upward motion. The moderately blue regions indicate the downward motion. This Figure serves to illustrate the importance of the upper level configuration for the wrapping of convection. While the upper level configuration was conducive for the wrapping of convection in Phailin (a), the destruction of the upper level features due to shear in Lehar (b) do not allow for the development of these pockets of convection.

3.2.2 Dynamic aspects

In this subsection, we examine the vortex-scale dynamic processes responsible for Phailin's RI using the tangential momentum equation described previously (Section 3.1.2). Figure 3.15 shows the radius-height plots of each of the terms in Eq. 3.1 for Phailin, time-averaged during the initial RI period (27-39 hours). The net tendency in Figure 3.15f indicates the difference in $\langle v \rangle$ over the time-period of interest. This tendency is positive on either side of the radius of maximum wind (RMW), with the maximum values (1 $ms^{-1}h^{-1}$ and higher) straddling the RMW within the BL.

These strong positive tendencies are the result of a strong inward flux of mean vorticity within the BL (Figure 3.15a). As air parcels from outer radii converge to smaller radii within the BL due to the radial pressure gradient, a diminution of momentum occurs due to BL friction (Figure 3.15e), and the eddy terms (Figure 3.15d, 0-2 km height, 60-240 km radii). Despite the losses within the BL, [94] show that the lower tropospheric convergence associated with organized convection along the inner eyewall results in the generation of supergradient winds in a region above the surface layer. This implies that the strongest tangential winds exist in close (vertical) proximity to the weakest tangential winds within the BL. Such a sharp vertical gradient in the tangential velocity ($\frac{\partial \langle v \rangle}{\partial z}$) is seen as a negative tendency in Figure 3.15b between 40-240 km radii, 0-1.5 km in the vertical). This spin-up of the tangential wind within the BL despite the above-mentioned weakening effects, has been referred to as the boundary-layer spin-up mechanism in [32] and references therein.

The vorticity generated within the BL is then transported to the upper portions of the vortex by deep-convection and this reflects as a strong positive tendency in Figure 3.15b on either side of the RMW. Radially outward motion in the upper-levels (12-16 km in the vertical, Figure 3.15a) and subsidence in the eye (radii ≤ 30 km, Figure 3.15) contribute to the negative tendencies in these terms. Figures 3.15c and 3.15d serve to illustrate the contribution of the eddy radial and vertical terms respectively. It is important to understand that the radial and vertical eddy terms are intrinsically coupled. For example, previous studies [21, 25, 95, 96] have shown that *radially* inward and outward-propagating gravity waves manifest as a result of the inner-core non-hydrostatic, *vertical* convective bursts. These gravity waves along with vortex-Rossby waves (that arise due to gradients in potential vorticity, see e.g., [97]) and others serve to transport and reorganize the fields of momentum, energy, vorticity etc. in radial, vertical and azimuthal directions.

Examination of Figure 3.15c suggests that within the boundary layer, the radially inward transport of vorticity by the eddy terms results in a positive contribution,

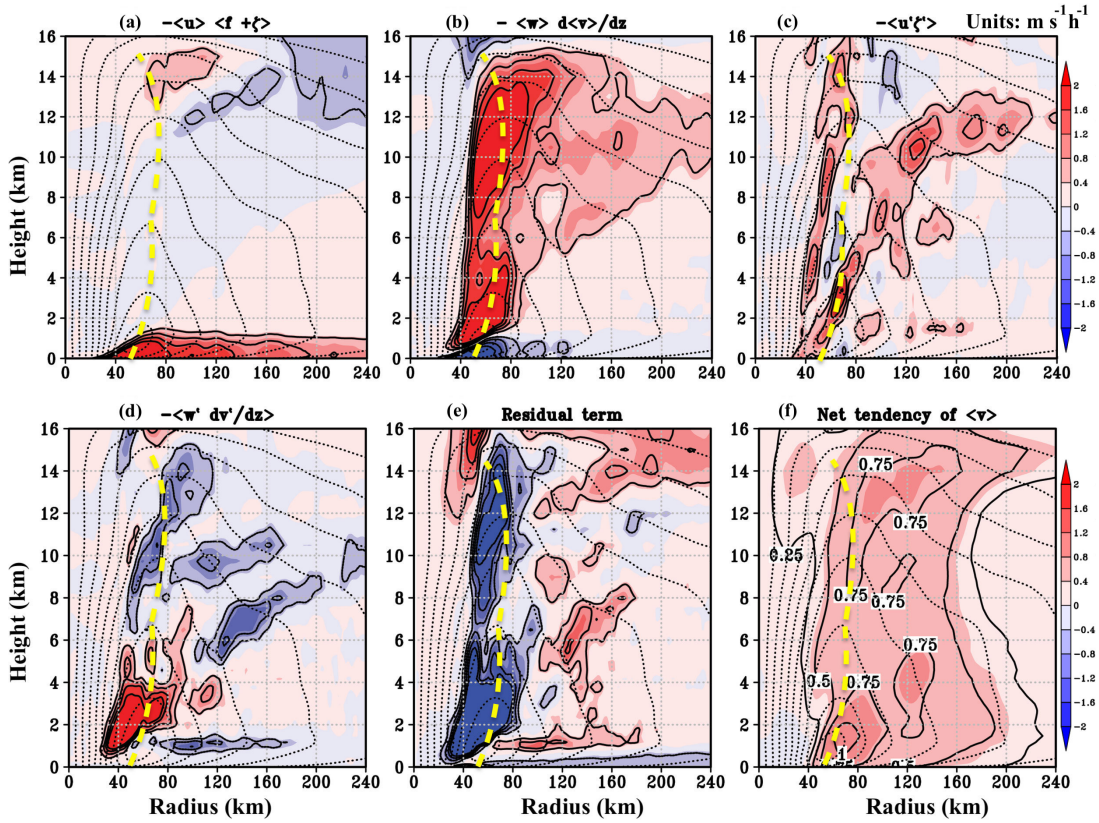

Figure 3.15. Radius-height plots of the terms of the tangential momentum ($\langle v \rangle$) budget time-averaged during the initial period (27 - 39 hours) of Phailin's RI. (a) Mean radial vorticity flux ($V_{m\zeta}$) (b) vertical advection of tangential momentum by the mean secondary circulation (V_{mv}) (c) the eddy radial vorticity flux ($V_{e\zeta}$), (d) the eddy vertical advection of tangential momentum (V_{ev}) (e) Residual terms (f) Net tendency in $\langle v \rangle$ over the period of interest. Units for all panels is $ms^{-1}h^{-1}$ and the contour intervals are 0.5 $ms^{-1}h^{-1}$. The dotted lines represent the $\langle v \rangle$ contours and the yellow dashed line represents the radius of maximum $\langle v \rangle$ at each height.

but the magnitudes are much smaller as compared to the mean terms (especially for radii $\geq$ 80 km (cf. Figure 3.15a). However, the eddy radial vorticity fluxes contribute significantly to the spin-up of the vortex along two distinct radially outward-sloping regions that extend to heights well above the BL (Figure 3.15c). The two distinct wall-like regions correspond to Phailin's concentric eyewalls during this period of time

(cf. Figure 3.11). These regions of positive vorticity act to spin-up and amplify the bursts of deep convection occurring just within the two concentric eyewalls (cf. Figure 3.15b). Similarly, the positive contribution in the vertical eddy term (Figure 3.15d) can be linked to the asymmetric bursts of convection that also serve to transport the tangential momentum from the BL to the upper portions of the vortex.

To address the contribution of these flux terms towards a system-scale growth in cyclonic vorticity, we look to the vorticity equation in its flux form [98, 99]. The (Eulerian) flux form of the vorticity tendency equation essentially represents the forces that contribute to or disrupt the concentration of vertical vorticity (ζ_z) within a defined area of interest and is represented as

$$\frac{\partial \zeta_z}{\partial t} = -\nabla_h.(v_h\zeta_z - \zeta_h v_z + k \times F_{fri}) - (\nabla_h\theta \times \nabla_h(C_p\frac{T}{\theta}))_z \tag{3.2}$$

where the subscripts h and z represent the horizontal and vertical components of the variables of interest (velocity (v), vorticity (ζ), temperature (T), and potential temperature θ). Here, the first term on the right represents the horizontal advective flux that represents the combined effect of the simple transport of vertical vorticity by mean or eddy horizontal flow ($v_h\nabla_h.\zeta_z$) and the effect of vortex stretching ($\zeta_z\nabla_h.v_h$). Note that the stretching term doesn't appear explicitly in this flux form of the vorticity tendency equation. The second term ($\nabla_h.\zeta_h v_z$) represents the vortex tilting that occurs as the upward motion curves the horizontal vorticity contours. The third term represents the divergence of turbulent Reynolds stress due to friction that is predominant close to the surface and the last term represents the baroclinic generation term that is important within regions of high baroclinity such as the eyewall. Following Stokes' theorem, an increase in the areal concentration of vorticity results in a change in the system-scale circulation (line integral of the tangential velocity across the loop encircling the region of interest) and by extension, the azimuthally-averaged tangential wind.

Our analysis of the azimuthally-averaged tangential wind tells us the symmetric and asymmetric contributions towards a system-scale spin-up and an upscale concen-

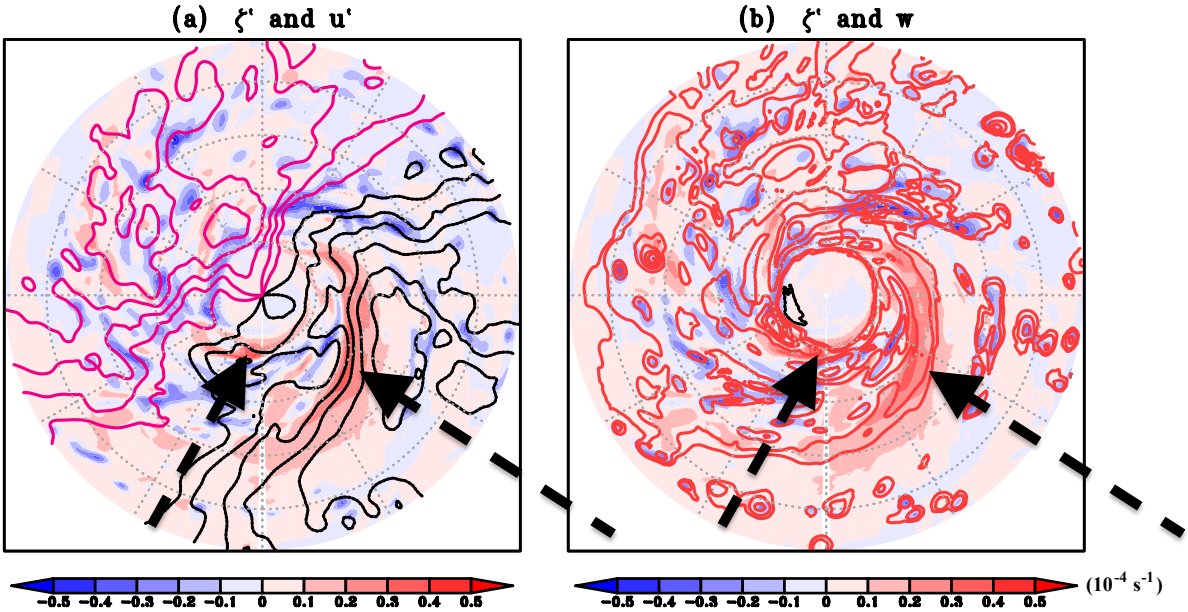

Figure 3.16. Phailin's plan view plots of (a) eddy relative vorticity (shaded, positive regions represent cyclonic direction) and eddy radial velocity (contours, black contours represent inflow and pink represents outflow) (b) eddy vorticity (shaded) and vertical velocity (contours, red contours represents upward motion). These plots are averaged between 4 and 12 km in the vertical for the RI period (27-39 hours) corresponding to Figure 3.15c. The dashed arrows highlight the regions of positive correlation between eddy inflow, cyclonic eddy vorticity and upward vertical velocity. Units of eddy vorticity are $10^{-4}s^{-1}$.

tration of cyclonic vorticity. From this perspective, the radial eddy flux terms play a particularly important role in radially advecting positive vorticity across the loop that encircles region of interest thereby increasing the circulation. But more importantly, the eddy terms radially transporting positive (cyclonic) vorticity into regions of strong, positive (upward) vertical velocities. Such a juxtaposition of the positive vorticity and vertical velocity is further elucidated in Figure 3.16. Here, the plan view plots of eddy relative vorticity and eddy radial velocity reveal that the positive contribution from the radial eddy vorticity term is due to the positive correlation between the eddy inflow and positive cyclonic eddy vorticity (black contours and red shaded regions in Figure 3.16a) and a positive correlation between eddy outflow and negative eddy vorticity (pink contours and blue shaded regions in Figure 3.16a).

Figure 3.16b further illustrates that the regions where the inflow and positive vorticity are collocated are also juxtaposed with updrafts. Thus, the individual vortical convective updrafts are tilted as the horizontally advected vorticity contours are curved by upward motions (Term 2 on the right of equation 3.2; Also, see discussion surrounding Figure 1 in [100]).

Summary

The eddy terms in Phailin compliment the mean terms by positively contributing to a growth in the concentration of vorticity (thereby increasing the circulation across the loop) and by vertically transporting the horizontal momentum generated in the BL to the upper portions of the vortex. Here, the juxtaposition of the (positive) eddy relative vorticity, (positive) eddy moist-entropy and upward vertical velocity positively influence the spin of the vortex through the depth of the vortex along the eyewall regions.

4 SPECTRAL CHARACTERISTICS OF ASYMMETRIES

(A version of this chapter is published in the Journal of the Atmospheric Sciences)

An alternative approach to the dynamical framework presented in the previous section is an energetics approach where there is no separation between the dynamical and thermodynamical factors. For example, regardless of whether the cause of Lehar's weakening was the influx of low θ_e or negative ζ, spin-down of a vortex is a result of the lack of sufficient conversion from potential (PE) to kinetic energy (KE). Additionally, in the dynamical framework, by virtue of Reynolds averaging, the effect of all the asymmetries are condensed to one (prime) term. However, such an approach fails to highlight the differences in the role of asymmetries at different scales [101]. For example, when individual cloud elements (of the order of a few kilometers, wavenumbers 3 and higher) are organized along with other cloud elements along the azimuth, they act as organized mesoconvective (sub-vortex scale) entities and contribute to the energetics directly at the scale of the hurricane (of the order of hundreds or thousands of kilometers). These organized azimuthal asymmetries (wavenumbers 1,2) in addition to wavenumber (WN) 0, explain around 85 percent of the total azimuthal variance in convection [27]. This implies that wavenumbers 0,1,2 are those that have a direct impact at a vortex-scale.

4.1 Power spectral Analysis

Rainwater mixing ratio (Q_r) in high-resolution, near-cloud resolving modeling outputs, carries the signature of these individual and organized mesoconvective elements and is used here as a proxy for convection[1] (Figures 4.1a, 4.1b). An illustration

[1]Alternatively, one may use reflectivity, vertical velocity, vertical mass flux, or diabatic heating as a proxy for convection

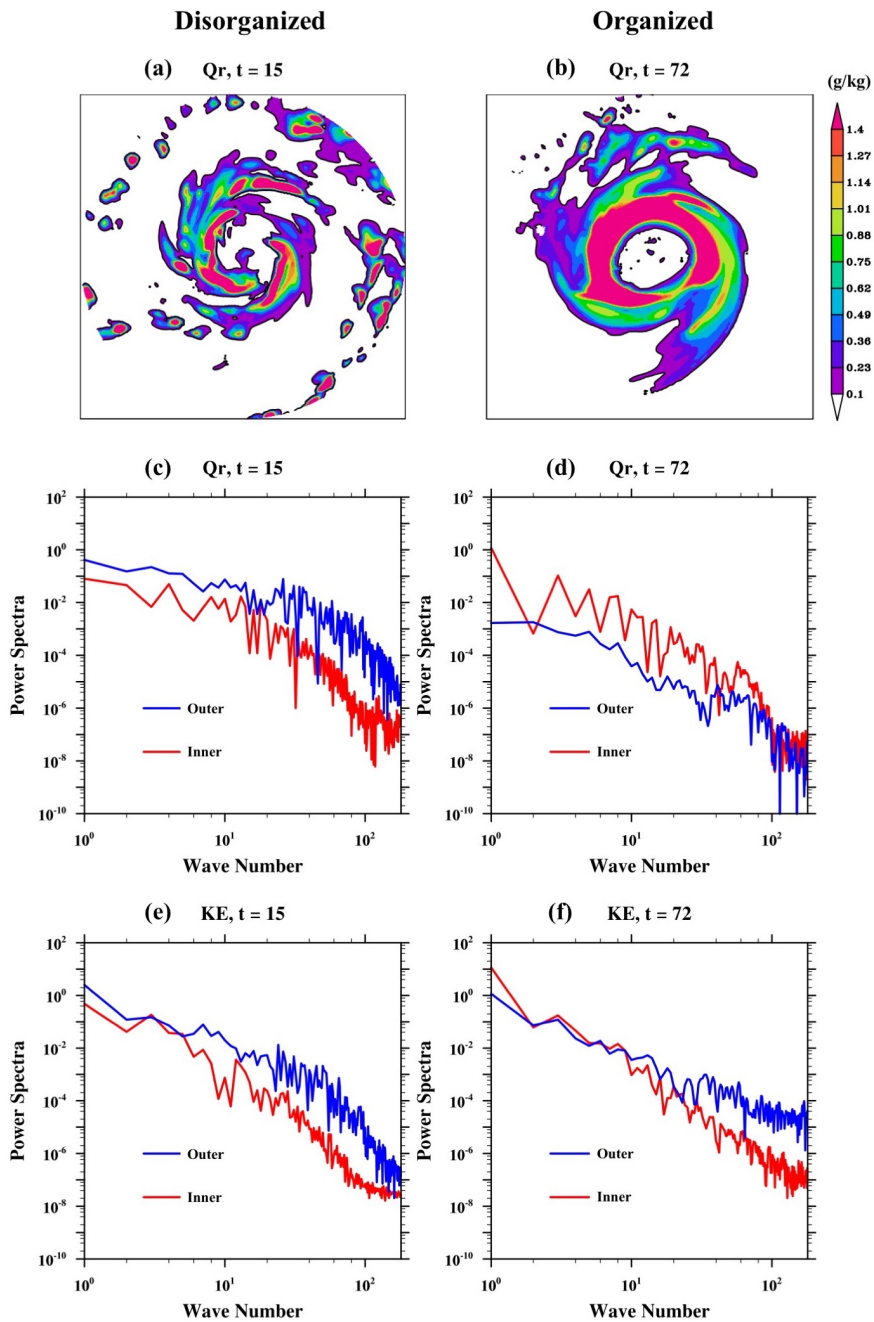

Figure 4.1. (a,b) Plot of Phailin's vertically integrated cloud-water mixing ratio (Q_r) at t = 15 during a disorganized phase (a) and at t = 72 during its peak intensity. (c,d) present a power spectra of Q_r as a function of wave number (WNs 1 to 180) corresponding to panels (a) and (b) averaged radially between 0-200 km (inner region) and 200-300 (outer rain band region). (e,f) show a power spectra of kinetic energy for the times corresponding to (c,d). The axes are plotted in a logarithmic scale to show the differences in the order of magnitude across the wavenumbers.

of Phailin's power spectra of the variance in asymmetric convection (Q_r) and eddy kinetic energy as it transitions from a disorganized phase to an organized phase is presented in Figures 4.1c-f. These spectral plots are computed separately for the inner-core region (0-200 km) and outer rainband region (200 - 300 km). The logarithmic axes indicate the differences in the order of magnitude in power between wavenumber 1 to 180 (The $d\theta$ here is 1 degree; As a result, there are 360 wavenumbers out of which 180 are unique and the rest are their complex conjugates).

At t=15 (Figure 4.1c), the power in the first ten wavenumbers is of the same order of magnitude. As Phailin gets more organized (Figure 4.1d), there is an upscale transfer of power (of Q_r) in the lower wavenumbers and a sharp decrease in power in the higher wavenumbers. As the initially disorganized vortical convective elements at outer radii aggregate, more mass flux is ventilated upwards and as the radial pressure gradient in the boundary layer increases in response to this, there is convergence within the boundary layer. This convergence draws the aggregated vortical convective elements to inner radii. This phenomenon is seen in (Figure 4.1d) where the power in the outer radii (blue line) reduces by several orders of magnitude as the power in the lower wavenumber (particularly wavenumber 1) increases.

Additionally, as a result of aggregation and convergence, the power in wavenumbers 10 and higher located in the outer rain band region drops significantly (roughly four orders of magnitude). Figures 4.1e and 4.1f show the power spectra in kinetic energy for the same times. In the inner core region (red lines), there is an order of magnitude increase in the kinetic energy of wavenumber 1 and a persistent decrease in the powers of the higher wavenumbers. On the other hand, between the time-periods where the TC is organized and disorganized, the kinetic energies in the higher wavenumbers in the outer rain band region (blue lines) *increase* (Figures 4.1e and 4.1f). This is in contrast to the power spectra of Q_r where the power in the higher wavenumbers decreases drastically (4.1c and 4.1d).

4.2 Scale Interactions

Scale interactions is a formalism that describes the different pathways of energy exchange in the wavenumber domain *at,* and *between* asymmetries of various length-scales. Saltzman (1957) [101] laid the foundation for this framework but applied it to a global domain and used a spherical coordinate system to study the energy exchanged between synoptic-scale zonally averaged flows and associated waves. Krishnamurti et al. [27] retailored the same for a hurricane, by casting the system of equations in a storm-centric, cylindrical coordinate system thereby enabling the study of azimuthal asymmetries. Since the intensity of the TC is directly linked to the kinetic energy (KE), we symbolically list the different types of energy exchanges that can impact the kinetic energy of the mean flow (Equation 4.1) and asymmetries at any scale (Equation 4.2).

$$\frac{\partial K_0}{\partial t} = -\sum_{n=1}^{N} < K_0 \rightarrow K_n > + < P_0 \rightarrow K_0 > - < K_0 \rightarrow F_0 > \tag{4.1}$$

$$\frac{\partial K_n}{\partial t} =< K_0 \rightarrow K_n > + < K_{k,m} \rightarrow K_n > + < P_n \rightarrow K_n > - < K_n \rightarrow F_n > \tag{4.2}$$

Here, the K_0 and K_n represent the kinetic energy of wavenumber 0 (mean flow) and wave number n respectively. K_m and K_k are the kinetic energies of wavenumbers m and k that interact with wavenumber n as a triad. Likewise, P_0 and P_n represent the potential energy of wavenumber 0 and wave number n. The terms in angular brackets indicate exchanges that are positive in the direction of the arrow. Equation 4.1 shows that the KE of the mean flow (WN 0) could either change due to the transactions of KE with other scales (known as cross-scale interactions), due to a conversion of available potential energy (APE) to KE on the scale of the mean flow (known as in-scale energy exchange), and frictional dissipation (F_0). The complete formal equations of the above exchanges can be found in the appendix at the end of this section (Equations 4.3 to 4.16).

The mean to eddy exchange of KE (term 1 in Eqn. 4.1) is a barotropic energy exchange that invokes the covariance between the mean motion and the eddy flux of

momentum. The conversion of energy from APE to KE is baroclinic in nature and invokes the covariance between vertical velocity and temperature (vertical overturning). Energy exchanges that happen at an individual scale are quadratic nonlinearities and are known as in-scale exchanges. Term 1 in Eqn. 4.2 is the same as Term 1 in Eqn. 4.1 except that it has an opposite sign (mean's loss is eddy's gain). Term 2 in Eqn. 4.2 represents the nonlinear exchange of KE among different scales. Energy interactions between the eddy scales occur via triad interactions that follow certain trigonometric rules. For example, wave numbers n, m and k can interact if and only if k + m = n, or -k + m = n, or k - m = n [101]. These exchanges invoke triple products and are known as cross-scale interactions. Term 3 in Eqn. 4.2 represents the baroclinic exchanges between APE to KE at each of the wavenumbers (n =1 to N) and the last term is the loss to friction.

The following methodology is adopted to address the role of asymmetries during TC rapid intensity changes using the formalism of scale interactions. High-resolution HWRF outputs of the desired storms of interest are taken and the necessary variables are projected on to a storm-centric, cylindrical coordinate system. A Fourier transform is then performed, and the resulting azimuthal harmonics of these variables are classified into three categories: Mean (WN 0); low-wavenumber (WN) asymmetries representing the eddies that are organized at the vortex-scale and are persistent in time (WN 1,2); and higher WNs that are representative of events that transient in nature (WNs 3 and higher) - e.g., corresponding to *individual* convective bursts.

The evolution of the following energy exchanges are computed during periods when there is a significant change in the organization of convection (RI/RW/landfall): (i) Generation of APE from heating (ii) Transfer from APE to KE (iii) Exchange of KE between the mean and eddies (iv) Exchange of KE amongst the asymmetries. The consistent behavior of asymmetries that clearly helps us distinguish RI from RW is presented here.

4.2.1 Generation of APE

The generation of APE is a quadratic, non-linear term just like the baroclinic exchanges described above. This term is computed using the covariance of diabatic heating (H) and temperature (T). Such a generation can happen at every individual scale (in-scale exchange). In other words, every scale can contribute directly to the generation of APE. Figure 4.2 shows the plot of the domain-averaged APE (y-axis) for each forecast time (x-axis) for the wavenumbers associated with the axisymmetric mean (wavenumber 0), low order (wavenumber 1-2) and higher order wavenumbers (wavenumbers ¿2) for TCs Phailin and Lehar. The RI period in Phailin is highlighted in red, and the RW period in Phailin (post-landfall) and Lehar (over the ocean) is highlighted in blue. The landfall time is marked by a dashed, gray line.

Figure 4.2a shows that during Phailin's RI period, there is an increase in the mean generation of APE (red solid line), while the generation term in the asymmetries (blue and green solid lines) is relatively small. However, just before landfall (as the outer rain bands of the TC vortex start interacting with land), there is an increase in the generation of APE both in the lower and higher WNs. An increase in WN 0 implies that during Phailin's RI period, the generation of APE comes from an axisymmetric, organized convection of the clouds along the azimuth. However, as the storm structure is disrupted due to interaction with land, the energy is transferred to the asymmetries. In the case of Phailin, the eddies maintain the storm for a certain time period during and post-landfall (between forecast time of 72 to 84 hours, the amount of APE generated in WNs 1,2 is more than twice the amount generated in mean). Once all the surface fluxes cease to exist over land, the generation term across all WNs drops substantially. However, we know that land is not the only possible disruptor of the organization in convection. Disruption of the organization in convection also occurs when a TC weakens over the ocean, due to adverse environmental influences (e.g., shear, dry air, cold waters or a combination thereof).

Figure 4.2b shows the time-series plots of the generation of APE for TC Lehar where the rapid weakening occurred over the ocean, due to a combination of shear and dry-air intrusion (See Section 3). In Lehar, for the first ∼36 hours, the magnitude of APE generated across all wavenumbers is comparable to that of Phailin's. However, at around 36 hours (more than 24 hours before landfall), there is a marked decrease in the mean generation of APE (red solid line in 4.2b). During this period, there is a corresponding increase in the generation of eddy APE (green and blue lines in 4.2b) almost 16 hours before landfall (∼42 hours). Once again, once the surface fluxes over land have ceased, there is a drastic drop in the generation of APE.

4.2.2 Conversion from APE to KE

The mechanism of transformation from APE to KE in a TC is the baroclinic overturning circulation (warm air rising and cold air sinking). Similar to the vertical advection terms V_{mv} and V_{ev} (Terms 2 and 4) in Equation 3.1, this term relies on the covariance between vertical velocity (w) and temperature (T). This conversion of energy happens at every individual scale through the vertical advection of high tangential momentum from the BL to the rest of the TC vortex.

However, previous studies have identified that there are preferential regions where the generated heating is more suited for conversion to KE ([102]). For example, Miyamoto et al. (2015) [93] showed that when the heating associated with the organized cumulus convection occurs with the RMW, a region of high inertial stability and low static stability, there is a higher likelihood of conversion from PE to KE[2]. Therefore, in a rapidly intensifying TC, one would expect that there is an increased generation of APE from heating and an increased conversion from APE to KE and

[2]Smith et al. (2016) [103] offer an alternative interpretation of heating occurring within the RMW using the evolution of angular momentum (M)-surfaces. As heating occurs within the RMW, the spin-up occurs within the BL and the high momentum is then advected vertically within the eyewall. This results in the M-surfaces being drawn closer and spins-up the regions above the BL as well. Regardless of the explanation as to why diabatic heating within RMW is more conducive for spin-up, our emphasis is on the fact that for the same amount of APE generated, there are preferential regions within the TC vortex that are most suited to the conversion of APE to KE.

vice-versa during RW. Figures 4.2c and 4.2d show the time-series of the magnitude of (domain-averaged within the vortex) conversion from *mean* PE to *mean* KE (red line), and eddy APE to eddy KE (blue and green lines). During the RI period (red shaded region), there is a persistent increase in the magnitude and during the RW period (blue region) post-landfall, there is a clear reduction in magnitude due to a decrease in the ability to sustain deep convection.

Since the spatially-averaged eddy terms in Figures 4.2c and 4.2d are an order of magnitude smaller than the mean terms, Figure 4.3 shows the radius-height plot of the magnitude of conversion from eddy APE to eddy KE during Phailin's RI (Figures 4.3a, 4.3c) and RW (Figures 4.3b, 4.3d) periods. The baroclinic conversion at the lower WNs is shown in Figures 4.3a and 4.3c. The transactions in the higher WNs are illustrated in Figures 4.3b and 4.3d. Figure 4.3 reveals that during the RI period, there is a region of strong positive correlation between w' and T' (40-80 km radii in Figures 4.3a, 4.3b). This positive correlation is the result of organized and disorganized updrafts that extend to the entire depth of the vortex within or near the eyewall region. Note that the peaks in the magnitude of the conversion from APE to KE in the eddy scales are comparable to averaged magnitudes of the conversion in the mean term in Figure 4.2c. Conversely, during the RW period, the ability to sustain deep convection is indicated by the positive transfer from APE to KE restricted to regions within the BL. Above the BL, there is a strong negative correlation (blue shaded region in 4.3c, 4.3d) between w' and T' that indicates the vortex's inability to transfer the tangential eddy momentum from the BL to the mid and upper portions of the vortex.

4.2.3 Mean to eddy kinetic energy transfer

This section focuses on the barotropic exchange in KE between the mean and long waves, and mean and short scales. This exchange invokes the covariance between the azimuthally averaged flows and the eddy convergence of momentum (predominantly

within the BL) in response to the organized and disorganized cumulus convection as discussed in previous sections. In the kinetic energy budget formulation using the standard Reynolds averaging partitioning, this transaction between the mean and eddies would feature as a production term (e.g., see Chapter 5 of [104]). Since the formalism of scale-interactions gives us the flexibility to look at individual scales of asymmetries, it is important to appreciate that the transport of momentum between each individual eddy scale of WN n and WN 0 is a unique transaction, distinct from the transactions between other eddy scales and the mean [101]. In this section, particular emphasis is laid on the direction of transfer between the mean and the asymmetries.

Figure 4.4 shows the radius-height plots of the KE exchange between WN 0 and WNs 1,2 for TC Phailin during its RI phases and for TC Lehar (2013) during its RW phase. In addition to TCs Phailin and Lehar, the same plot is shown for Hurricane Harvey (2017) that underwent an asymmetric RI for the purpose of contrasting symmetric and asymmetric RI. On the right, plots of vertically integrated rainwater mixing ratio (Q_r) are presented corresponding to the time periods on the left. In the R-Z plots, a positive exchange (red) indicates that the direction of transfer is from the mean to low WN asymmetries. Conversely, a negative exchange (blue) indicates that the direction of transfer is from the asymmetries to the mean.

The Q_r plot during Phailin's RI (Figure 4.4a) indicates that Phailin's RI was maintained by azimuthally symmetric convection. During this period, between 30-80 km radii, there is a strong transfer of energy from the eddies to the mean (blue regions). This is quite different from Harvey's RI that is supported by asymmetric convection characterized by WNs 1 and 2 (Figure 4.4b). During this period, the radius-height plot indicates that the direction of energy transfer is from the mean to the eddies (predominant regions of red). The RI configurations in Figures 4.4a and 4.4b are compared to the RW configuration in Lehar (Figure 4.4c). The Q_r plot during Lehar's RW in a sheared environment indicates that the weakening period was characterized by a predominance of WN 1 convective asymmetry. During this period,

there is a strong transfer of kinetic energy from the mean to WNs 1 and 2 (deep red regions). At outer radii within the BL, the direction of transfer is always from mean to the (organized) eddies suggesting a predominance of WN 1 and 2 asymmetries in the rain-band region. The dominance of mean to eddy transactions during Harvey's RI and Lehar's RW simply suggests that organized asymmetries that receive energy from the mean can either lead to RI or RW. While such information is not very useful for the purpose of distinguishing RI from RW, this transaction between the mean and long waves acts as a useful indicator as to whether the intensification or weakening process is symmetric or asymmetric.

Figure 4.5 shows the radius-height plot of TC Phailin's KE exchange between the mean and higher WNs during its RI (Figure 4.5a) and RW (Figure 4.5b) phases. As in Figure 4.4, a positive exchange (red) indicates that the direction of transfer is from the mean to (higher WN) eddies and a negative exchange (blue) indicates that the direction of transfer is from the eddies to the mean. During RI (Figure 4.5a), there is a clear upscale (disorganized eddies at higher WNs to WN 0) transfer of KE within the BL indicating an organization of convective elements. Conversely, during RW (Figure 4.5b), there is a downscale (WN 0 to disorganized eddies at higher WNs) transfer of energy within the BL indicating a disruption in the organization of convection.

Additionally, the asymmetries at the smallest scales play a major role in dissipating the turbulent kinetic energy into internal energy [105]. What we see here, is the bulk signature of the organization and disruption of convection, that dominates the trickle-down effect (from the mean to the smallest of eddies until viscosity dissipates the energy) that occurs at all times in turbulent flows.

4.2.4 Eddy to eddy kinetic energy transfer

This section addresses the cross-scale interactions between the low-WNs and high-WNs. These exchanges are computed using triple products since the exchanges take place in triplets (WN n with WNs m and k). Figure 4.6a presents the time-series

plot of Phailin's kinetic energy transfer from the cloud scales to the long waves. Most importantly, these transactions indicate how the disorganized scales project on to the scales organized at the scale of the TC through upscale or downscale transfers. During Phailin's RI period (shaded in red), there is an upscale transfer from the higher to lower WNs.

On the other hand, during the RW period (shaded in blue), there is a downscale transfer from the lower to higher WNs. Figures 4.6b and 4.6c are the radius-height plots of the same exchange time-averaged during RI and RW respectively. Figure 4.6b suggests that the majority of the upscale KE transfer occurs within the BL with the maximum values straddling the RMW. Likewise, during the weakening phase, the majority of the downscale transfer happens within the BL (radii ≥ 100 km), and in the eyewall region within the RMW where the diabatic heating is concentrated (Figure 4.6c). The upscale and downscale cascade of turbulent kinetic energy described here has also been noted previously in observational analyses of the hurricane boundary layer [106].

The above discussions on the multiple competing modes of energy exchanges that influence the KE at a particular scale reveal an important message regarding the transfer of energy between the mean and eddies: the growth and decay of kinetic energy in the mean or eddy scales need not happen at the expense of one another. Figure 4.7 shows the time-series plot of the net rate of change in KE (computed using Equations 4.1 and 4.2) at WNs 0, 1, 2, and in the cloud scales over the course of Phailin's life-cycle. Importantly, the change in KE in each of the scales is plotted against the rate of change in intensity (cf. with Figure 2.2 for the time-series of intensity) to indicate which scales had the direct impact on intensity change at a particular period in time. Between 0-36 hours, the change in intensity is correlated with an increase in kinetic energy across all the wavenumbers (mean and eddy scales). As expected, during this period, WN 0 is the most dominant scale. However, the net kinetic energy in all the disorganized scales is comparable to that of WN 0. At about 42 hours, the kinetic energy of the mean starts to drop. During this period, the

eddy scales maintain the TC until the intensity starts to drop rapidly after 72 hours. Between 72 and 90 hours when Phailin is over land, the kinetic energy in the mean drops significantly while the energies in the eddy scales continue to grow.

The above discussion is intended to disprove any notion that the eddies only grow at the *expense* of the mean. With this, we reemphasize that if we overlook the multiple competing pathways of energy transfer at a particular scale, the consequent results will lead us to draw incorrect conclusions regarding the very nature of eddies during TC rapid intensity changes.

4.2.5 Order of magnitude analysis

Given the competing nature of the various terms that influence the energetics at and across the various scales within a TC, it is important to understand the relative importance of these terms at various stages in a TC's life-cycle. Figure 4.8 presents such an analysis and underscores the order of magnitudes (only absolute values are presented here) of the various energy transactions that take place over the course of the life-cycles of TC Phailin. In this figure, the darker shades represent the higher orders of magnitude and the lighter shades represent the smaller order of magnitudes. Each of the terms is domain averaged in the R-Z plane within the vortex (0-300 km radii) for the specific periods indicated in the y-axis.

First and foremost, the comparison of the generation of APE in the mean (0), low-WN asymmetries (L), and high-WN asymmetries (S) indicates that the generation in each of these scales is of the same order of magnitude (10^1). The baroclinic conversion terms from APE to KE are one order smaller than the generation term indicating that not all of the PE generated is converted to KE as one would expect. The baroclinic conversion in the mean is one order higher than the asymmetric conversion from PE to KE (10^{-1} in the mean and 10^{-2} in the eddy scales). Interestingly, the barotropic transactions between the mean and eddy scales are the smallest amongst all the transactions (of the order of 10^{-4} or 10^{-5}). This finding is perhaps not very

surprising given that a TC vortex is a largely baroclinic system due to the abundance of buoyant updrafts and corresponding downdrafts.

However, the fact that the barotropic exchanges are so smaller compared to the baroclinic transactions, raises concerns about the previous treatment of the processes of axisymmetrization using purely barotropic models (e.g., [18,107,108]). Our results suggest that the process of axisymmetrization occurs when the mean (WN 0) gains a significant amount of kinetic energy directly from potential energy as an in-scale baroclinic transaction rather than a barotropic transaction from the eddy terms.

On the other hand, the eddy-eddy (across-scale) transactions (last column in Figure 4.8) are of the same order of magnitude as the baroclinic terms (10^{-1} during peak intensity and RI periods and 10^{-2} during other periods). These eddy-eddy transactions are of crucial importance since they represent the mechanism through which the disorganized cloud scales eddies project onto the wavenumbers corresponding to the organized eddies by means of upscale and downscale transfers. Studies using *linear* models that only permit transactions between the mean and eddies (e.g., [30]) or those that purely follow a Reynolds averaging-based treatment of the eddy terms (e.g., [93]) fail to capture this important mode of energy exchange through which the asymmetries influence the system-scale kinetic energy and intensity.

In summary, the dominant processes that impact the TC intensity are the in-scale baroclinic transactions and the across-scale eddy-eddy energy exchanges between organized and disorganized eddies. It must also be noted that the contributions from the higher WNs are non-negligible and should not be ignored. However, given their shorter time-scales, the eddy-eddy cross-scale interactions are particularly important as they are a mechanism by which these higher-order asymmetries project on to the low-WN eddies that are more persistent and predictable.

4.3 Summary

The second framework addresses the same problem from an energetics perspective. The key difference here is that the differences in the behaviors of asymmetries at different scales are accounted for. Here, the asymmetries are classified into scales that are *organized* at the scale of the TC vortex (WNs 1,2) and scales that represent the disorganized or individual cloud scales (WNs 3 and higher). Scale interactions is a formalism wherein the myriad of exchanges of energy *at* and *across* each of the individual scales are computed. A summary of all the key takeaways from this scale interactions perspective is presented in Figure 4.9.

Figure 4.9 seeks to illustrate the consistent behavioral patterns in the asymmetries during RI and RW that may be used for a diagnostic or qualitative prediction of rapid intensity changes. At this point, the sample size is clearly insufficient for drawing statistically significant conclusions. Therefore, the points noted here are just observations from a couple of case-studies. In this schematic, the weight of the arrow represents the magnitude of the energy exchange. During RI, the APE generated is maximum in WN 0 and relatively less in the eddy scales. During RW, the mean APE generated reduces drastically as the organization of convection within the vortex is broken down and the eddy APE increases before decreasing in all scales once the surface fluxes are completely cut off over land. Similarly, between RI and RW, there is a significant drop in the baroclinic conversion from PE to KE across all the scales. The double-sided arrows between the mean and long waves indicate that the direction of transfer between these scales can be either way during RI or RW. This informs us that from a diagnostic/qualitative prediction perspective, the barotropic exchange between the mean and long waves is not a very good indicator/differentiator as to whether the TC is about to undergo RI or RW. However, given that we know the hurricane intensity is described by the low wavenumbers 0,1 and 2, this exchange reveals key information as to whether the TC is maintained by symmetric convection

(all the energy is directed towards WN 0) or by asymmetric convection (energy is directed towards the WNs 1 and 2).

A more consistent and useful signature is the upscale transfers from the cloud scales to the long waves and the mean, and the downscale transfers from the low wavenumbers to higher wavenumbers during RI and RW respectively. The change in sign (upscale or downscale) is illustrated with black and red arrows. The cross-scale interactions are particularly important since they illustrate how the effects of the less-predictable, disorganized cloud scales are projected on to the organized and predictable low WNs. These signatures need to be verified over a large sample of TCs that underwent rapid intensity changes across multiple basins.

Finally, using an order of magnitude analysis we show that the baroclinic transfer terms and the non-linear across-scale eddy-eddy transactions are the dominant mechanisms for the aggregation of convection. These findings are in contrast to the traditional barotropic viewpoint that posits that convective aggregation and axisymmetrization occur primarily through a direct transfer between the mean and the eddies. Such a transaction is shown to be several orders of magnitudes smaller than the two above-mentioned mechanisms.

4.4 Appendix: Pertinent Equations for Scale Interactions

The derivation of equations (4.1) and (4.2) in a storm-centric, cylindrical isobaric framework is presented in [27] in detail. Therefore, we only present the explicit forms of the terms in equations (4.1) and (4.2) used in this study. Please note that the $\frac{v_\theta^2}{r}$ in equation A2 of [27] should have a positive sign in the right hand side of the radial momentum equation; there was a typographical error in their equation.

We will use capital letters to denote Fourier coefficients of the fields represented in corresponding small letters.

(a) The barotropic transactions of kinetic energy between the mean and a given eddy of WN n (cf. term 1 on the right in equations 4.1 and 4.2) is given by

$$< K_0 \rightarrow K_n >= \int_M [\Phi_{v_\theta v_r}(n)\frac{\partial\langle v_\theta\rangle}{\partial r} + \Phi_{v_r v_r}(n)\frac{\partial\langle v_r\rangle}{\partial r} + \Phi_{v_\theta\omega}(n)\frac{\partial\langle v_\theta\rangle}{\partial p} + \Phi_{v_r\omega}(n)\frac{\partial\langle v_r\rangle}{\partial p} + \frac{1}{r}\Phi_{v_\theta v_\theta}(n)\langle v_r\rangle - \frac{1}{r}\Phi_{v_\theta v_r}(n)\langle v_\theta\rangle]\, dM \tag{4.3}$$

Here θ denotes the azimuthal angle, r denotes the radius from the storm center, and p stands for the pressure. The tangential, radial, and vertical components of wind are denoted by v_θ, v_r, and $\omega = \frac{dp}{dt}$. We use variables (v_r,v_θ) in lieu of (u, v) to be consistent with the presentation of [27]. For fields a,b we define $\Phi_{ab}(n) = A(n)B(-n) + A(-n)B(n)$, where A and B are the Fourier coefficients of fields a and b respectively. dM denotes an elementary mass of the domain of interest M.

(b) Defining $\Psi_{ab}(m, n) \equiv A(n - m)B(-n) + A(-n - m)B(n)$, we may express the rate of change of kinetic energy per unit mass, $K(n)$ of a given WN n due to cross-scale nonlinear interactions with all the other WNs other than 0 (cf. second term on the right in equation 4.2) as

$$< K_{k,m} \rightarrow K_n > =$$

$$\int_M \sum_{\substack{m=-\infty \\ m\neq 0}}^{\infty} V_\theta(m)(\frac{1}{r}\Psi_{v_\theta \frac{\partial v_\theta}{\partial \theta}}(m,n) + \Psi_{v_r \frac{\partial v_\theta}{\partial r}}(m,n) + \Psi_{\omega \frac{\partial v_\theta}{\partial p}}(m,n) + \frac{1}{r}\Psi_{v_\theta v_r}(m,n))$$

$$+V_r(m)(\frac{1}{r}\Psi_{v_\theta \frac{\partial v_r}{\partial \theta}}(m,n) + \Psi_{v_r \frac{\partial v_r}{\partial r}}(m,n) + \Psi_{\omega \frac{\partial v_r}{\partial p}}(m,n) - \frac{1}{r}\Psi_{v_\theta v_\theta}(m,n))$$

$$-\frac{1}{r}\frac{\partial}{\partial r} r[V_\theta(m)\Psi_{v_r v_\theta}(m,n) + V_r(m)\Psi_{v_r v_r}(m,n)]$$

$$-\frac{\partial}{\partial p}[V_\theta(m)\Psi_{\omega v_\theta}(m,n) + V_r(m)\Psi_{\omega v_r}(m,n)]\, dM \tag{4.4}$$

(c) The generation of available potential energy (P) for azimuthal WN 0 is calculated as

$$GEN(\ P_0\ ) = \int_M \gamma\ < H - \overline{\overline{H}} >< T - \overline{\overline{T}} >\ dM \tag{4.5}$$

The double overbars indicate a horizontal areal average (inner-domain average up to 300 km radius from the storm center) and angular bracket represents azimuthal mean. H is the diabatic heating rate per unit mass (in K/s) and T is the temperature. γ is the static stability parameter defined as $\gamma = -\frac{\frac{T_{pot}}{T}(\frac{R}{C_p p})}{\frac{\partial T_{pot}}{\partial p}}$. Where T_{pot} is the potential temperature, R is the universal gas constant (287 J/kg K), and C_p is the specific heat at constant pressure (1005 J/kg K).

The generation of available potential energy at any other WN n is expressed as

$$GEN(\ P_n\ ) = \int_M \gamma\ \Phi_{HT}(n)\, dM \tag{4.6}$$

(d) The baroclinic, in-scale conversion from available potential to kinetic energy at WN 0 (cf. term 2 on the right in equation 4.1) is given by:

$$< P_0 \rightarrow K_0 > = -\int_M \frac{C_p}{p} < \omega - \overline{\overline{\omega}} >< T - \overline{\overline{T}} >\ dM \tag{4.7}$$

For all other scales (cf. term 3 on the right in equation 4.1),

$$< P_n \rightarrow K_n > = -\int_M \frac{C_p}{p}\Phi_{\omega T}(n)\, dM \tag{4.8}$$

The $\Phi_{HT}(n)$ and $\Phi_{\omega T}(n)$ (in Equations 4.6 and 4.8) are a more accurate representation than the $H_n T_n$ and $\omega_n T_n$ used in Equations A17 and A19 of [27].

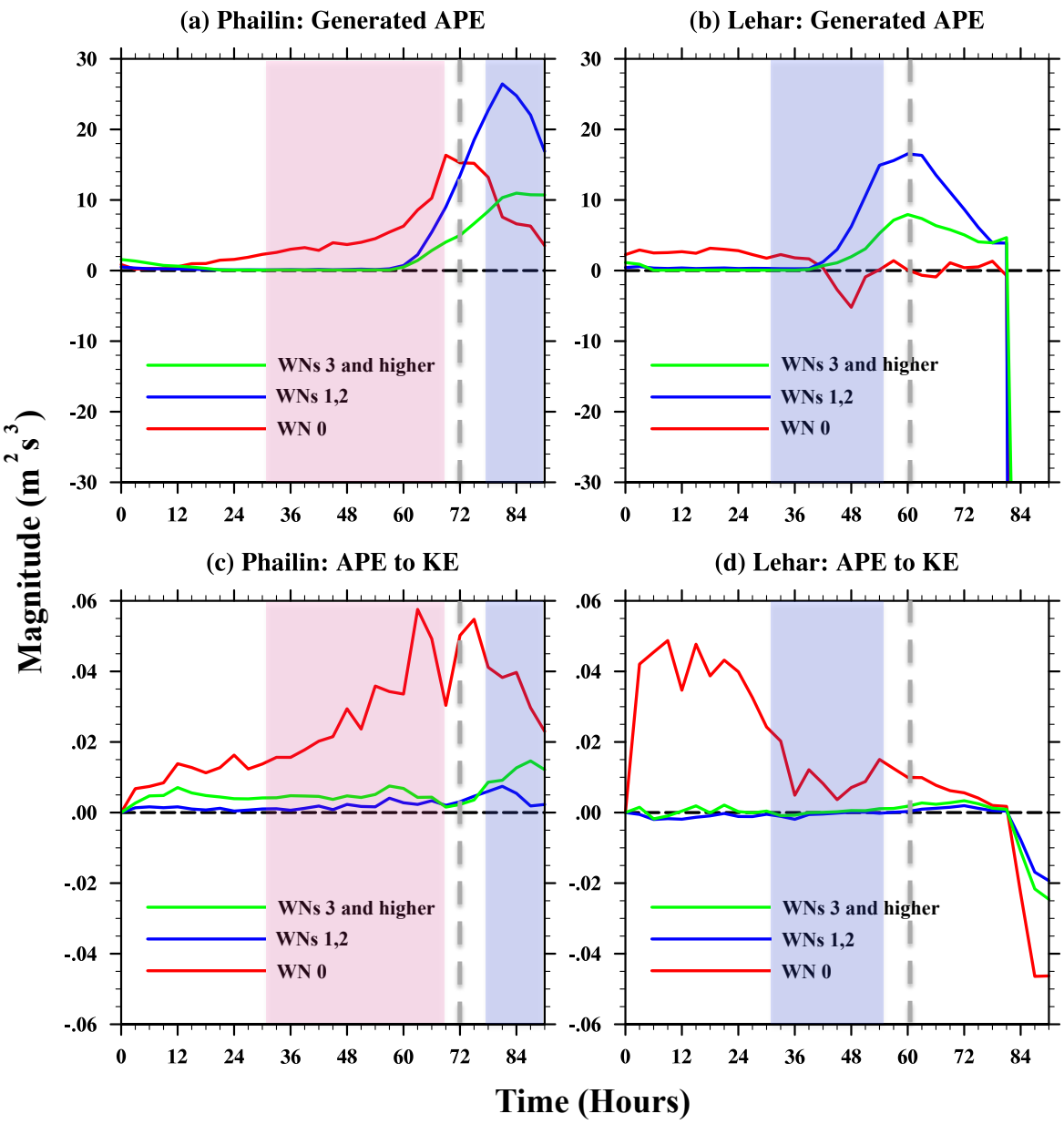

Figure 4.2. Time-series of the domain-averaged (up to a radius of 300 km, up to 20 km in the vertical) available potential energy (a,b) generated at axisymmetric mean (wavenumber 0), low order (wavenumber 1-2) and higher order wavenumbers (wavenumbers ¿2). (c,d) represents the conversion from available potential energy generated to kinetic energy. The left panels are for Phailin and the right panels are for Lehar. The RI period is shaded in red and the RW period is shaded in blue. The landfall time is marked by a dashed, gray line.

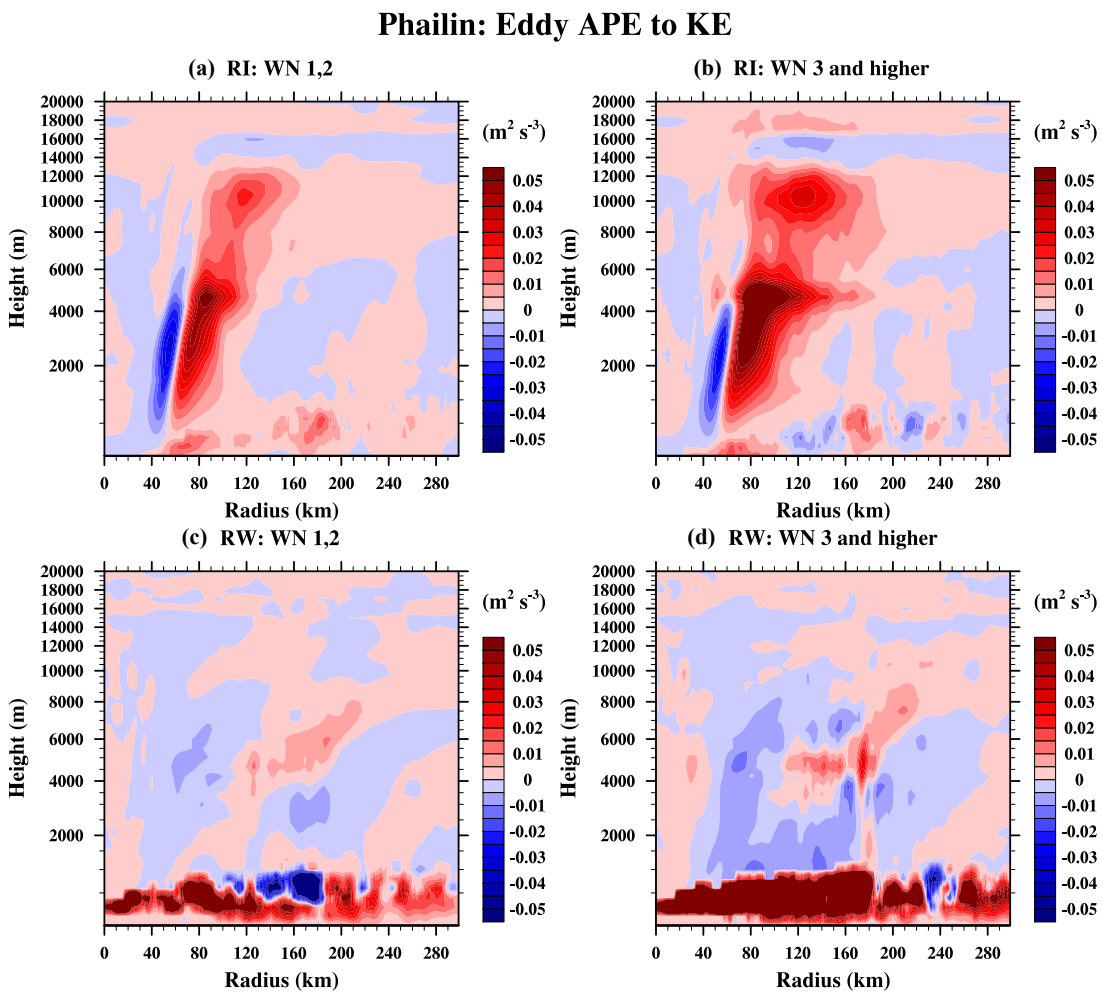

Figure 4.3. Phailin: Radius-height plots of the conversion from eddy potential to eddy kinetic energy for WNs 1,2 (a,c) and WNs 3 and higher (b,d). The RI and RW periods in Phailin correspond to the red shaded region in Figure 4.2c.

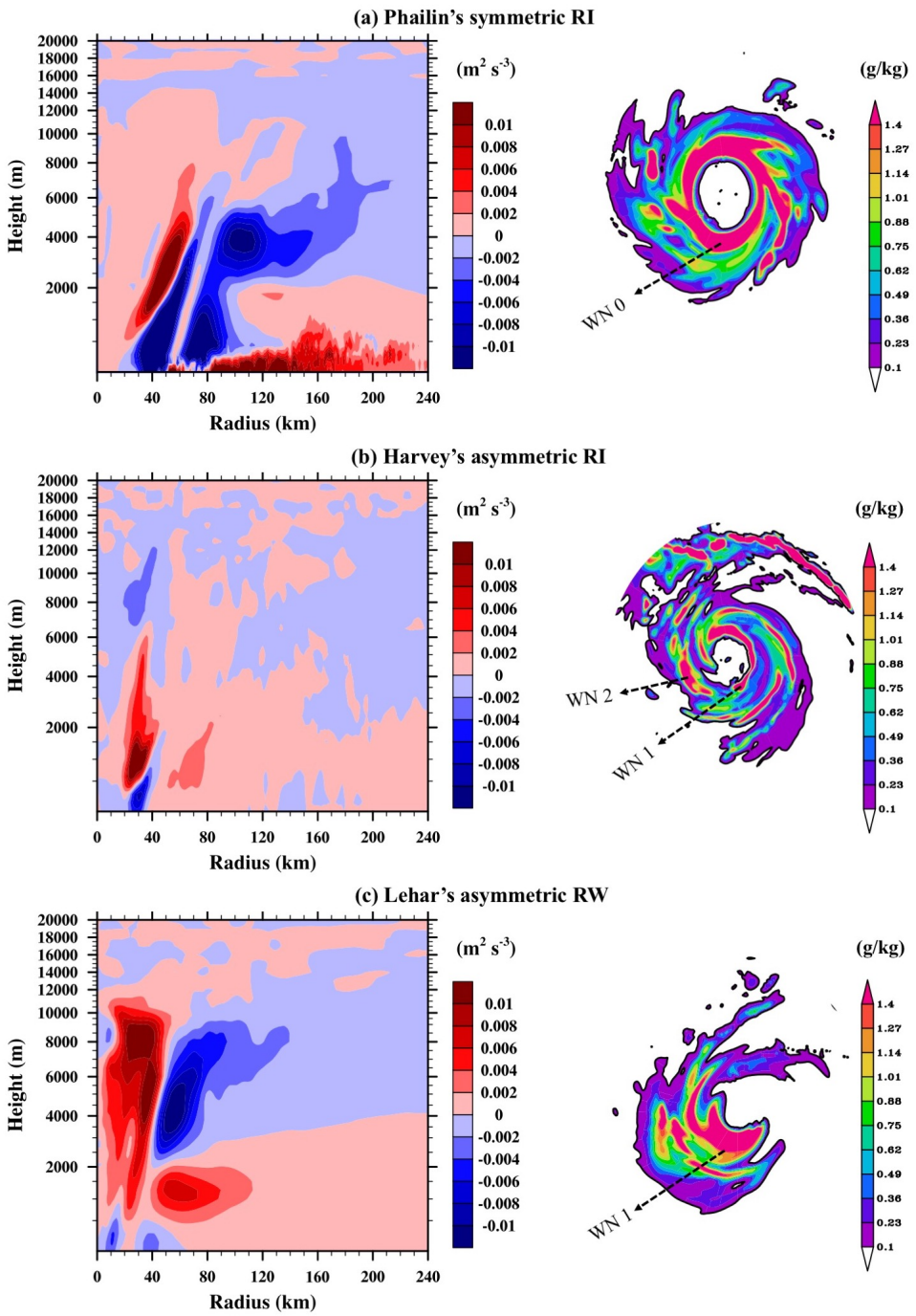

Figure 4.4. (Left) Radius-height plots of the barotropic exchange between the mean and low-wavenumber asymmetries for TC Phailin and Hurricane Harvey during their RI phases, and for TC Lehar during its RW phase. (Right) Corresponding plots of rainwater mixing ratio (in g/kg) to illustrate the symmetric or asymmetric nature of convection during the highlighted periods.

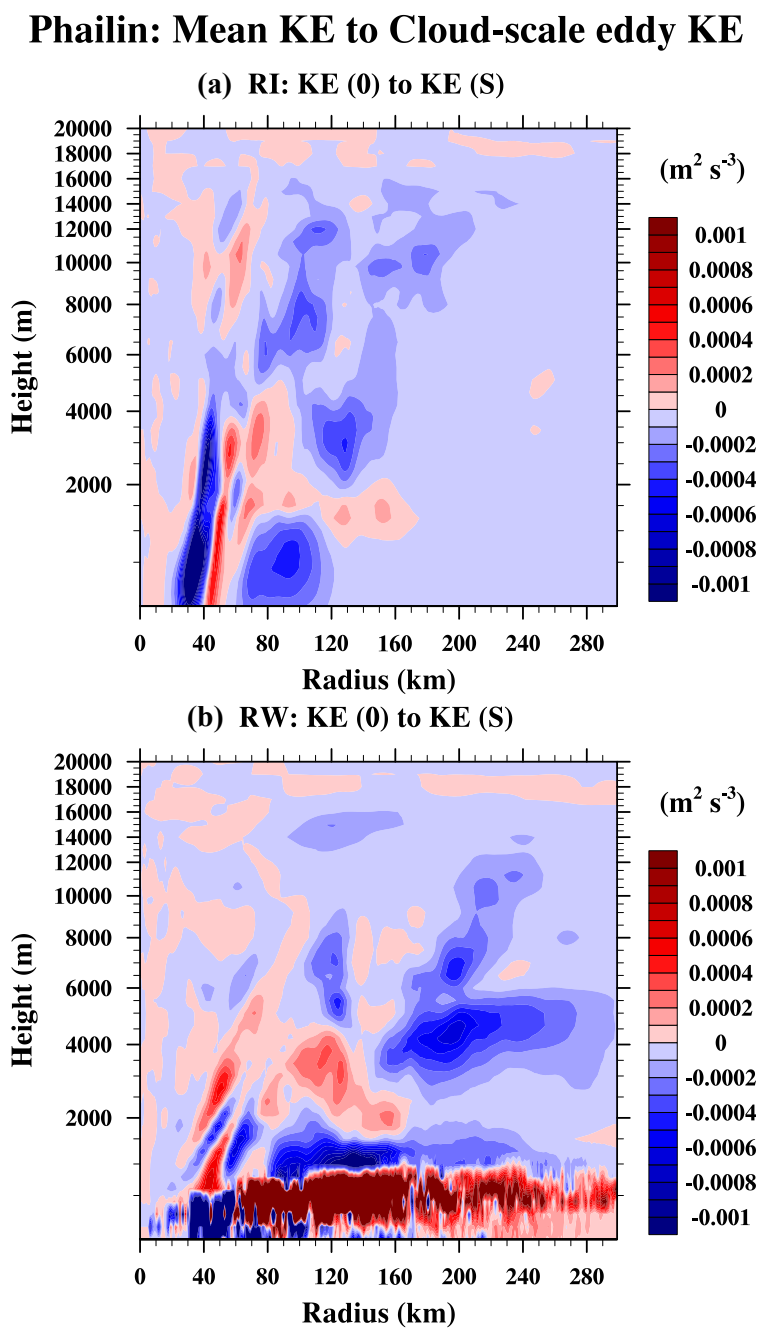

Figure 4.5. Radius-height plots of the barotropic exchange between the mean and short scales (WNs 3 and higher) for TC Phailin (2013) during its RI and RW phase.

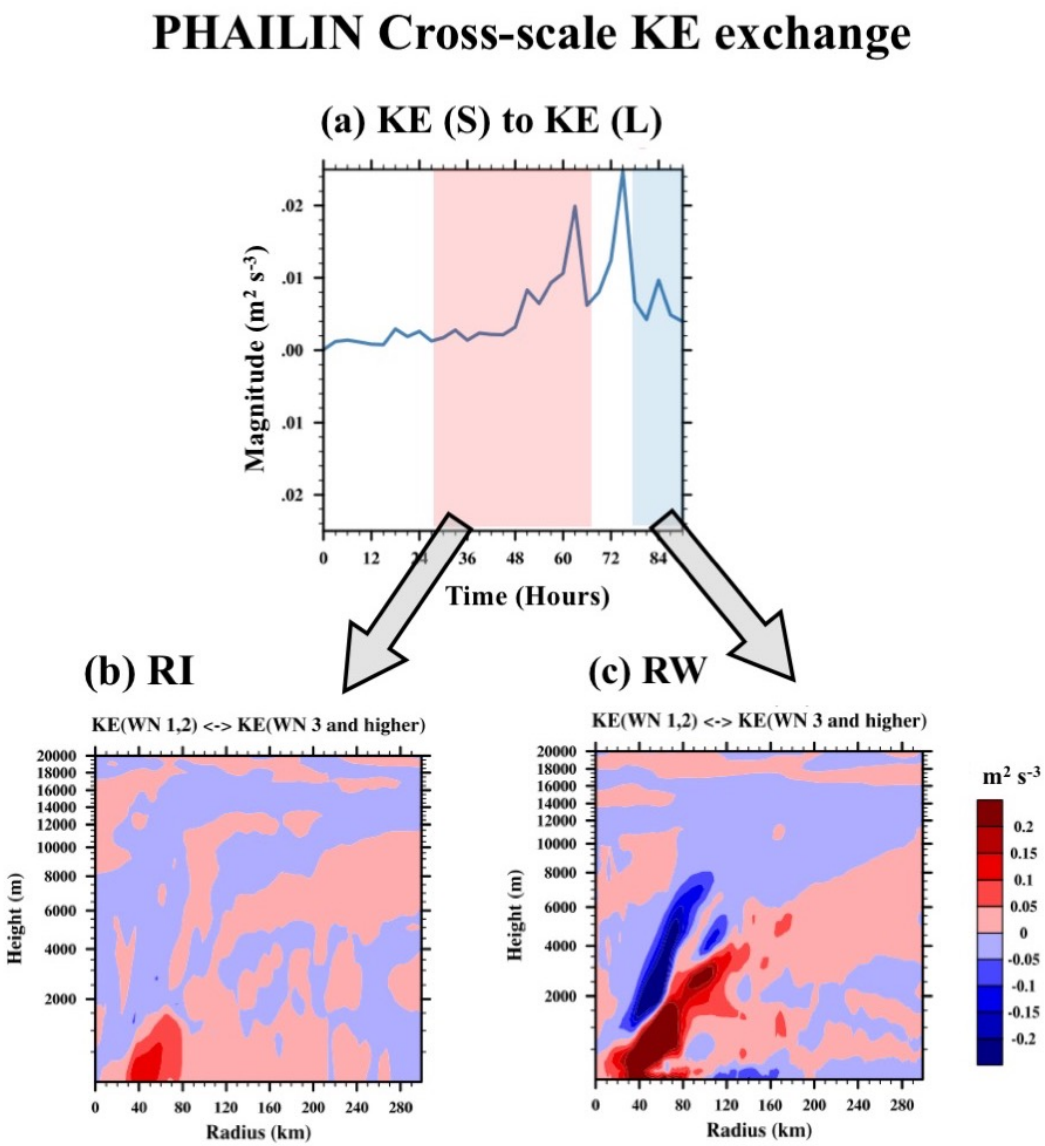

Figure 4.6. (a) Time-series plot of Phailin's (domain-averaged) rate of change of kinetic energy of long waves due to eddy-eddy interactions with the cloud scales. In this figure, an increase represents an upscale transfer of KE from short to long and a decrease represents a downscale transfer of KE from long to short. (b) and (c) Radius-height plots of the same quantity time-averaged during the Phailin's RI period (highlighted in red in (a)) and RW phase (highlighted in blue in (a)) respectively.

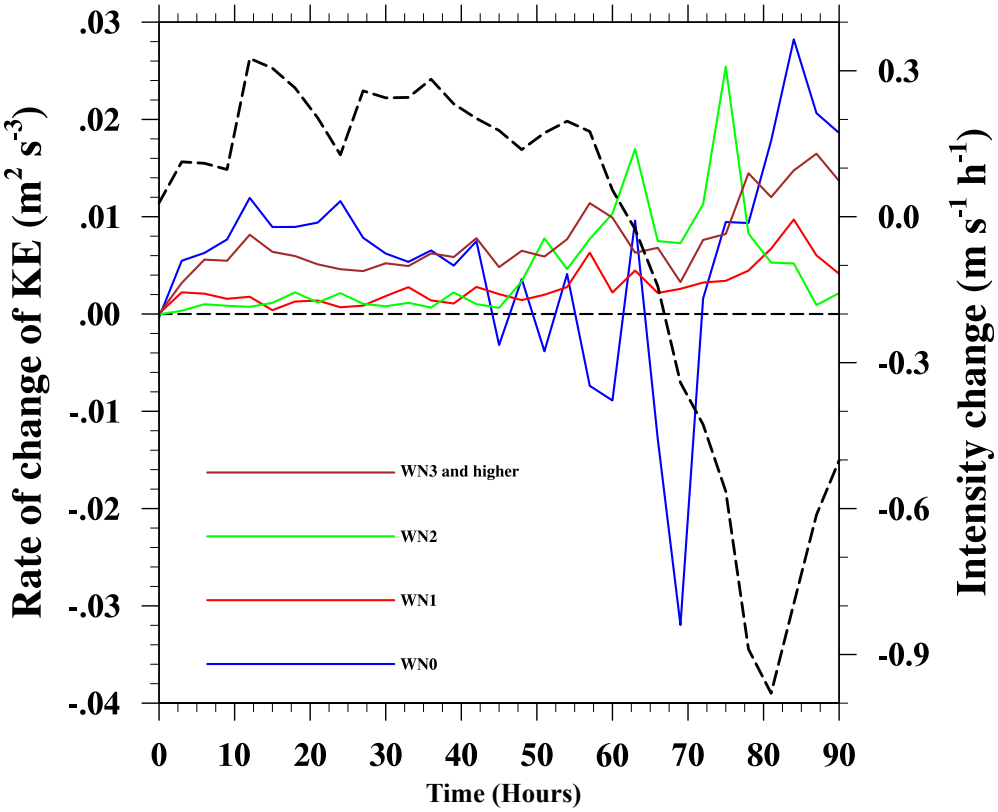

Figure 4.7. Time-series of the *net* change of KE in WNs 0,1,2,≥3 (blue, red, green and brown solid lines) in Phailin compared against the rate of change in intensity (black dashed line) over the course of its life-cycle. This figure serves to illustrate that due to the existence of multiple modes of energy exchanges that influence the KE at a particular scale, it is entirely possible that the energies at the mean and the eddies grow at the same time (t= 10 to 30 hours) or that the eddies grow at the expense of the mean (t = 65 to 75 hours).

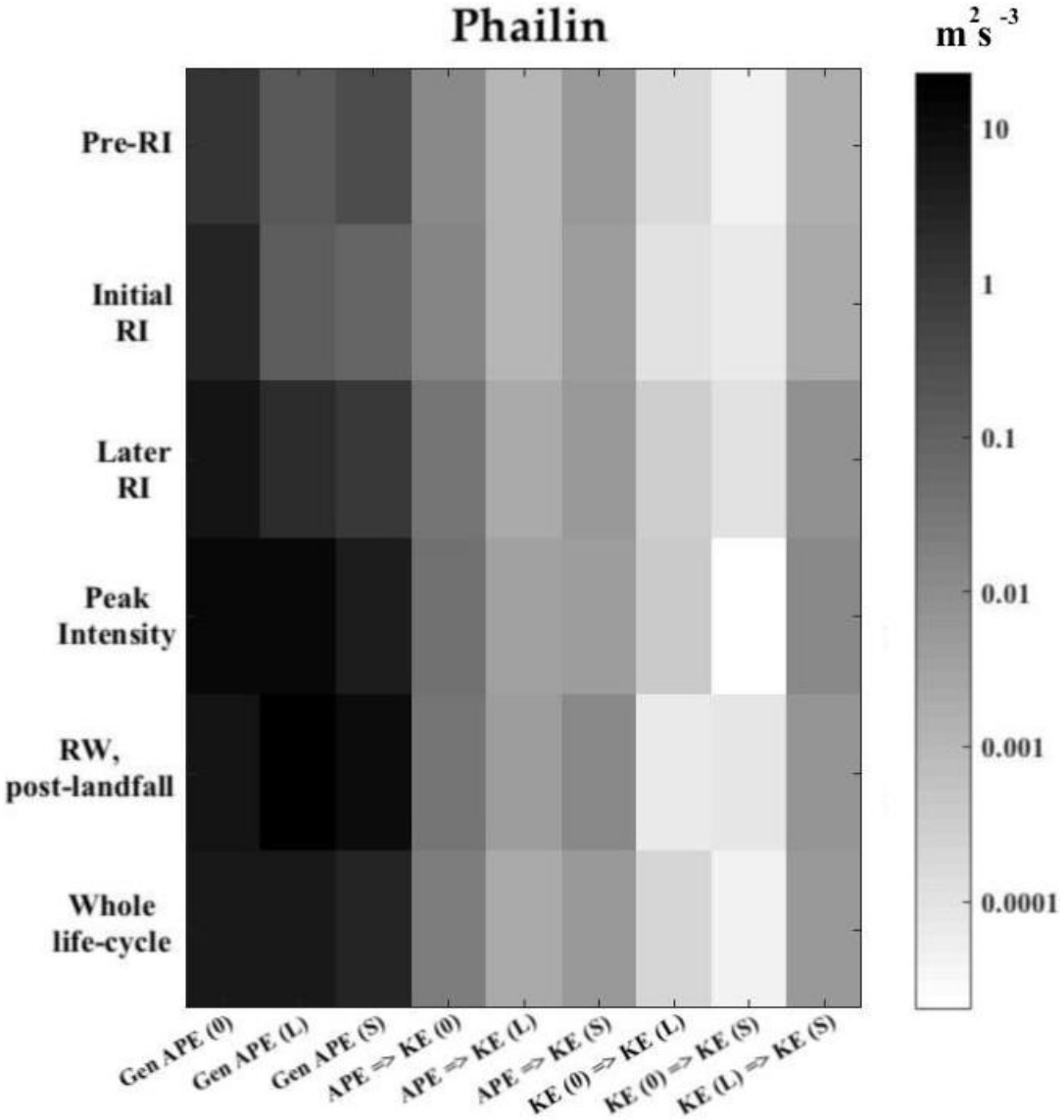

Figure 4.8. Order of magnitude analysis for the various energy transactions over the course of TC Phailin's life-cycle.

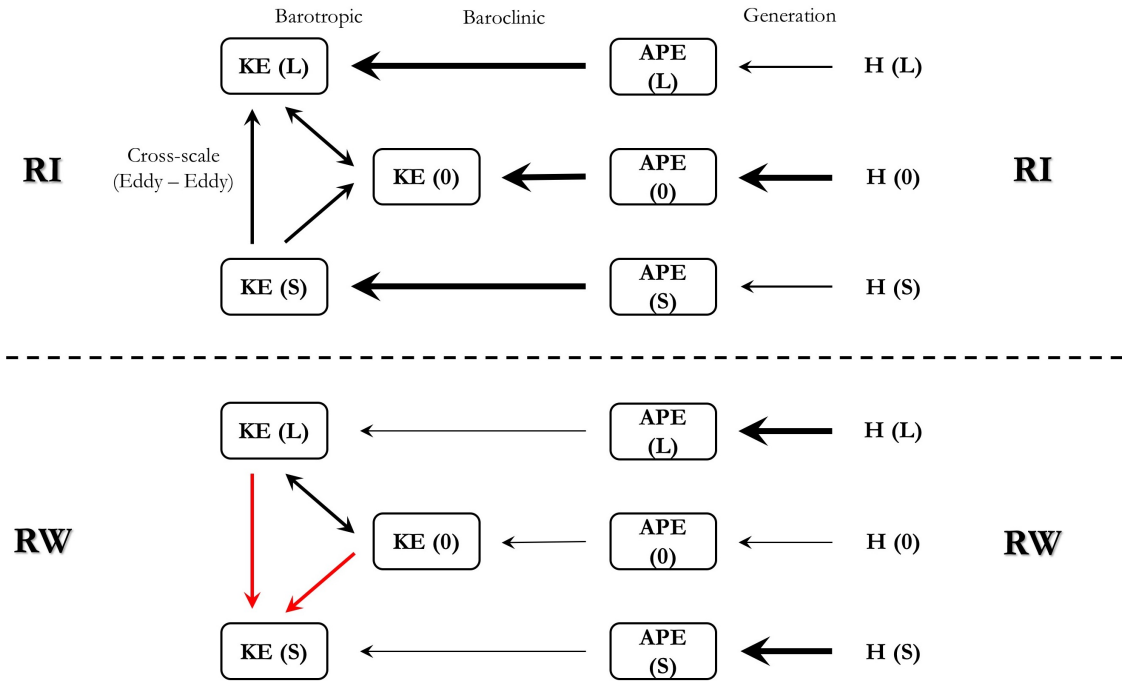

Figure 4.9. Summary of the insights from scale-interactions during RI and RW phases. In this figure, the weight of the arrow corresponds to the magnitude of the energy exchange and the change in color and direction represents a change in the direction of transfer of energy. Double-sided arrows indicate that the energy transaction can be either way during RI and RW.

5 PARSIMONIOUS DIAGNOSTIC MODELS

From a forecasting perspective, the vast amount of information available from models (e.g., HWRF has three spatial dimensions in three nested domains, and one temporal dimension) and observations makes it difficult for forecasters to analyze the potential for rapid intensity changes real-time. With this in mind, two further diagnostic frameworks - an empirical model and a stochastic model, are introduced in this chapter to aid in the probabilistic, real-time forecasting of TC rapid intensity changes.

5.1 Empirical model: Computation of the relative roles of factors influencing rapid intensity changes

(A version of this chapter has been published in Geophysical Research Letters)

In this section, I present an empirical framework that examines symmetric and asymmetric convection and other state variables within the vortex, and in the environment across a suite of TC and identifies a set of 'important' variables that are significantly different during time periods that precede a rapid intensification as opposed to a rapid weakening. Our framework then ranks the variables identified based on how significantly they influence a rapid intensity change in a TC and the amplification factor of any associated variability. The highest ranked variables are the ones that must be prioritized in future observational and consequent modeling efforts that incorporate such observations as initial conditions of TC forecast models.

5.1.1 Background

The roles of external, large-scale environmental processes towards influencing RICs are better understood due to the longer timescales associated with the processes of

interest [36, 46, 109–114]. Therefore, statistical indices targeted at RI prediction were developed primarily using large-scale environmental predictors [46, 115, 116]. While there are no corresponding indices for RW over the ocean, empirical indices for rapid decay of TC intensity *post-landfall* have been developed [117]. However, such indices have their limitations [44]. Hendricks et al. (2010) cautioned that RI is mostly controlled by *internal dynamical processes* and therefore, may not be well predicted by models that under-represent such processes. The processes intrinsic to a TC vortex occur at a multitude of spatial and temporal scales and many of the stochastic processes may not be persistent enough to influence a systemic change within the vortex. An inclusion of all such processes may or may not offer any advantage in our ability to predict a critical transition at a vortex-scale. Therefore, it is critical that we identify and include the processes at those scales that have the most persistent and significant impact at a vortex-scale. Section 4 dealt with how the processes at individual cloud scales impact the processes at the vortex-scale.

In this light, only recently has the role of processes within the inner-core of the vortex received sufficient attention from observational [61, 118–120] and numerical [12,32,33,71,121] efforts. The focus of these studies has largely been on the spatial (radial and azimuthal) distributions of symmetric and asymmetric convection. Their conclusions point to two distinct convective pathways that lead to RI: through asymmetric (isolated) bursts of intense convection or via well-organized, symmetric, albeit weaker convection. Here, we take a holistic and objective perspective and address the relative importance of symmetric and asymmetric convective processes in causing RI or RW. Additionally, Rogers et al. (2013) [120] noted that an important aspect that separated TCs that underwent RI from steady-state ones was the *radial* location of convection with respect to the radius of maximum winds (RMW). They found that during RI, the convection was located *inside* the RMW and during other times, the convection was concentrated *outside* the RMW. Alternatively, other studies [33,66,71] focus on the *azimuthal* distribution of convection with respect to the shear vector. However, these results are largely based on individual cases or idealized experiments,

with very few systematic studies (such as [65]) conducted over a large number of cases that are sufficiently varied and representative to make statistically significant conclusions.

The present study aims to incorporate the insights from the above-mentioned studies and address the following specific scientific questions by analyzing a suite of TCs that experienced RICs: What is the relative importance of the following: 1. processes occurring at the vortex-scale versus those occurring in the TC environment 2. the spatial distribution of inner-core convection. Specifically, (a) the symmetric distribution versus asymmetric distribution of convection; and (b) the radial distribution with respect to RMW versus the azimuthal distribution with respect to the shear vector.

It is important to note that any computation of the relative roles is useful only when you look at the behavior of a variable *in the context* of the other variables. For example, instead of questioning how important vortex-scale convective processes are for RIC, we seek to understand the importance of vortex-scale process in the context of multiple environmental backgrounds. To achieve our objectives, our empirical approach analyzes model simulations of recent TCs over the Bay of Bengal that underwent RICs.

In addition to the complexity of the multiple processes interacting nonlinearly and acting simultaneously, there are uncertainties in the representations of these processes and in the initial conditions provided to our forecast models [122, 123]. The uncertainty in the knowledge of the initial values combined with the inherent stochasticity of processes we seek to simulate makes it unwise to rely solely on deterministic predictions [114, 124]. With this in mind, we choose to focus on how the joint probability density functions (PDFs) of the initial values that evolve to rapidly intensify are different from those that evolve to rapidly weaken, and what specifically about these initial values is different for the two populations. Kaplan et al. (2010) [115] caution that the relative significance of various processes influencing a TC's intensity change may vary from basin to basin. From that perspective, the results and the

subsequent interpretations presented here are directly linked to the basin of interest and the assumptions made in the model. However, our primary intent is to present a generic framework that allows for the quantification of the relative significance of the competing processes in a TC. We also seek to identify the 'generic markers' or instantaneously measurable symptoms that indicate whether a TC is about to undergo RI or RW. Finally, we address how the variability of these markers affects the 24-hour change in the TC intensity.

5.1.2 Data

TCs over the Bay of Bengal basin that experienced a rapid intensity change at least once over their life-cycles between 2012-2017 are selected (Table 5.1). The Weather Research and Forecasting model (WRF, version 3.4.1) is used to simulate the above-mentioned TCs of interest and the details of the model configurations are available in Table 5.4. These simulation use nested grids in which the grid-spacing of the inner domain is 4km and one-hourly outputs are recorded. The simulations are then transformed to a storm-centric, cylindrical coordinate system where the center is defined as the minimum surface pressure centroid for each time. As an example, the time-series of TC Phailin's and TC Lehar's intensities (maximum 10-m tangential wind in m/s) are shown in Figure 5.1a. Of interest here are the times just preceding a rapid intensity change (highlighted periods in Figure 5.1a). The TCs are not further classified based on their intensity, magnitude of shear, or proximity from land at the time of consideration. A total of 319 cases (158 RI and 151 RW) are obtained from these storms.

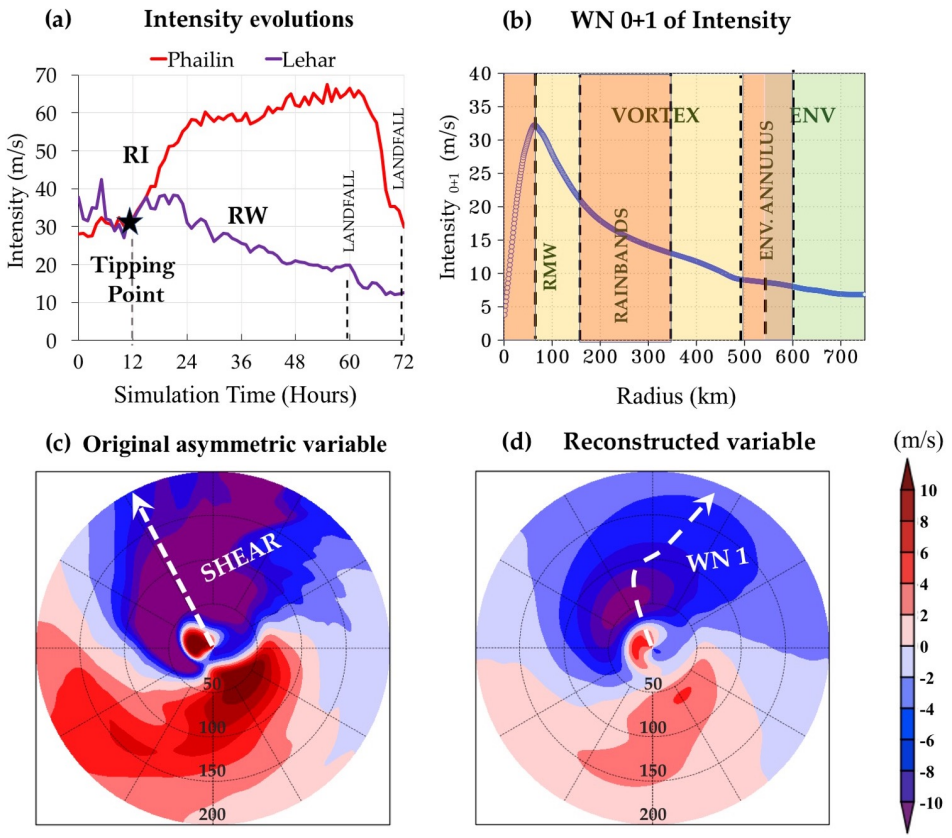

Figure 5.1. (a) Time series of intensity (maximum 10-meter tangential winds) for TCs Phailin and Lehar forecast by the model. The rapid intensification phase of Phailin and the rapid weakening phase of Lehar are denoted as 'RI' and 'RW' respectively. (b) Low wavenumber reconstruction of TC Phailin's intensity at t=12 (before the start of RI) used to identify the RMW, the rainband region, the bounds of the vortex, and the environmental annulus. (c) The horizontal cross-section of Phailin's radial wind averaged between the surface and 850 mb represented in storm-centric, cylindrical coordinates. (d) Same as (c) except that the asymmetric variable is reduced to its lowest wavenumbers. The shear vector and the phase vector of WN 1 are highlighted.

Table 5.1.

The selected list of tropical cyclones (TCs) over the Bay of Bengal. Also, the dates and times of initialization (cycles) of the TCs in the numerical model are provided. The length of each simulation was 72 hours. A 'case' constitutes a set of vortex and environmental state variables extracted from model outputs at an instance in time (say, t = t1) that precedes a rapid intensity change in the next 24 hours (From t1 to t1 + 24). In other words, for a 72-hour simulation, the intensity change between t1 + 24 and t1 is computed as t1 varies from the first hour to the 48th hour. If the magnitude of intensity change between t1 + 24 and t1 is greater than 30 knots, the case is selected for diagnosis. Thus, within the 33 simulations, there are 48 possibilities (33x48=1584 total possibilities) for a rapid intensity change. While we understand that there may be some overlap between the cases taken within a single TC for times that are close, each case still represents a unique combination of the state variables within the vortex and in the environment.

Tropical Cyclone	Initialization dates and times
Nilam	0 UTC, 28th October 2012; 0 UTC, 29th October 2012; 0 UTC, 30th October 2012.
Viyaru	0 UTC, 12th May 2013; 0 UTC, 13th May 2013; 0 UTC, 14th May 2013;
Phailin	0 UTC, 9th October 2013; 0 UTC, 10th October 2013; 0 UTC, 11th October 2013;
Helen	0 UTC, 20th November 2013; 0 UTC, 21st November 2013; 0 UTC, 22nd November 2013;
Lehar	0 UTC, 26th November 2013; 0 UTC, 27th November 2013; 0 UTC, 28th November 2013;
Madi	0 UTC, 12th December 2013; 0 UTC, 13th December 2013; 0 UTC, 14th December 2013;
Hudhud	0 UTC, 9th October 2014; 0 UTC, 10th October 2014; 0 UTC, 11th October 2014;
Roanu	0 UTC, 18th May 2016; 0 UTC, 19th May 2016; 0 UTC, 20th May 2016;
Kyant	0 UTC, 23rd October 2016; 0 UTC, 24th October 2016; 0 UTC, 25th October 2016;
Nada	0 UTC, 29th November 2016; 0 UTC, 30th November 2016; 0 UTC, 1st December 2016;
Vardah	0 UTC, 11th December 2016; 0 UTC, 12th December 2016; 0 UTC, 13th December 2016;

Table 5.2.
Details of the Weather Research and Forecasting model set-up.

Model used	WRF-ARW v3.4.1
Resolution	Two-way Nested domain with 12 km and 4 km grid-spacing (36 vertical levels)
Initialization	NCEP GFS 0.5deg data
Forecast Updates	Daily with 00Z initial condition
Forecast Period	72 hours with hourly interval
Domain size	7.12196 N to 37.3972 N; 63.9995 E to 97.609 E
Cumulus Physics	Kain-Fritsch Scheme (only on the 12km domain; turned off for the 4km domain)
Microphysics	Thompson
Long wave radiation scheme	Rapid Radiative transfer model - G
Short wave radiation scheme	Rapid Radiative transfer model - G
Surface layer physics	Eta similarity scheme
Land surface scheme	Unified NOAH
Boundary layer physics	Yonsei University Scheme

5.1.3 Low Wavenumber Reconstruction

The following variables and combinations thereof from the WRF model outputs are initially selected to describe the instantaneous state of the vortex and the environment just before a RIC:

- Precipitation
- Radial and vertical component of wind
- Divergence of horizontal wind

- Relative humidity
- Environmental wind shear
- Horizontal moisture flux convergence

Note that this itself would amount to some 10^9 atmospheric state variables in the radial, azimuthal, and vertical dimensions over the domain. To reduce the dimensionality, these variables are first reduced to their wavenumbers (WN) 0 and 1 azimuthal harmonics (the lowest-order symmetric component, WN 0 and the lowest-order asymmetric component, WN 1) similar to the treatment in [125] using the following equations:

$$f(r,\theta) \approx \hat{f}_0(r) + \hat{a}_1(r)cos(\theta) + \hat{b}_1(r)sin(\theta) \tag{5.1}$$

$$where \quad \hat{f}_0(r) = \frac{1}{2\pi}\int_{-\pi}^{\pi} f(r,\theta)d\theta, \tag{5.2}$$

$$\hat{a}_1(r) = \frac{1}{2\pi}\int_{-\pi}^{\pi} f(r,\theta)cos(\theta)d\theta, \tag{5.3}$$

$$\hat{b}_1(r) = \frac{1}{2\pi}\int_{-\pi}^{\pi} f(r,\theta)sin(\theta)d\theta \tag{5.4}$$

where $f(r,\theta)$ represents any 2D variable in a storm-centric, cylindrical coordinate framework; r and θ are the independent variables: radius and azimuthal angle respectively; The hats indicate an azimuthal Fourier harmonic and the subscript indicates which harmonic.

The low wavenumber reconstruction (WN 0+1) of 10m tangential winds (intensity) of the individual cases was used to identify the radii corresponding to the maximum winds (RMW), the outer boundary of the vortex, and the environmental annulus as highlighted in Figure 5.1b. An example of how an original asymmetric variable (low-level radial wind) is reduced to its low wavenumber counterpart is depicted in Figures 5.1 c,d. Also highlighted are the shear (defined as the vector difference between 200 mb and 850 mb averaged winds) vector in the original asymmetric variable and the WN 1 phase vector in the reconstructed variable. the outer boundary of the vortex is defined as the radius at which the WN 0+1 of intensity drops below 8

m/s. The environmental annulus is then defined as the annulus ± 50 km from the radius that marks the outer boundary of the vortex. Additionally, the radii between the 2*RMW and 5*RMW is denoted as the rainband region. Once these regions are defined for each case, the wavenumber 0 and 1 coefficients of the variables listed above were obtained and then averaged over a handful of horizontal sectors (the disk within the RMW, the rainband annulus, and the environmental annulus) and four vertical layers (between 1000 - 850 mb, 850 - 700 mb, 700 - 500 mb, and 350 - 200 mb). The subset of 26 variables listed in Table 5.3 was retained as the candidate variables whose relative importance in determining the 24-hour intensity change will be quantified.

Previous studies [36] have also shown that over the Bay of Bengal, the sea surface temperature (SST) while one of the 'necessary' conditions for TCs to persist, is not very useful in differentiating those TCs that rapidly intensified or weakened. Therefore, only atmospheric state variables are considered for the current study that focuses on the Bay of Bengal basin. A similar effort over the Atlantic Ocean for example, will require the consideration of SSTs and ocean heat content since they have anecdotally and statistically been observed to be important [115]

We emphasize that this list was designed with a sole purpose to directly address the questions pertaining to the relative importance listed in Section 5.2.1. As a result, this list of variables does not resemble the set of variables used previously to develop statistical RI indices [36, 46, 115][1].

The assumption made here is that WN 1 represents most of the variance contained in the asymmetries (Figure 5.2). Since the treatment of our problem of interest is that of an initial value problem, only the initial state at the beginning of the

[1]One of our initial objectives was to understand the relative importance of variables and processes in different azimuthal quadrants defined with respect to environmental shear vector (Upshear left, Upshear right, Downshear left, and Downshear right). For this purpose, once the variables were reconstructed to their lowest wavenumbers, they were azimuthally averaged in the different shear-based quadrants. However, for the dataset considered here, the covariance between the variables in the different quadrants was very high. Furthermore, the shear vector was not always a good representative of the variance in WN 1. For this purpose, we refrained from using variables from different quadrants defined with respect to the shear vector. We note that our approach might have to be different if the initial set of TCs comprised only of those that experienced moderate to high shear and further examination is necessary.

Table 5.3.

List of variables after low wavenumber reconstruction. Notes: (i) The precipitation variable used here is a 2D variable (integral quantities for each grid cell). (ii) While the WN 0 represents the azimuthal average of a variable, the asymmetric representation of variables indicated as WN 0+1 are averaged in an azimuthal quadrant centered around the phase vector pointing towards the maximum or minimum WN1 asymmetry. (iii) The variables are either averaged within the radius of maximum wind (RMW), in the rain band region, within the entire vortex, or in the environmental annulus.

1	WN0 of Divergence of the wind at 200-300 hPa in the environmental annulus
2	WN0 of rain at the environmental annulus
3	WN0 of rain within the RMW
4	WN0 of rain in the rain band region
5	WN0 of environmental relative humidity at 850-700 hPa
6	WN0 of environmental relative humidity at 1000-850 hPa
7	WN0+1 environmental relative humidity at 850-700 hPa - Averaged in a quadrant around the max asymmetry
8	WN0+1 environmental relative humidity at 1000-850 hPa - Averaged in a quadrant around the max asymmetry
9	WN0+1 environmental relative humidity at 850-700 hPa - Averaged in a quadrant around the min asymmetry
10	WN0+1 environmental relative humidity at 1000-850 hPa - Averaged in a quadrant around the min asymmetry
11	Angle of the phase vector of driest environmental air (WN 1, 700 – 400 mb) and the shear vector
12	WN0 of the 1000-850 hPa horizontal moisture flux convergence within the RMW
13	WN1 of the 1000-850 hPa horizontal moisture flux convergence within the RMW
14	WN0 of the 850-700 hPa horizontal moisture flux convergence in the rain band region
15	WN1 of the 850-700 hPa horizontal moisture flux convergence in the rain band region
16	WN0 of the 1000-850 hPa radial wind within RMW
17	WN0+1 of the 1000-850 hPa radial wind within the RMW - Averaged in a quadrant around maximum inflow asymmetry
18	WN0 of the 850-700 hPa radial wind within the RMW
19	Magnitude of environmental (deep-layer) shear (difference between 850 and 200 hPa)
20	Convective bursts (Number of grid cells with vertical velocity greater than 1m/s at 8km (350 hPa)) within RMW
21	Phase overlap between boundary layer inflow, maximum of relative humidity, and upward vertical velocity within the vortex
22	Phase overlap between boundary layer inflow, minimum of relative humidity, and downward vertical velocity within the vortex
23	Magnitude of WN1 of rain within the RMW
24	Magnitude of WN1 of rain in the rain bands
25	Angle of the phase vector of WN1 of rain within RMW and the shear vector
26	Angle of the phase vector of WN1 of rain in the rain bands and the shear vector

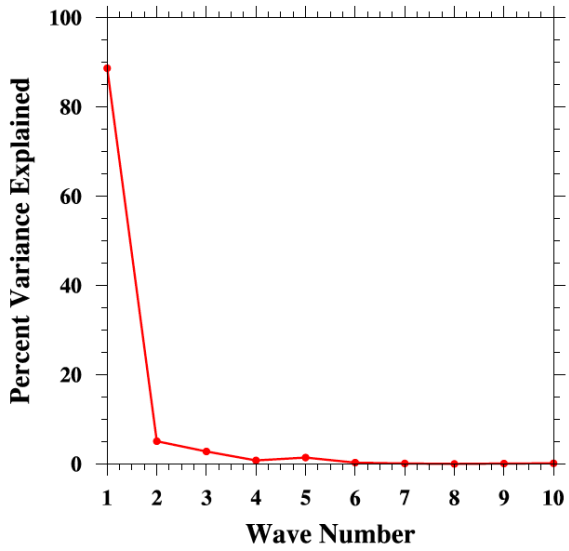

Figure 5.2. The percentage of variance in 10m tangential velocity (intensity) explained by azimuthal harmonics (wavenumbers) 1 to 10 for TC Lehar (2013) just before the start of its rapid weakening (t = 24, initialization: 2013112600). The computation is performed within a 3 x3 degree box around the center of circulation. This figure serves to illustrate that the majority of the eddy (wavenumbers greater than 0) variance is contained in wavenumber 1 and hence, the low wavenumber reconstruction is justified. Under rare scenarios, the percent of variance explained by the higher wavenumbers is much larger. Nonetheless, the idea is to simplify the complex asymmetric field into one symmetric (WN 0) and one asymmetric (WN 1) component.

RIC period (and the boundary conditions) has any effect on the simulated TCs. From that perspective, all the effect from the higher order wavenumbers (WNs 2 and higher) from previous times is already contained in the initial state. Such upscale and downscale exchanges between eddies of different wavenumbers are detailed in Section 4. However, even if the higher order wavenumbers are important to the evolution of the storm, WN 1 represents the organized asymmetries that are the most persistent in time and therefore have the best predictive potential [125].

5.1.4 Computation of Linear Discriminants and Projection on to Principal Component space

Given that we characterize an initial TC state with a small discrete set of variables $x_1, x_2 \cdot x_n$, the problem of separating points that were characterized as RI from points that are characterized as RW becomes one of finding a hyperplane that separates the two sets of points in n-dimensional space. For two such objectively separated populations (RI and RW) with means $\vec{\mu_{RI}}$ and $\vec{\mu_{RW}}$, and with covariances C_{RI} and C_{RW}, the separation threshold (S) between the two distributions is defined as the ratio of the variances between the two populations to the variance within the populations [126]. The Fisher's linear discriminant is given by:

$$[(C_{RI}+C_{RW})^{-1}(\vec{\mu_{RI}}-\vec{\mu_{RW}})^t)]\ \vec{x} \gtrless [(C_{RI}+C_{RW})^{-1}(\vec{\mu_{RI}}-\vec{\mu_{RW}})^t)]\frac{(\vec{\mu_{RI}}+\vec{\mu_{RW}})}{2} \quad (5.5)$$

By denoting $[(C_{RI} + C_{RW})^{-1}(\vec{\mu_{RI}} - \vec{\mu_{RW}}))]^t$ as α and the right hand side as the threshold (S), this equation may be further written as

$$\alpha_1\vec{x}_1 + \alpha_2\vec{x}_2 + \cdots + \alpha_n\vec{x}_n \gtrless S \quad (5.6)$$

If the discriminant produced is $>$ than S, this means that $\vec{x}$ leads to RI and if the discriminant produced is $<$ than S, it means that $\vec{x}$ leads to RW.

After normalizing the variables $\vec{x_i}$ by their respective variances, σ_i, eqn. 6 may be rewritten as:

$$\alpha_1\sigma_1(\frac{\vec{x}_1}{\sigma_1}) + \alpha_2\sigma_2(\frac{\vec{x}_2}{\sigma_2}) + \cdots + \alpha_n\sigma_n(\frac{\vec{x}_n}{\sigma_n}) \gtrless S \quad (5.7)$$

Consequently, $\alpha_1\sigma_1 \cdots \alpha_n\sigma_n$ are the coefficients (weights) associated with each of the normalized variables that may be compared. Note that the modeled cases are segmented into RI and RW a priori and that the variables associated with the biggest normalized weights in the linear discriminant analysis (LDA) are the most significant in causing the separation between the two populations.

Initially, no assumption is made about the relative importance of variables and the entire list in Table 5.3 is subject to the LDA. The 319 cases are randomly split

into one training and one testing subset following a 50:50 ratio and the discriminant is computed. This exercise is repeated a thousand times whilst varying the training and testing data subsets. This randomization produces a thousand discriminants for a thousand sub-samples. To decide whether the randomization of the training dataset essentially produces the same discriminant for each of the 1000 randomizations, or if instead it produces different discriminants which are highly dependent on the training set, the coefficients of the LDA resulting from each of the 1000 iterations are projected onto their top two Principal Components (PC). PC1 and PC2 capture most of the variability of these coefficients and, therefore, enable a two-dimensional quantification of their variability as the training set is randomized (Figure 5.3a). Note how the variance is extremely high (order of magnitudes 10^6 and 10^7).

Using the initial variable list, the LDA produced significantly different discriminants when the training data subsets were randomly varied. This is a clear evidence of over-fitting. To rectify this, a novel technique was used wherein we analyzed the coefficients of the discriminants for the cases that projected on the *extreme* ends in PC space i.e. around the edges of the ellipsoid capturing most of the points in PC1-PC2 space. By comparing the coefficients of the initial variable list for these cases, it was possible to identify the variables whose coefficients were consistent across different training sets and those whose coefficients exhibited a large variability, often changing signs while keeping relatively large magnitudes[2]. An example of this is provided in Figures 5.5 and 5.6.

The PC analysis revealed a core subset of variables whose coefficients were essentially constant regardless of the randomized training set used. These variables are listed in Figure 5.7a and Table 5.4. The 1000 discriminants were re-derived using this core subset, for each of the 1000 randomized training sets. In this manner, we allowed the LDA to guide the set of variables to be used for analysis without making

[2]The exact reason for such inconsistent behavior is not known at this point. One possible explanation could be that since the LDA assumes that the two populations are separable by their means, if a particular variable has identical means but very high variances, skewness, or kurtosis, between the two populations, then the assumptions of the LDA fails at this point.

a subjective assumption regarding the relative importance of these variables. In the following section, only the LDA of the core subset of variables is presented. These 1000 discriminants were then averaged, producing a single 'mean' discriminant. The details on the selection of the optimal threshold (S) for the mean discriminant are provided in Figure 5.8.

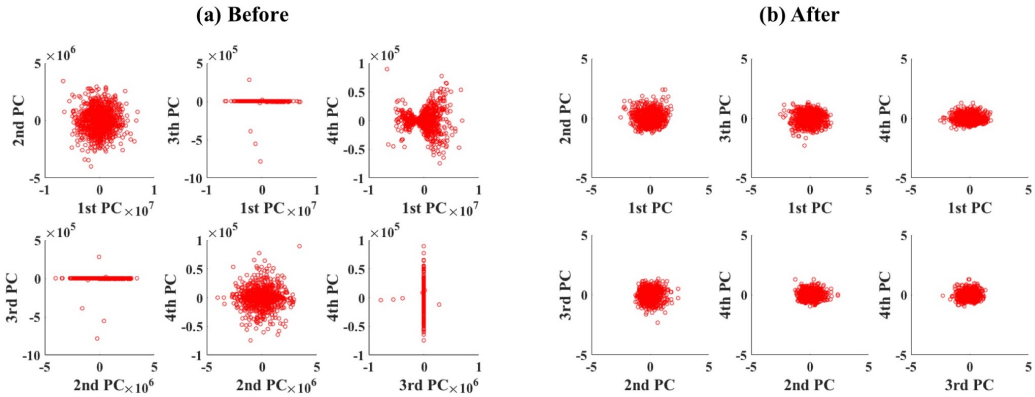

Figure 5.3. (a) Coefficients of the linear discriminant analysis (LDA) performed iteratively using a 1000 different training sets chosen from the superset of cases and the *initial* variable list projected on to principal component space. (b) Same as (a) but using only the consistent variables (after the removal of outliers).

5.1.5 Results of the Discriminant Analysis

Figure 5.4 presents the results of the LDA using only vortex-scale variables (Figure 5.4a), only the environmental variables (Figure 5.4b), and when all the variables are considered together (Figure 5.4c). The y-axis represents the magnitude of discriminant computed using the left-hand side of Eqn. 5.7. The cases that underwent RI in reality, are represented as blue and those that underwent RW in reality, are represented as red in Figure 5.4. Here, a discriminant higher than the threshold (S) implies that the specific case is estimated by the LDA to undergo RI and a discriminant less than S implies that the case is estimated by the LDA to undergo RW. Thus,

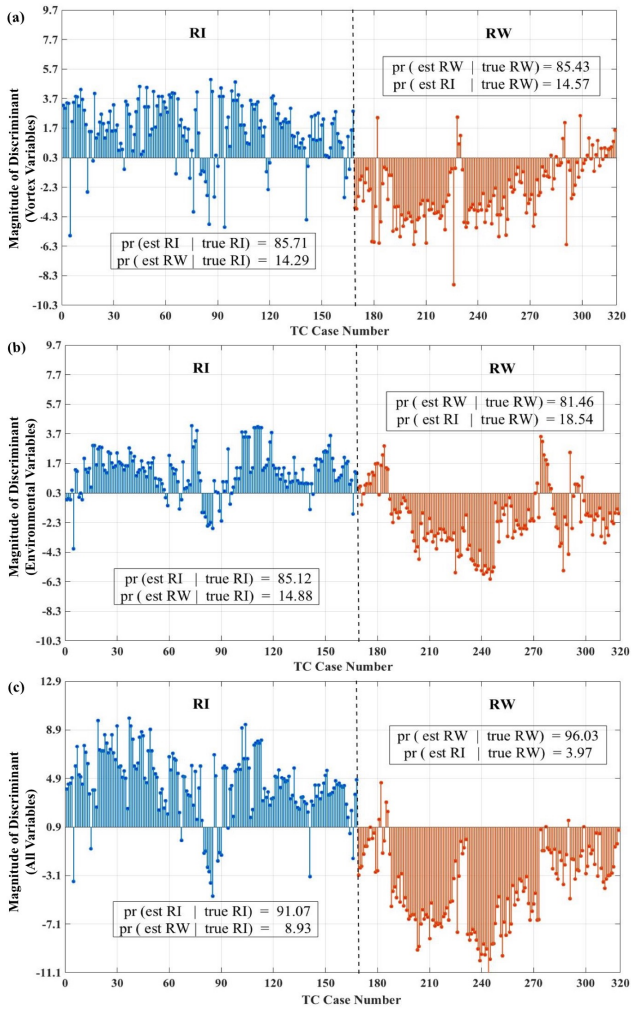

Figure 5.4. Results of the linear discriminant analysis. (a) Magnitude of discriminants computed for the RI and RW cases using only the vortex variables (b) Same as (a) except that the computation is done only using the environmental variables (c) Same as (a) except that the computation is done using both vortex and environmental variables together. The threshold (S) is marked by a horizontal line. Also highlighted are the estimated and true probabilities.

the true positives (pr (estimated RI | true RI) in Figure 5.4) and true negatives (pr (estimated RW | true RW) in figure 5.4) are indicated by blue lines with discriminants over S and red lines with discriminants less than S respectively. Likewise, the false positives (pr (estimated RW | true RI) in figure 5.4) and false negatives (pr (estimated

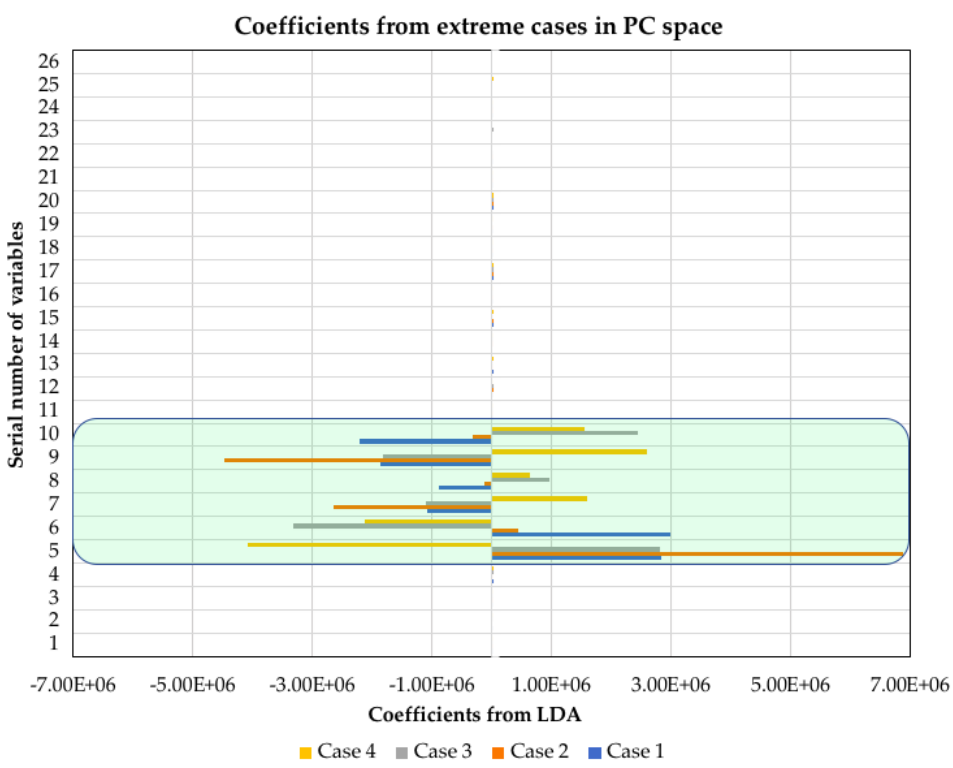

Figure 5.5. Coefficients of the discriminants for the cases that projected on the extreme ends in PC space. The serial numbers of the variables correspond to Table 5.3. Highlighted, are the variables whose coefficients fluctuate several orders of magnitude when the training data subsets are varied. These highlighted variables are treated as outliers and are removed from the analyses hereafter. For the data analyzed here, the variables related to the environmental relative humidity were identified as outliers.

RI | true RW) in Figure 5.4) are indicated by blue lines with discriminants less than S and red lines with discriminants greater than S. Note that the threshold (S) may be different in Figures 5.4a, 5.4b, and 5.4c.

Figure 5.4 demonstrates the following: (i) the discriminant computed with all the consistent set of variables taken together can effectively detect RI and RW with a high probability of detection and low probability of false alarm (ii) Between the three scenarios presented in Figure 5.4, the best predictive capabilities are achieved by using a combination of vortex and environmental variables.

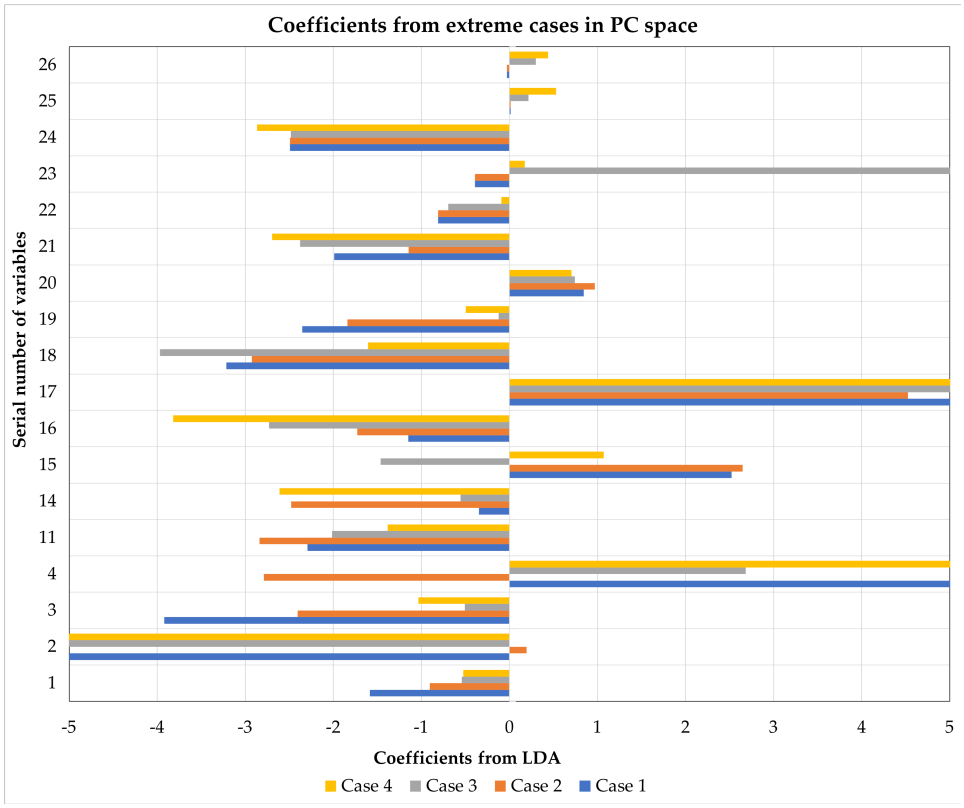

Figure 5.6. Same as Figure 5.5 except that at this juncture, the highlighted variables in 5.5 are removed. Note the immense reduction in axes bounds. A further round of screening is performed where the variables whose coefficients fluctuate in sign (but are still of same order of magnitude) when the training data subsets are varied. Finally, the covariance of the different variables was observed across the training period and a core of ten variables with little covariance amongst themselves, and whose magnitude and sign are consistent regardless of the chosen data subset are selected for further analyses.

5.1.6 Generic markers and their relative importance

We refer to the core subset of the most consistent variables presented in Figure 5.7a as generic markers, since they are the best instantaneous *symptoms* of a forthcoming rapid intensity change. This section compares the relative importance of the different subsets amongst the consistent variables. Figure 5.7a shows the coefficients computed using the LDA corresponding to each variable ($w_n = \alpha_n \sigma_n$ as defined in

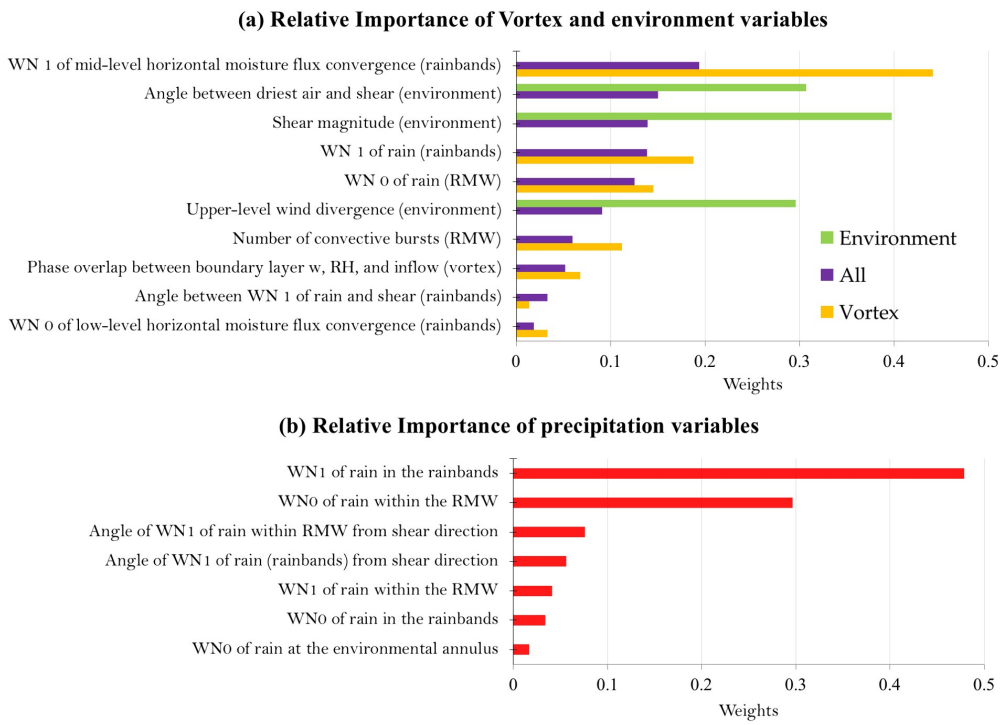

Figure 5.7. (a) Bar graph showing the weights (results of the LDA) that represent the relative importance of the environment and vortex variables. The purple bars show the results of the computation when all the variables are taken together; the golden bars show the results of LDA when only the vortex variables are taken together, and the green bars show the results of LDA when only the environment variables are taken together. (b) Same as (a) except that the bars indicate the results of LDA when only the precipitation variables within the vortex are considered.

Eqn. 5.7). Figure 5.7a depicts the coefficients associated with the individual variables. Here, the purple bars correspond to the scenario where all the variables are taken together; the golden bars correspond to the scenario where only the vortex variables are considered, and the green bars correspond to the scenario where only the environmental variables are considered for the LDA. At this juncture, it is important to note that the weights shown here are *in the context of* the other variables. Hence the term *relative* importance. By themselves, the importance of the variables may not mean anything unless they are placed in the context of the other variables/processes

Table 5.4.
Covariance matrix of the final set of variables computed across all the 1000 training subsets. Here, the above serial numbers (1 - 10) stand for the below variables: 1. 350 - 200 mb (upper-level) horizontal wind divergence (environment) 2. WN 0 of rain within RMW 3. Angle of the driest air from the direction of shear (environment) 4. WN 0 of 1000 - 850 mb horizontal moisture flux convergence (within RMW) 5. WN 1 of 850 - 700 mb horizontal moisture flux convergence (rain band region) 6. Magnitude of environmental vertical wind shear 7. Number of convective bursts within the RMW 8. Phase overlap between WN 1 of inflow, vertical velocity and RH within the boundary layer (vortex) 9. WN 1 of rain (rain band region) 10. Angle of WN1 of rain in the rain bands from the shear direction (vortex)

Covariance Matrix of the ten generic markers (consistent variables)										
	1	2	3	4	5	6	7	8	9	10
1	0.14	0.00	0.10	0.02	-0.04	0.07	0.00	0.02	0.13	-0.01
2	0.00	0.11	0.01	-0.01	-0.04	0.03	-0.03	0.01	-0.01	-0.02
3	0.10	0.01	0.12	0.01	-0.04	0.09	-0.01	0.03	0.13	-0.02
4	0.02	-0.01	0.01	0.01	0.01	0.00	0.00	0.00	0.01	0.02
5	-0.04	-0.04	-0.04	0.01	0.17	-0.08	0.00	-0.02	-0.06	0.02
6	0.07	0.03	0.09	0.00	-0.08	0.12	-0.01	0.03	0.11	-0.02
7	0.00	-0.03	-0.01	0.00	0.00	-0.01	0.05	0.00	-0.02	0.00
8	0.02	0.01	0.03	0.00	-0.02	0.03	0.00	0.05	0.04	0.00
9	0.13	-0.01	0.13	0.01	-0.06	0.11	-0.02	0.04	0.38	-0.01
10	-0.01	-0.02	-0.02	0.02	0.02	-0.02	0.00	0.00	-0.01	0.05

acting simultaneously since the LDA relies on the separation between *joint* probability distributions of RI and RW populations. Due to this, the weight for the same variable may change when it is considered as part of the vortex variables alone and when it is considered as part of the entire list.

Figure 5.7a reveals that the most important vortex-scale variables are the amplitudes of the asymmetric fields (WN 1) of 850-700 mb horizontal moisture flux convergence, and WN 1 of rain in the rainband region; and the amplitude of the symmetric field (WN 0) of rain within the RMW. Likewise, the angle between the driest air and the shear vector; and the magnitude of vertical wind shear are the most important environmental variables. The analysis also revealed that the sum of coef-

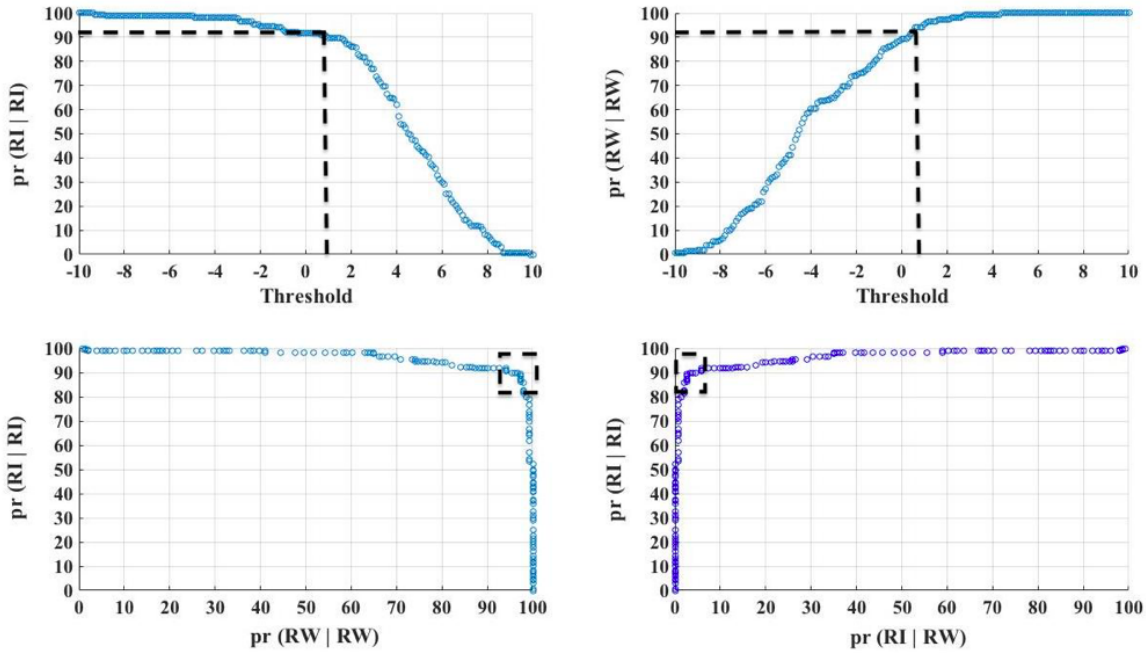

Figure 5.8. Demonstration of the selection of thresholds for the discriminant computed using coefficients averaged across the 1000 data subsets. Once the average coefficients are computed from the various subsets, the threshold (S) is varied between three standard deviations below to three standard deviations above. At each threshold, the estimated versus true probabilities of RI and RW for the mean discriminant are computed for all the cases. The threshold that produces the best combination of true positives and true negatives is selected. (a) Plot of the probabilities of the correct diagnosis of RI (true positives, pr (estimated RI — true RI)) for various thresholds. (b) Plot of probabilities of correct diagnosis of RW (true negatives, pr (estimated RW — true RW)) for various thresholds. (c) Plot of probabilities of correct diagnosis of RW (x-axis) versus probabilities of correct diagnosis of RI (y-axis) (d) Plot of probability of incorrect diagnosis of RI (false negative, pr (estimated RI — true RW)) versus probability of correct diagnosis of RI (true positive, pr (estimated RI — true RI)). The dashed regions and lines serve to illustrate that a threshold of 0.9 yields the best combination of true positives (91 percent) and true negatives (96 percent) corresponding to Figure 5.4c (all variables taken together).

ficients of all the environment variables compared to that of all the vortex variables (in the scenario where all of them were taken together) was 45:55. In other words, we

can conclude that the environment and vortex variables are equally important (with a five percent error) in influencing a rapid intensity change.

Figure 5.7b shows the weights of the LDA computed with just the precipitation (moist-convective) variables. Figure 5.7b reveals that the symmetric distribution of rain (WN 0) is most important within the RMW and that the asymmetric distribution (WN 1) is most important in the rain band region. Furthermore, Figure 5.7b indicates that the variables pertinent to the radial distribution of convection are more important than the azimuthal distribution with respect to the shear direction (both within the RMW and in the rain band region).

5.1.7 Discussions and Conclusions

The framework presented here offers a quantitative technique for testing the relative importance of the various external and internal processes influencing rapid intensity changes in TCs over the Bay of Bengal. The assumption here is that the modeled cases are representative of the spectrum of TC behavior in the Bay of Bengal. At the core of this framework is the LDA that takes in inputs from modeled cases segmented into two populations - RI and RW. Such a scenario is akin to a steady-state TC with RI and RW as two distinct attractor basins. Given that there are multiple pathways for the TC to be pushed into one attractor or the other, the LDA identifies the variables that have the most significant impact on the TC evolution. To reduce the dimensionality associated with the variables required to describe the instantaneous state of the vortex and its environment, a low-wavenumber reconstruction is performed before the LDA. The LDA then analyzes the joint probability distributions of the two populations and assigns coefficients based on how a particular variable affects the separation of the PDFs in the two populations. The best separation of the two predicted populations is achieved using a combination of the vortex and environmental variables. The coefficients suggest that the aggregate contribution from the environmental variables and the vortex variables are nearly equal.

Our analysis of the relative roles of symmetric and asymmetric convective processes suggest that the vortex responds more markedly to the changes in the symmetric component (WN 0) of precipitation rather than the asymmetric, deep bursts of convection within the RMW. The greater the amplitude of WN 0 within the RMW, the more conducive is the configuration for the TC to undergo RI as opposed to RW. This finding is consistent with those of [13, 119], and [61]. It must be noted it is possible that an RI in its *initial* stage may be driven by asymmetric convection. Over time, as the RI continues, the convection may then wrap around in the azimuth and the symmetric component may become dominant. However, such a distinction cannot be made in the present study and will require a pre-classification of the cases before the LDA. Outside the RMW, in the rainband region, the amplitudes of the asymmetric component (specifically WN 1 of precipitation and 850-700 mb horizontal moisture flux convergence) are seen to have a major influence.

The manner in which the WN 1 of 850-700 mb (mid-level eddy flux) convergence of moisture acts to influence intensification or weakening is not straightforward to interpret. For example, the mid-level horizontal eddy moisture flux may act to bring in dry (moist) air into the storm core [82] and aid in the rapid weakening (intensification) of TCs. On the other hand, if the flux convergence of moist air occurs in the rainband region as opposed to the inner-core region, then these eddy fluxes may aid the growth of the rainband thereby subtracting energy from the inner-core, and contribute to weakening. Likewise, the impact of WN 1 of precipitation in the rainband region on the TC undergoing RI/RW depends on the stage of the TC. If the TC is well developed, we speculate that the development of asymmetric precipitation in the rainband region will lead to weakening since the rainbands are subtracting energy from the TC core. On the other hand, in the early stages of the development of the TC, the asymmetric rain and convection in the rainband region may aggregate and advect radially inward into the core aiding in the intensification of the TC. Clearly, these topics require further investigation before we can arrive at definitive conclusions.

Furthermore, our results indicate that within the vortex, the amplitudes and radial location of asymmetric convection are more significant than the azimuthal phasing with respect to the shear in influencing a RIC. Again, the relative importance of the azimuthal distribution within the vortex might increase if the TCs are pre-classified such that only those that experienced moderate to high environmental shear are considered.

In the environmental annulus, the azimuthal phasing of the driest air is shown to be very important along with the magnitude of environmental shear. The impact of the magnitude of environmental vertical wind shear on TC intensity changes has been well documented ([15, 77, 127, 128] and references therein). In summary, these studies suggest that low magnitudes of wind shear are expected to aid in the TC's intensification and high magnitudes are expected to aid in the TC's weakening. Moderate wind shear magnitudes are sources of high uncertainty and either configuration is possible [72, 112]. Under such scenarios, the other external and intrinsic state variables are expected to dictate whether the TC will intensify or weaken. The alignment in the azimuthal phasing of the driest air with the shear vector will act to rapidly weaken the storm as evidenced by prior studies that have demonstrated the inhibitive role of dry air in the upshear quadrants [33, 37, 61, 72, 77].

Note that the identification of the 'most important' markers does not imply that these are *sufficient* to predict the evolution of the TC. For example, when the LDA was performed with just the two variables with the highest weights, the predictive capabilities were significantly worse than those presented in figure 5.4. This is because the variables with lesser weights help establish the context for the other variables to be more important. The correct way to interpret the coefficients is that they are weights in the sense that they magnify the effect of each variable. This means that if there is an uncertainty associated with these variables when they are fed in as inputs into a predictive model, their associated coefficients indicate how the uncertainty in those variables is magnified. From an observational perspective, we must know the

markers with higher weights much better than the other, by a factor equal to the ratio of their coefficients.

5.1.8 A note on available observations and limitations

A detailed note on the satellite observations that may be used for estimating the highest ranked variables and the current gaps in our observations that limit their utility is presented.

(a) ***The structure of the 700 - 850 mb horizontal moisture flux convergence in the rain bands***: To estimate this, we need vertically resolved observations of the moisture combined with observations of the flow at different levels. There are satellite observations and estimates of these parameters albeit with limited availability and certainty. The horizontal distribution of moisture in the 700 - 850 mb layer may be obtained from sounder observations such as the Atmospheric Infrared Sounder (AIRS) [129], Microwave Humidity Sounder (MHS) [130, 131], and the Advanced Technology Microwave Sounder (ATMS) [132]. However, their estimates are less reliable within the precipitating areas. Since we are interested in the rain band region particularly, observations from Radio Occultation measurements (GNSS-RO) [133] will be very valuable. While their vertical resolution is high, their limitation is the low spatial resolution ($\sim$150 km) and even more importantly, by their sporadic sampling that does not allow for the retrieval of the 2D structure of moisture. To estimate the flux convergence from observations, one would need observations of the flow field at a given layer. As of today, there are no direct observations of the flow field. However, tracking of features (moisture and/or clouds) has resulted in the development of algorithms to estimate the winds from Geostationary infrared (IR) observations. These Atmospheric Motion Vectors (AMVs) [134] have proven very valuable, in the absence of direct observations. However, cau-

tion must be taken while using them as they have uncertainty in the estimates of their altitude. Furthermore, they are absent inside the heavy cloud regions.

(b) ***The amplitude of WN 1 of the precipitation in the rain band region*** - There are a multitude of passive microwave observations from the imagers that are part of the GPM constellation such as Microwave Imager (GMI) [135], Advanced Microwave Scanning Radiometer - 2 (AMSR2) [136], and the Special Sensor Microwave Imager Sounder (SSMIS) [137]. Using the Rain Index - a multi-channel combination of the passive microwave observations [138], it is possible to easily detect the precipitating regions, by providing a radar-like depiction and a first order estimate of the rain intensity. Applying the wave number analysis to the Rain Index allows for a very reliable depiction of the rain bands.

(c) ***The amplitude of WN 0 of precipitation within the radius of maximum winds*** - The precipitation within the RMW region may also be detected using the Rain Index and the Wave number analysis. The radius of maximum winds may be detected using surface level scatterometer observations from the Advanced Scatterometer (ASCAT) [139] and RapidScat [140]

(d) ***The angle between the driest air and the shear vector in the environmental annulus*** - Again, the observations for moisture come from sounders and Radio Occultation measurements as described above. The estimation of shear comes from the atmospheric motion vectors (AMS) described above.

(e) ***The Magnitude of environmental vertical wind shear*** - From Atmospheric Motion Vectors (AMVs) described above.

While this section focuses on the Bay of Bengal where aircraft reconnaissance is absent, the methodology presented herein could be applied to other basins where reconnaissance is available. Under such scenarios, dropsondes can provide much higher

quality humidity and wind speed observations than the remotely sensed products and may be used to measure the variables of interest.

We further recommend that the observations of the generic markers with the highest coefficients be assimilated as inputs into TC forecasting models for best predictive capabilities.

5.1.9 Future work

In the future, we seek to test the above methodology for not just instantaneous inputs, but *tendencies* of variables and examine if that helps reduce uncertainty. Additionally, we intend to test the methodology using observations from satellites in addition to model outputs. By further separating the TC cases into sub-classes based on (i) shear magnitude (ii) intensity/stage of the vortex (e.g. nascent, developing, and mature) and (iii) proximity from land, it is possible to conduct the same analysis and see how the relative importance of the markers varied at different stages of a TC and for different classes of TCs. Furthermore, we seek to test the methodology for other basins such as the Atlantic and Pacific. An advancement of the technique used here would be an expanded representation of the problem nonlinearities, by including nonlinear transforms of the initial state variables (such as the flux convergence of moisture or θ_e). These topics will be explored in a follow-up study.

5.2 Stochastic model

(A version of this chapter is published in Earth and Space Science)

A fundamental limitation in developing indicators for complex systems is that they cannot be used to predict transitions in a deterministic sense. Stochastic shocks will always play an important role in triggering rapid intensity changes provided the vortex is preconditioned a certain way. For this purpose, in this section, we introduce a scale-specific stochastic model that computes the probabilities of episodic, tipping of a tropical cyclone vortex between a rapidly intensifying and a rapidly weakening configuration (two attractor basins) in response to an ensemble of stochastic forcings. Here, I build on the energetics-based diagnostic framework developed in Chapter 4, by adding a stochastic term whose memory and amplitude are varied for individual scales. The central idea here is to recognize that the stochastic shock may arise from any of the scales within and external to the vortex and then compute the probability of such a stochastic transition across an ensemble of scenarios.

The motivation for this work stems from the observation of Ed Lorenz who noted that small difference in the initial condition can be amplified over the integration time and have an impact on the meso- and synoptic-scale fields [141,142]. In addition to the specifications of the initial conditions for the vortex and the environment, uncertainty (stochasticity) may arise from one of the following sources: (i) Numerical formulation (ii) Misrepresentation of the model physics and/or the sub-grid scale parameterizations (iii) Inherent stochasticity in the process (especially convection) [143]. These concepts of error growth and the intrinsic predictability limits has been explored previously for TCs using ensemble simulations of perturbed initial conditions [114,143–146]. Alternatively, researchers have used an ensemble of models to produce a superior forecast as compared to individual model forecasts [147].

The relation between the previous works and the present work is the question of the predictability of asymmetries within a TC vortex. Judt et al. (2016) [114] investigated the error growth of individual wavenumbers within TCs whilst imposing stochastic

perturbations at various scales internal as well as external to the TC vortex. Forecast errors in the small-scales (wavenumbers ≥ 20) were found to grow rapidly and limit their predictability to around 6-12 hours. Medium-scales (wavenumbers 2 - 5) were found to have a predictability of 1-5 days, and the large-scales (wavenumbers 0 and 1), whose predictability was tied strongly to the environment, had a predictability limit of around 7 days. The predictability limit of each of the scales is inherently linked to their spatio-temporal scales of existence. With this background, we set out to model and quantify the system-scale probability of episodic, stochastic tipping of the TC vortex between an attractor basin that represents an intensifying configuration and one that represents a weakening configuration.

5.2.1 Stochastic Model description

Recall that equations 4.1 and 4.2 compute the kinetic energies of asymmetries at different length-scales. These equations account for the individual contribution of asymmetries at different length-scales; for different natures of interaction between the mean and asymmetries as well as asymmetries of different length scales; and for the contributions from external and intrinsic dynamic-thermodynamic processes.

We begin by rewriting the partial differential equation for kinetic energy, $K(n,t)$ as a first-order forward difference equation i.e.,

$$K(n,t) = K(n,t-\Delta t) + \Delta t * \frac{\partial K(n,t)}{\partial t} \tag{5.8}$$

where the $K(n,t)$ and $K(n,t-\Delta t)$ represent the kinetic energy at each scale at the current time-step and the previous time-step respectively. The time-step, Δt is 1 hour in this case. The $\frac{\partial K(n,t)}{\partial t}$ term is computed using the right hand side of equations 4.1 and 4.2. Recall that this term represents the combined effect of the source and/or sink terms that act to add or subtract energy at a given scale and time. At this stage, the mean-eddy, eddy-eddy, and the APE to KE terms have been pre-computed from model outputs at every time-step as discussed in Chapter 4.

We now add a scale-specific stochastic forcing term $\xi(n,t)$ to equation 5.8 in the following manner:

$$K(n,t) = K(n,t-\Delta t) + \Delta t * \frac{\partial K(n,t)}{\partial t} + \xi(n,t) \tag{5.9}$$

The questions that are yet to be addressed are (i) What is the nature of the perturbation? (ii) What is the amplitude of perturbation? (iii) Do the stochastic forcing have a memory or do they behave as memory-less white-noise? To answer these questions, we expand the $\xi(n,t+\Delta t)$ term in the following manner:

$$\xi(n,t) = \alpha(n) * \xi(n,t-\Delta t) + A(n,t) * w_t(t) \tag{5.10}$$

where $\alpha(n)$ is a scale-specific memory parameter; $A(n,t)$ is the scale-specific amplitude of the stochastic forcing; and the $w_t(t)$ term represents a random number that is extracted from a Gaussian distribution whose mean is 0 and variance, 1.0 (white-noise). At each time-step, the stochastic forcing is applied according to equation 5.10 and the $K(n,t)$ is updated. As noted previously, the $\frac{\partial K(n,t)}{\partial t}$ term is pre-computed using the right hand side of equations 4.1 and 4.2, and invoked at each time-step.

Note that this formulation is that of a first-order auto-regressive process where the stochastic forcing depends on the value at the previous time-step(s). The formulation described herein is a more sophisticated version of the stochastic kinetic-energy backscatter (SKEBS) method (cf. equation 5 of [143]). The novel feature of our implementation is the scale-specificity in the memory (with decorrelation time, τ) and amplitude terms. Building-off the above-mentioned previous studies, we recognize that the asymmetries at lower wavenumbers (WNs 0-1 and 2 to 5) have a higher persistence in time and therefore, are associated with some memory. On the other hand, the higher wavenumbers (WNs > 5) are associated with no memory and are stochastic in nature. For this purpose, we write $\alpha(n)$ as a step function which assigns a decorrelation time (τ) of 12 hours to WNs 0 and 1, 6 hours to WNs 2 to 5, and no memory to WNs > 5. The memory parameter, $\alpha(n)$ and the decorrelation time, $\tau(n)$ are related in the following manner:

$$\alpha = \frac{\tau - 1}{\tau} \tag{5.11}$$

The forcing amplitude $A(n,t)$ is one hundredth of the actual amplitude of $K(n,t)$ computed using equations 4.1 and 4.2 for each scale and time. In other words, the scale-specific forcing amplitude, $A(n,t)$ mimics the actual distribution of energies, $K(n,t)$. Since the amplitudes of the kinetic energy (or power) across the different wavenumbers is distributed in the form of a power law (i.e., the lower wavenumbers carry the majority of the variance. cf. Figure 4.1), the amplitude of the stochastic term also follows suit.

A notable difference between the implementation presented herein and the SKEBS methodology is that their stochastic perturbation was added at the *start of the forecast cycle* for each ensemble into the flow field. On the other hand, in our methodology, we have the model outputs a priori from HWRF or an equivalent model. As a result, we have the 'source-sink' terms computed at each time-step. The stochastic forcing is applied as a separate diagnostic that is independent from the actual model run. The ensembles presented herein are diagnostic ensembles in that the actual fields of the environment or vortex is not perturbed. Only the effect of such external and intrinsic fluctuations at asymmetries of various scales within the vortex is simulated herein.

Once we have the modified kinetic energies for each scale and time, we invoke Parseval's theorem to derive the aggregate kinetic energy of the vortex. Parseval's theorem states that energy (or power) is conserved irrespective of whether we are working in physical space or Fourier-space. Therefore, the system-scale kinetic energy is just the sum of the kinetic energies at individual wavenumbers.

This procedure is iteratively repeated to create an ensemble of scenarios and the aggregate kinetic energy evolution of the vortex is derived for each scenario. Finally, the number of transitions into either intensification or weakening configurations is computed across the ensembles and the probability of transition to either state is presented.

5.2.2 Results and Discussion

Figure 5.9 shows the time-evolution of the aggregated kinetic energy in Phailin and Lehar for an ensemble of 100 realizations with stochastic forcing (gray lines). The red, dashed line indicates the aggregated kinetic energy computed with no stochastic forcing. The first impression from Figure 5.9 is that the distribution of the realizations is not bi-modal i.e., the realizations cannot be classified into two bins as RI or RW. The distribution of the simulated ensemble does resemble the distribution of TCs in the real-world where RI and RW are not the only attractor basins, they simply represent the extremes.

Second, the memory term in the stochastic forcing plays an important role in the build-up of the system-scale memory in kinetic energy. The build-up of memory results in a positive feedback loop that may tip the vortex into an increasingly intensifying configuration. On the other hand, since the amplitude of noise mimics the actual distribution of kinetic energy, when the sink terms increase (e.g., when the conversion from potential to kinetic energy is reduced post-landfall or due to dry-air intrusion), the noise term also reduces (negative-feedback). Due to the above two balancing acts, there is a large variation in the *timing* of the rise and fall of kinetic energy (Figures 5.9a,b).

Figures 5.10a,b show the probability density functions (PDFs) of aggregated kinetic energy across all ensembles at each time. The PDFs indicate how the mean and variance evolve for the two TCs across their life-cycles. For both of the TCs, the variance increases with time (as evidenced by the broadening of the PDF violins) due to the memory and feedbacks discussed above. The red dots in Figures 5.10a,b indicate the median (fiftieth percentile) of the PDFs at each time [3] The trajectory of the median broadly indicates the growth or decay of kinetic energy with time. Note that the evolution of the median is analogous to the KE evolution without any stochastic forcing (cf. red, dashed lines in Figure 5.9).

[3]The median is chosen instead of the mean at this juncture since a single (outlier) realization at a particular time can significantly influence the mean giving a false impression of increase or decrease.

There are two ways to issue a probabilistic forecast based on this ensemble. The first method is to simply track the number of realizations that underwent a rapid increase or decrease in kinetic energy over the course of the simulation. However, since we are dealing with kinetic energy and not intensity, there is no equivalent definition for RI or RW (change in intensity of 30 knots over 24 hours). Therefore, any definition at this point is arbitrary. A way forward may be to plot a PDF of the change in 24-hour kinetic energy computed between each time t, and t+24. Consequently, the number of realizations that underwent the 95th percentile of change in KE may be compared to the total number of realizations. The change in KE will also reflect the positive or negative feedbacks as a result of the stochastic forcing.

The second method is to pick the most realistic member(s) from the ensemble by comparing the evolution of KE with observations. Of course, this is conditioned on the availability of some observational estimate of the 'truth'. At this point, our observational capacity to measure the flow-field of the entire vortex (and therefore, the aggregate kinetic energy) in three dimensions at a good temporal resolution is lacking. However, if we restrict the focus to surface-based measurements of winds, then this method may be explored due to the availability of scatterometer observations (among others).

Summary

A scale-specific stochastic model that offers immense scope for the probabilistic forecasting of TC rapid-intensity changes is presented here. We have attempted to model the stochastic term in a realistic manner by treating the lower-wavenumbers and higher-wavenumbers differently. As a result, the ensembles generated here mimic the distribution of TCs in the real world. Further work is necessary to define the critical thresholds that can be used for the probabilistic forecasting of RI and RW.

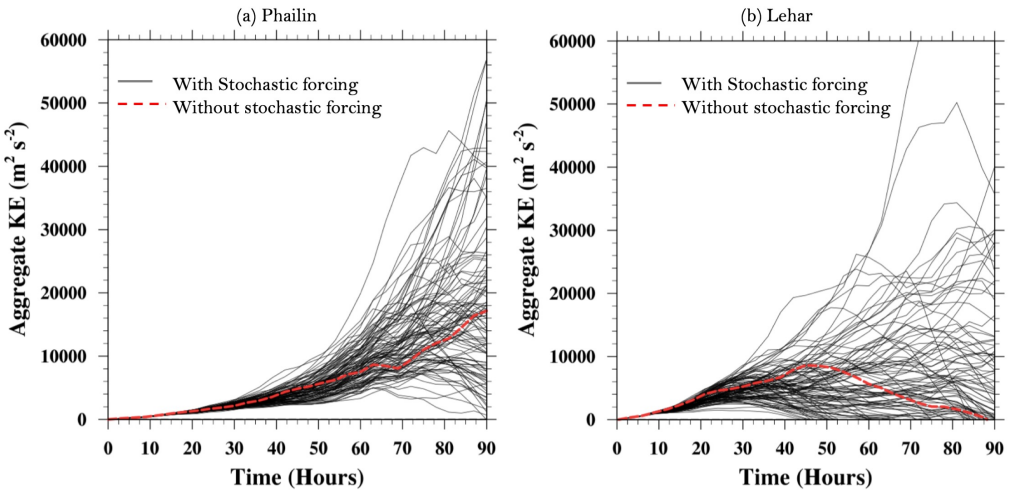

Figure 5.9. Simulations of aggregate kinetic energy (sum of kinetic energy across all wavenumbers; spatially averaged through the depth of the vortex and between 0-300 km radii) for (a) Phailin (b) Lehar. The gray lines represent individual realizations with the addition of stochastic forcing. The dashed, red line represents the aggregate kinetic energy computed without any stochastic addition.

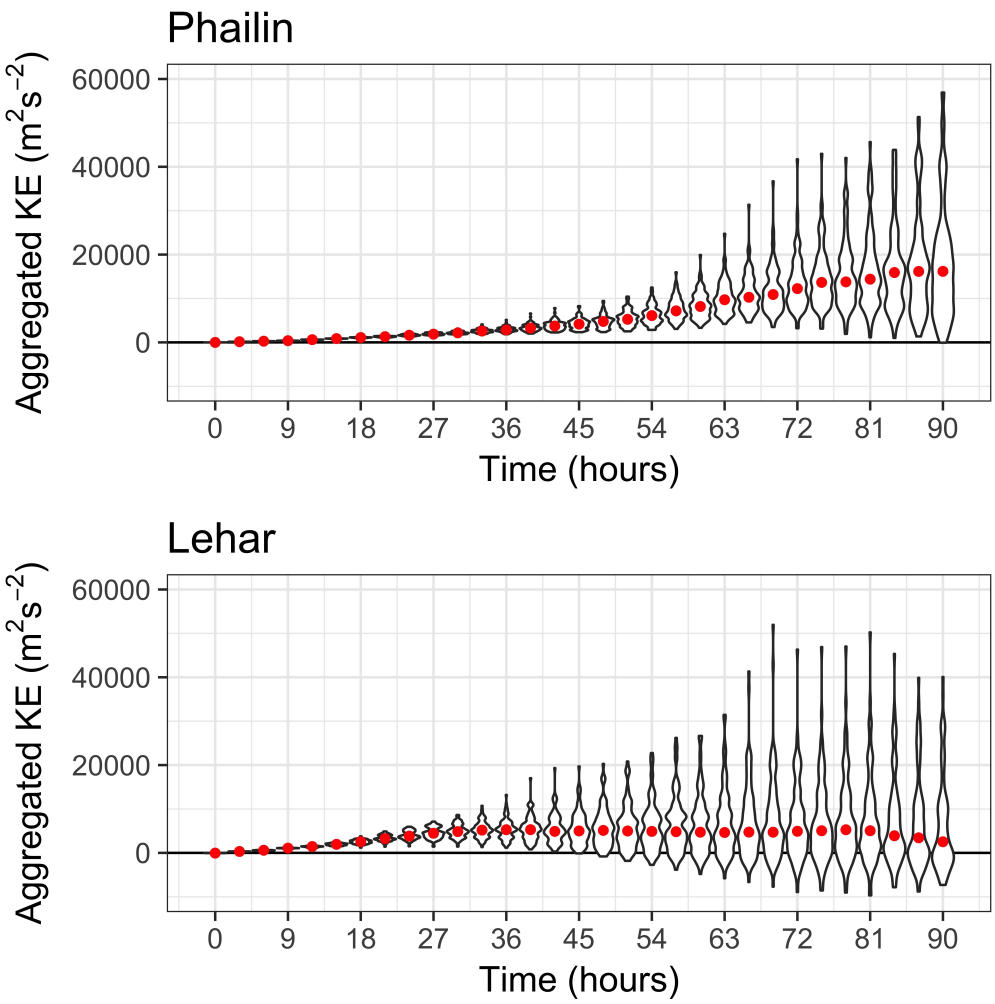

Figure 5.10. A violin plot of the probability density function (PDF) of aggregated KE (across all ensembles) at each time. The red dots indicate the median of the PDF at each time.

6 SYN-THESIS

Our collective understanding of asymmetric features such as eddies and waves within the large-scale, coherent structure of a tropical cyclone, continues to improve with the availability of more detailed observations and high-resolution model outputs. The growth or decay of these asymmetries is an interesting problem since their dynamics are strongly linked to the intensification or weakening of the TC vortex. Interestingly, recent studies have shown that these asymmetries may positively or negatively influence the vortex. Such findings imply that with our current understanding, the mere presence of asymmetries within a TC does not tell us anything in advance regarding the probability of consequent change in TC intensity. It behooves us to better understand and characterize the nature of asymmetries in the context of the predictability of at least the extreme scenarios viz. periods of *rapid* intensity changes. This naturally motivates the question: Under what scenarios do asymmetric TC vortices spiral towards (rapid) intensification as opposed to (rapid) weakening and vice versa?

In this thesis, I take the first steps towards establishing the basis of such predictive capability (of asymmetries) through diagnosis of model output and satellite imagery. It became apparent to us at an early stage that there is no single silver bullet approach to this problem. As a result, multiple diagnostic frameworks that compliment each other are presented herein. In this chapter, I first summarize the conclusions and their implications from the rest of the chapters. This is followed by a set of recommendations. Finally, I close by describing future opportunities that stem from the current work.

6.1 Epilogue

At the very outset, this thesis investigates the spatial, spectral, and temporal characteristics of multi-scale asymmetries induced by a combination of external and intrinsic sources. Our numerical investigation of a sheared vortex reveals the creation of preferential zones (local environments) within the vortex that serve to support or disrupt the organization in convection. These local environments are created by the spatial juxtaposition of several asymmetric dynamic-thermodynamic fields viz. θ_e, radial velocity, relative vorticity, and vertical velocity. The presence of low-θ_e air (anti-fuel) in the vicinity (e.g., radii $\geq$ 100 km from storm center) of the TC does not imply that the TC will weaken. We show that the rapid weakening of the TC is triggered only when the downward flux of low-θ_e air through the top of the boundary layer collocates favorably with the radially inward flux of low-θ_e air within the boundary layer. Such a juxtaposition opens up a pathway for the anti-fuel from outside the storm to intrude into the TC core and impede the development of convection. In addition to a phase synchronization, a synchronization in the peak of the amplitude of the downward and radially inward fluxes of low-θ_e air was also noted. The synchronization in both the magnitude and the phase happens particularly in the upshear-left quadrant between 40-80 km radii in our case-study of interest.

We also note that in certain regions within the sheared vortex (e.g., 6-10 km in the vertical), the eddy flux arising from the asymmetric distribution of vorticity may serve to have a positive influence on the TC intensity change. However, such an influence may be counteracted by the eddy fluxes of low-θ_e air in the same region, thereby superseding the effect of the dynamic variable. This is an important finding as it reveals that the rapid weakening may occur in a sheared environment even if the conditions are dynamically favorable. Importantly, as shear reorganizes the fields of vorticity, θ_e, radial velocity, and the convective upward/downward motions in the azimuthal direction, looking for signatures in the individual fields might be misleading given the competing nature of the mechanisms associated with these fields. Rather,

we must attempt to understand the juxtaposition of these asymmetric fields and how their behavior evolves in the context of one another and the external environment.

At this juncture, it is unclear as to what determines the phasing of the dynamic-thermodynamic fields. Why is it in-phase during certain times and why is it out-of-phase at other times? However, the key takeaway here is that despite not understanding all the details of the system, the juxtaposition in the vertical and horizontal fluxes of low-θ_e air acts as an early warning signal for a forth-coming rapid intensity change. Additionally, by identifying these preferential zones, we have essentially developed a resilience map of the TC vortex. For example, the upshear-left quadrant is the fragile zone that is vulnerable to the intrusion of the anti-fuel from the environment and the downshear-right quadrant is the most resilient.

In low-sheared vortices, when the fields of θ_e and radial velocity are symmetrically distributed, the generic markers developed for sheared vortices might not apply. Our analyses shows that under such scenarios, the strength of the radial inflow within the boundary layer and the radial location of boundary layer convergence relative to the radius of maximum wind act as symptoms of the forthcoming critical transition. A tangential momentum budget analysis revealed that the collocations of the regions of cyclonic relative vorticity and upward vertical velocity are seen to positively aid in the local spin. Such a collocation happens along the eyewall region throughout the depth of the vortex. Additionally, the eddy fluxes of vorticity are shown to positively contribute to a system-scale spin-up by radially advecting positive vorticity across the loop that encircles region of interest thereby increasing the circulation.

In Chapter 4, I apply an energetics-based diagnostic known as scale interactions that allows us to examine the behavior of asymmetries at multiple length-scales in spectral space. By applying it to select cases, this thesis uncovers the relative importance of the energy pathways that support or disrupt the growth of asymmetries at various length-scales within the vortex. Contrary to the conventional wisdom that the convective aggregation/disaggregation and axi/asymmetrization occurs through barotropic mean-eddy transactions, my thesis reveals that the mechanisms of growth

or disruption of asymmetries (i) the baroclinic conversion from available potential to kinetic energy at individual scales of asymmetries and (ii) the transactions of kinetic energy between the asymmetries of various length-scales. In other words, the energy being transferred amongst the asymmetries of different length-scales is far greater than the amount transferred between the mean and the asymmetries. This finding applies to both the convective aggregation that occurs during the genesis of the storm as well as during rapid intensification. Our analysis also shows that the growth of asymmetries may occur independent of the growth or decay of the mean (not necessarily at the expense of the mean).

In Chapter 5, I quantify the relative importance of symmetric and asymmetric convection within the vortex in the context of other intrinsic and external state variables during time periods that just precede rapid intensity changes. For this purpose, we developed an empirical model based on the instantaneous states of external and intrinsic variables taken across simulations of a suite of TCs that experienced rapid intensity fluctuations over the Bay of Bengal. This empirical model was the laboratory for testing the relative importance of the various indicators discovered from individual cases (described in previous chapters). The first key result was that the aggregate contribution to rapid intensity changes from the intrinsic and environmental variables was nearly equal. Next, our analysis indicates that different regions of the vortex respond differently to symmetric and asymmetric fields. For example, the region within the radius of maximum winds responded more markedly to the changes in the symmetric component whereas the rain band region responded to the asymmetric component. The environment was sensitive to the magnitude of shear as well as the azimuthal phasing between the low θ_e air and the shear vector.

A fundamental limitation in developing indicators for complex systems is that they cannot be used to predict transitions in a deterministic sense. Stochastic shocks will always play an important role in triggering rapid intensity changes provided the vortex is preconditioned a certain way. For this purpose, in Chapter 5, we introduce a scale-specific stochastic model that computes the probabilities of the vortex tipping into an

intensifying or weakening configurations given an ensemble of scenarios. Here, I build on the energetics-based diagnostic framework developed in Chapter 4, by adding a stochastic term whose memory and amplitude are varied for individual scales. The key idea here is to recognize that the stochastic shock may arise from any of the scales within and external to the vortex and then compute the probability of such a stochastic transition across an ensemble of scenarios.

In summary, my thesis contribution is the development of diagnostic lenses that allow us to examine and characterize an (a)symmetric vortex and predict if it is going to rapidly intensify or weaken with $x\%$ probability. My research is a stepping stone toward a fundamental change in the way the scientific community understands and treats asymmetries in the context of tropical cyclone rapid intensity changes.

6.2 Specific Recommendations

A list of specific recommendations targeted at aiding the real-time forecasting of asymmetric vortices is compiled below.

1. **Identify the source of asymmetries**: The first step towards understanding the characteristics of asymmetries is to understand their source. Asymmetries induced by the environment-vortex interactions usually manifest as WNs 1 or 2. Their persistence in time and space is directly linked to the time-period of the external forcing and the adjustment period of the vortex to attain thermal-wind or quasi-geostrophic balance with the environment. In the absence of a dominant external force such as shear or land, asymmetries that manifest as WNs 1 or 2 purely due to forces intrinsic to the vortex behave differently from their externally induced counterparts.

   (a) Note: Shear must not be treated as a one-way forcing from the environment on to the vortex. We must acknowledge that in reality, the vortex feeds back onto the environment and (potentially) modifies its own local shear. We need to move away from the traditional bulk-shear definitions

as they might under-represent the structural complexity of the vortex and the environmental flow-field in three dimensions. The shear profile in the vertical impacts the phasing of the convection, θ_e, and radial inflow.

(b) Note: In this study, the center of the coordinate system was always a surface-based, minimum pressure centroid. However, in sheared environments, when the vortex is tilted, the circulation center may vary significantly at different altitudes. For this purpose, sensitivity experiments with the center of the coordinate system may be necessary.

2. **Look at the azimuthal phasing between θ_e, vorticity, inflow, and updrafts/downdrafts within the vortex**: Our research has demonstrated that individual asymmetric fields never present a true picture and are often counter-intuitive in their behavior over time. For the holistic picture, it is necessary to look at the phase overlap between the above-mentioned variables.

3. **Radial location of convection v/s azimuthal phasing with respect to shear**: In more symmetric storms and at radii very close to the radius of maximum winds, the radial location of convection may take precedence over the azimuthal distribution with respect to shear. The azimuthal phasing with respect to the shear vector takes precedence at radii greater than the radius of maximum winds - particularly the rain band region and in the environment. In addition to the shear vector, the storm motion vector and the phase alignment between the two may also decide the phasing and the relative importance of such phasing in convection and other related variables.

4. **Use the scale-interactions framework to compute the three energy pathways for an asymmetry at any given scale**. The scale-interactions framework computes the non-linear transactions at each scale through three pathways: the barotropic pathway, the baroclinic pathway and the across-scale pathway. The barotropic transactions tell us whether the vortex is maintained by symmetric or asymmetric convection. The magnitude and direction of the

baroclinic and across-scale transactions tell us whether an asymmetry at a given length scale is growing or decaying. WNs 0,1, and 2 are the dominant scales from the perspective of impact on the vortex-scale. Examination of the baroclinic transactions and the upscale and downscale transfer of energy to WNs 0,1, and 2 will aid in the prediction of vortex-scale rapid intensity changes.

5. **Asymmetries must be treated independent from the mean**: Our research has shown that the growth and decay of asymmetries occur nearly independent of the dynamics in the mean. In other words, the growth of asymmetries need not happen at the expense of the mean. Even if direction of transfer is from the mean to wavenumbers 1 and 2, energetics at these low wavenumbers are capable of sustaining the vortex during an intensification period. In any case, the order of magnitude of such a barotropic transaction between the mean and eddy term is much smaller than the transactions through alternative pathways. Using purely barotropic models or linear models will lead to incorrect conclusions about the nature of asymmetries.

6. **Do not neglect the small-scale asymmetries**: The generation of available potential energy and the subsequent conversion to kinetic energy happens at asymmetries of every individual length-scales. Although the generation and conversion terms in the higher wavenumbers were one order of magnitude smaller than that of the lower wavenumbers, their magnitudes were not insignificant. Second, the cross-scale energy exchanges were found to be a significant influence on the aggregation and disaggregation of convection and system-scale kinetic energy. As a result, while the small-scale asymmetries are transient and may not manifest at time-scales that are typical for forecasting purposes, they project on to the large-scale asymmetries that are persistent in time. Importantly, combining points 5 and 6, asymmetries must not be treated as inhibitive features that subtract energy from the mean. Rather, they must be treated as an inherent

part of the vortex dynamics and the very aggregation of individual cloud entities in the azimuth is what results in the meso-scale and vortex-scale organization.

7. **Prioritize the important variables identified here during observational and data-assimilation efforts**: The empirical model introduced here may be used as a framework for the identification of the most important variables within a given region of interest. These variables are important in the sense that they have a significant influence on rapid intensity changes and any initial condition error associated with these variables will be amplified at a greater scale compared to the other variables.

   (a) Note: Different regions within the vortex respond differently to symmetric or asymmetric components of various fields. For example, our analysis showed that the region within the radius of maximum winds responded to the symmetric component of moist-convection and the rain-band region responded to the amplitude of the asymmetric component of moist-convection.

   (b) Note: Both the amplitude and the phasing of asymmetries are important within different regions and during different stages of the vortex.

8. **Move towards probabilistic forecasting** In reality, there are uncertainties in our knowledge of the initial state. This, coupled with the inherent nonlinearity in the system, makes it unwise to rely solely on deterministic forecasts. The linear-discriminant-based model and the stochastic model (using an ensemble of cases) detailed in this thesis are efforts in this direction.

6.3 Future Work

The work presented herein was only the first step towards demystifying the behavior of asymmetries within a TC vortex. A lot of work remains to be done.

- First, a more physical understanding of the processes that determine the phase locking or unlocking of the various fields is necessary. At this stage it is unclear if there is a fundamental mechanism that dictates the azimuthal phasing, or if the azimuthal phasing of each of the individual fields are independent and the juxtaposition is mere happenstance.

- In this thesis, the case-studies chosen represent the extremes viz. rapid weakening in a sheared environment and rapid intensification in a low sheared environment. It remains to be tested whether the asymmetric rapid intensification may be diagnosed by the favorable juxtaposition of warm and moist θ_e, inflow, and updrafts in the upshear quadrants. Further, the diagnostic metrics presented here must be tested for vortices in moderately sheared environments and for moderate intensity changes ($\leq$ 15 knots) where the uncertainty is the highest [112].

- The analysis presented here may be extend to understand environment-vortex or vortex-vortex interactions. For example, one might ask what scales in space and time best describe the anomalies in the TC environment and what scales and energy pathways are required to maintain such a set-up. Once we have a mature understanding of what the dominant scales are in the TC-environment and within the TC-vortex, we can investigate as to how these scales communicate with one another.

- Furthermore, we can use the techniques described here to diagnose how well the energy exchanges are being handled by the TC forecast models. Once we have a base state of understanding of what to expect in an RI or RW scenario, we can evaluate the performance of the model in representing the processes that lead to such critical transitions. Such information can potentially aid in the improvement of the components in the model that directly influence the aggregation and disruption of the organization in convection. The dynamics, representation of grid-scale and subgrid-scale cumulus convection and model

diffusion are the elements in a forecast model that need to be studied in this context.

- Further testing with the empirical models across basins other than the Bay of Bengal, with a combination of satellite and model outputs, and for a larger sample of TCs is warranted to make statistically significant conclusions about the behavior of asymmetries.

- A sensible follow-up to the stochastic model presented here will be towards a more analytical approach. This will especially be useful for cases where we do not have the energetics computed a priori for each scale at every time. Using an empirical approach, it might be possible to know the nature of the probability functions for each of the terms and derive an analytical solution.

6.4 Applicability to complex systems outside tropical cyclones

Tropical Cyclones are examples of highly-interconnected, heterogeneous, complex, dynamical systems. There are several other complex systems we encounter in our daily lives - e.g., the human brain, ecosystems, financial markets, and socio-technological systems. A study of these systems - their response, failure, and resilience to external and stochastic shocks in a unified sense, has been the topic of complex systems literature [148–150]. The focus of such studies has been on anticipating and adapting to regime shifts in the state of these systems even when our understanding of the details of the system behavior is limited [151–153]. Our study of the behavior of the TC vortex in response to external and intrinsic forces is very analogous to the above-mentioned studies.

For highly stochastic systems with alternative stable states (or attractor basins analogous to rapid intensification and weakening in this thesis), Scheffer et al. (2012) [152] provide a review of the various early-warning indicators or generic markers of transitions between the stable states in different complex systems. Under scenarios where deterministic solutions are not possible, the best path forward may be to de-

velop such early warning indicators and resilience maps that indicate the regions that are more susceptible and regions that are resilient to such external stressors. In spirit, this is precisely what my thesis attempts to achieve.

REFERENCES

[1] William K George. Lectures in turbulence for the 21st century. *Chalmers University of Technology*, 2013.

[2] Katsuyuki V Ooyama. Conceptual evolution of the theory and modeling of the tropical cyclone. *Journal of the Meteorological Society of Japan. Ser. II*, 60(1):369–380, 1982.

[3] Kerry A Emanuel. The theory of hurricanes. *Annual Review of Fluid Mechanics*, 23(1):179–196, 1991.

[4] Frank D Marks and Lynn K Shay. Landfalling tropical cyclones: Forecast problems and associated research opportunities. *Bulletin of the American Meteorological Society*, 79(2):305–323, 1998.

[5] Michael T Montgomery and Roger K Smith. Recent developments in the fluid dynamics of tropical cyclones. *Annual Review of Fluid Mechanics*, 49:541–574, 2017.

[6] Katsuyuki Ooyama. Numerical simulation of the life cycle of tropical cyclones. *Journal of the Atmospheric Sciences*, 26(1):3–40, 1969.

[7] Kerry A Emanuel. 100 years of progress in tropical cyclone research. *Meteorological Monographs*, Early Online Release, 2018.

[8] Frank D Marks Jr and Robert A Houze Jr. Airborne doppler radar observations in hurricane debby. *Bulletin of the American Meteorological Society*, 65(6):569–582, 1984.

[9] Frank D Marks, Robert A Houze Jr, and John F Gamache. Dual-aircraft investigation of the inner core of hurricane norbert. part i: Kinematic structure. *Journal of the Atmospheric sciences*, 49(11):919–942, 1992.

[10] Shuyi S Chen, John A Knaff, and Frank D Marks Jr. Effects of vertical wind shear and storm motion on tropical cyclone rainfall asymmetries deduced from trmm. *Monthly Weather Review*, 134(11):3190–3208, 2006.

[11] Richard A Anthes. Development of asymmetries in a three-dimensional numerical model of the tropical cyclone. *Monthly Weather Review*, 100(6):461–476, 1972.

[12] Nguyen Van Sang, Roger K Smith, and Michael T Montgomery. Tropical-cyclone intensification and predictability in three dimensions. *Quarterly Journal of the Royal Meteorological Society*, 134(632):563–582, 2008.

[13] Sundararaman G Gopalakrishnan, Frank Marks Jr, Xuejin Zhang, Jian-Wen Bao, Kao-San Yeh, and Robert Atlas. The experimental HWRF system: A study on the influence of horizontal resolution on the structure and intensity changes in tropical cyclones using an idealized framework. *Monthly Weather Review*, 139(6):1762–1784, 2011.

[14] Sarah C Jones. The evolution of vortices in vertical shear. i: Initially barotropic vortices. *Quarterly Journal of the Royal Meteorological Society*, 121(524):821–851, 1995.

[15] William M Frank and Elizabeth A Ritchie. Effects of vertical wind shear on the intensity and structure of numerically simulated hurricanes. *Monthly Weather Review*, 129(9):2249–2269, 2001.

[16] Scott A Braun. A cloud-resolving simulation of hurricane bob (1991): Storm structure and eyewall buoyancy. *Monthly Weather review*, 130(6):1573–1592, 2002.

[17] Herbert Riehl and Joanne Malkus. Some aspects of hurricane Daisy, 1958. *Tellus*, 13(2):181–213, 1961.

[18] Eric A Hendricks, Michael T Montgomery, and Christopher A Davis. The role of vortical hot towers in the formation of tropical cyclone Diana (1984). *Journal of the Atmospheric Sciences*, 61(11):1209–1232, 2004.

[19] Stephen R Guimond, Gerald M Heymsfield, and F Joseph Turk. Multiscale observations of hurricane Dennis (2005): The effects of hot towers on rapid intensification. *Journal of the Atmospheric Sciences*, 67(3):633–654, 2010.

[20] MT Montgomery, ME Nicholls, TA Cram, and AB Saunders. A vortical hot tower route to tropical cyclogenesis. *Journal of the Atmospheric sciences*, 63(1):355–386, 2006.

[21] HE Willoughby. Inertia-buoyancy waves in hurricanes. *Journal of the Atmospheric Sciences*, 34(7):1028–1039, 1977.

[22] Michael T Montgomery and Randall J Kallenbach. A theory for vortex rossby-waves and its application to spiral bands and intensity changes in hurricanes. *Quarterly Journal of the Royal Meteorological Society*, 123(538):435–465, 1997.

[23] Yongsheng Chen and MK Yau. Spiral bands in a simulated hurricane. part i: Vortex rossby wave verification. *Journal of the Atmospheric sciences*, 58(15):2128–2145, 2001.

[24] EA Hendricks, WH Schubert, SR Fulton, and BD McNoldy. Spontaneous-adjustment emission of inertia-gravity waves by unsteady vortical motion in the hurricane core. *Quarterly Journal of the Royal Meteorological Society*, 136(647):537–548, 2010.

[25] Yumin Moon and David S Nolan. Do gravity waves transport angular momentum away from tropical cyclones? *Journal of the Atmospheric Sciences*, 67(1):117–135, 2010.

[26] Robert A Houze, Wen-Chau Lee, and Michael M Bell. Convective contribution to the genesis of hurricane Ophelia (2005). *Monthly Weather Review*, 137(9):2778–2800, 2009.

[27] TN Krishnamurti, S Pattnaik, L Stefanova, TSV Vijaya Kumar, Brian P Mackey, AJ Oshay, and Richard J Pasch. The hurricane intensity issue. *Monthly Weather review*, 133(7):1886–1912, 2005.

[28] David Raymond, Željka Fuchs, Saška Gjorgjievska, and Sharon Sessions. Balanced dynamics and convection in the tropical troposphere. *Journal of Advances in Modeling Earth Systems*, 7(3):1093–1116, 2015.

[29] David S Nolan and Lewis D Grasso. Nonhydrostatic, three-dimensional perturbations to balanced, hurricane-like vortices. Part ii: Symmetric response and nonlinear simulations. *Journal of the Atmospheric sciences*, 60(22):2717–2745, 2003.

[30] David S Nolan, Yumin Moon, and Daniel P Stern. Tropical cyclone intensification from asymmetric convection: Energetics and efficiency. *Journal of the Atmospheric Sciences*, 64(10):3377–3405, 2007.

[31] John Persing, Michael T Montgomery, J McWilliams, and Roger K Smith. Asymmetric and axisymmetric dynamics of tropical cyclones. *Atmos. Chem. Phys*, 13(12):299–12, 2013.

[32] Roger K Smith, Jun A Zhang, and Michael T Montgomery. The dynamics of intensification in a hurricane weather research and forecasting simulation of hurricane earl (2010). *Quarterly Journal of the Royal Meteorological Society*, 143(702):293–308, 2017.

[33] Hua Leighton, Sundararaman Gopalakrishnan, Jun A Zhang, Robert F Rogers, Zhan Zhang, and Vijay Tallapragada. Azimuthal distribution of deep convection, environmental factors, and tropical cyclone rapid intensification: A perspective from hwrf ensemble forecasts of hurricane edouard (2014). *Journal of the Atmospheric Sciences*, 75(1):275–295, 2018.

[34] SSC Shenoi, D Shankar, and SR Shetye. Differences in heat budgets of the near-surface arabian sea and bay of bengal: Implications for the summer monsoon. *Journal of Geophysical Research: Oceans*, 107(C6):5–1, 2002.

[35] Peter J Webster, Greg J Holland, Judith A Curry, and H-R Chang. Changes in tropical cyclone number, duration, and intensity in a warming environment. *Science*, 309(5742):1844–1846, 2005.

[36] SD Kotal and SK Roy Bhowmik. Large-scale characteristics of rapidly intensifying tropical cyclones over the Bay of Bengal and a rapid intensification (RI) index. *Mausam*, 64(1):13–24, 2013.

[37] Bhalachandran Saiprasanth, R Nadimpalli, K. K Osuri, Frank Marks Jr, S G Gopalakrishnan, S Subramanian, U. C Mohanty, and D Niyogi. On the processes influencing rapid intensity changes of tropical cyclones over the bay of bengal. *Scientific Reports*, Manuscript submitted, 2018.

[38] Odisha State Disaster Management Authority. Disaster management in odisha. Technical report, Odisha State Disaster Management Authority, 2016.

[39] Nasreen Akter and Kazuhisa Tsuboki. Role of synoptic-scale forcing in cyclogenesis over the bay of bengal. *Climate dynamics*, 43(9-10):2651–2662, 2014.

[40] M Mohapatra, GS Mandal, BK Bandyopadhyay, Ajit Tyagi, and UC Mohanty. Classification of cyclone hazard prone districts of india. *Natural hazards*, 63(3):1601–1620, 2012.

[41] Uma Charan Mohanty and Sundararaman G Gopalakrishnan. *Advanced Numerical Modeling and Data Assimilation Techniques for Tropical Cyclone Predictions*. Springer, 2016.

[42] UC Mohanty, Krishna K Osuri, Sujata Pattanayak, and P Sinha. An observational perspective on tropical cyclone activity over indian seas in a warming environment. *Natural hazards*, 63(3):1319–1335, 2012.

[43] Russell L Elsberry, Greg J Holland, Hal Gerrish, Mark DeMaria, Charles P Guard, and Kerry Emanuel. Is there any hope for tropical cyclone intensity prediction? a panel discussion. *Bulletin of the American Meteorological Society*, 73(3):264–277, 1992.

[44] Eric A Hendricks, Melinda S Peng, Bing Fu, and Tim Li. Quantifying environmental control on tropical cyclone intensity change. *Monthly Weather Review*, 138(8):3243–3271, 2010.

[45] UC Mohanty, M Mohapatra, OP Singh, BK Bandyopadhyay, and LS Rathore. *Monitoring and prediction of tropical cyclones in the Indian Ocean and climate change*. Springer Science & Business Media, 2013.

[46] John Kaplan and Mark DeMaria. Large-scale characteristics of rapidly intensifying tropical cyclones in the North Atlantic basin. *Weather and forecasting*, 18(6):1093–1108, 2003.

[47] Kimberly M Wood and Elizabeth A Ritchie. A definition for rapid weakening of North Atlantic and eastern North Pacific tropical cyclones. *Geophysical Research Letters*, 42(22):10–091, 2015.

[48] Russell L Elsberry, Lianshou Chen, J Davidson, Robert Rogers, Yuqing Wang, and Liguang Wu. Advances in understanding and forecasting rapidly changing phenomena in tropical cyclones. *Trop. Cyclone Res. Rev*, 2:13–24, 2013.

[49] M Mohapatra, DR Sikka, BK Bandyopadhyay, and Ajit Tyagi. Outcomes and challenges of Forecast Demonstration Project (FDP) on landfalling cyclones over the Bay of Bengal. *Mausam*, 64:1–12, 2013.

[50] Scott A Braun, Ramesh Kakar, Edward Zipser, Gerald Heymsfield, Cerese Albers, Shannon Brown, Stephen L Durden, Stephen Guimond, Jeffery Halverson, Andrew Heymsfield, et al. NASA's Genesis and Rapid Intensification Processes (GRIP) field experiment. *Bulletin of the American Meteorological Society*, 94(3):345–363, 2013.

[51] Brian W Knosp, P Peggy Li, Quoc A Vu, Francis J Turk, Tsae-Pyng J Shen, Svetla M Hristova-Veleva, Stephen J Licata, and William L Poulsen. JPL genesis and rapid intensification processes (GRIP) portal. 2012.

[52] UC Mohanty, Krishna K Osuri, Vijay Tallapragada, Frank D Marks, Sujata Pattanayak, M Mohapatra, LS Rathore, SG Gopalakrishnan, and Dev Niyogi. A great escape from the bay of bengal super sapphire–phailin tropical cyclone: a case of improved weather forecast and societal response for disaster mitigation. *Earth Interactions*, 19(17):1–11, 2015.

[53] Vijay Tallapragada, Ligia Bernardet, Sundararaman Gopalakrishnan, Young Kwon, Qingfu Liu, Timothy Marchok, Dmitry Sheinin, Mingjing Tong, Samuel Trahan, Robert Tuleya, et al. Hurricane weather research and forecasting (hwrf) model: 2013 scientific documentation. *HWRF Development Testbed Center Tech. Rep*, 99, 2014.

[54] Daniel R Chavas and Kerry Emanuel. Equilibrium tropical cyclone size in an idealized state of axisymmetric radiative–convective equilibrium. *Journal of the Atmospheric Sciences*, 71(5):1663–1680, 2014.

[55] Thomas Frisius. What controls the size of a tropical cyclone? investigations with an axisymmetric model. *Quarterly Journal of the Royal Meteorological Society*, 141(691):2457–2470, 2015.

[56] Yoshio Kurihara, Morris A Bender, and Rebecca J Ross. An initialization scheme of hurricane models by vortex specification. *Monthly Weather review*, 121(7):2030–2045, 1993.

[57] Kerry A Emanuel, J David Neelin, and Christopher S Bretherton. On large-scale circulations in convecting atmospheres. *Quarterly Journal of the Royal Meteorological Society*, 120(519):1111–1143, 1994.

[58] Roger K Smith, Michael T Montgomery, and Hongyan Zhu. Buoyancy in tropical cyclones and other rapidly rotating atmospheric vortices. *Dynamics of atmospheres and oceans*, 40(3):189–208, 2005.

[59] Leon T Nguyen and John Molinari. Simulation of the downshear reformation of a tropical cyclone. *Journal of the Atmospheric Sciences*, 72(12):4529–4551, 2015.

[60] Paul D Reasor, Robert Rogers, and Sylvie Lorsolo. Environmental flow impacts on tropical cyclone structure diagnosed from airborne doppler radar composites. *Monthly Weather Review*, 141(9):2949–2969, 2013.

[61] Robert Rogers, Jun A Zhang, Jonathan Zawislak, Haiyan Jiang, George R Alvey III, Edward J Zipser, and Stephanie N Stevenson. Observations of the structure and evolution of hurricane edouard (2014) during intensity change. part ii: Kinematic structure and the distribution of deep convection. *Monthly Weather Review*, 144(9):3355–3376, 2016.

[62] Kristen L Corbosiero and John Molinari. The effects of vertical wind shear on the distribution of convection in tropical cyclones. *Monthly Weather Review*, 130(8):2110–2123, 2002.

[63] Jennifer C DeHart, Robert A Houze Jr, and Robert F Rogers. Quadrant distribution of tropical cyclone inner-core kinematics in relation to environmental shear. *Journal of the Atmospheric Sciences*, 71(7):2713–2732, 2014.

[64] Joshua B Wadler, Robert F Rogers, and Paul D Reasor. The relationship between spatial variations in the structure of convective bursts and tropical cyclone intensification as determined by airborne doppler radar. *Monthly Weather Review*, (2018), 2018.

[65] Kristen L Corbosiero and John Molinari. The relationship between storm motion, vertical wind shear, and convective asymmetries in tropical cyclones. *Journal of the Atmospheric Sciences*, 60(2):366–376, 2003.

[66] Eric D Rappin and David S Nolan. The effect of vertical shear orientation on tropical cyclogenesis. *Quarterly Journal of the Royal Meteorological Society*, 138(665):1035–1054, 2012.

[67] Lynn K Shay, Gustavo J Goni, and Peter G Black. Effects of a warm oceanic feature on hurricane Opal. *Monthly Weather Review*, 128(5):1366–1383, 2000.

[68] Benjamin Jaimes, Lynn K Shay, and Eric W Uhlhorn. Enthalpy and momentum fluxes during hurricane earl relative to underlying ocean features. *Monthly Weather Review*, 143(1):111–131, 2015.

[69] Jun A Zhang, Joseph J Cione, Evan A Kalina, Eric W Uhlhorn, Terry Hock, and Jeffrey A Smith. Observations of infrared sea surface temperature and air–sea interaction in hurricane edouard (2014) using gps dropsondes. *Journal of Atmospheric and Oceanic Technology*, 34(6):1333–1349, 2017.

[70] Joshua B Wadler, Jun A Zhang, Benjamin Jaimes, and Lynn K Shay. Downdrafts and the evolution of boundary layer thermodynamics in hurricane Earl (2010) before and during rapid intensification. *Monthly Weather Review*, (2018), 2018.

[71] Hua Chen and Sundararaman G Gopalakrishnan. A study on the asymmetric rapid intensification of hurricane earl (2010) using the HWRF system. *Journal of the Atmospheric Sciences*, 72(2):531–550, 2015.

[72] Rosimar Rios-Berrios and Ryan D Torn. Climatological analysis of tropical cyclone intensity changes under moderate vertical wind shear. *Monthly Weather Review*, 145(5):1717–1738, 2017.

[73] David R Ryglicki, James D Doyle, Yi Jin, Daniel Hodyss, and Joshua Cossuth. The unexpected rapid intensification of tropical cyclones in moderate vertical wind shear. part ii: Vortex tilt. *Monthly Weather Review*, (2018), 2018.

[74] David R Ryglicki, Joshua Cossuth, Daniel Hodyss, and James D Doyle. The unexpected rapid intensification of tropical cyclones in moderate vertical wind shear. part i: Overview and observations. *Monthly Weather Review*, (2018), 2018.

[75] TN Krishnamurti, Lydia Stefanova, and Vasubandhu Misra. Monsoons. In *Tropical Meteorology*, pages 75–119. Springer, 2013.

[76] D.S. Pai and S.C. Bhan. *Monsoon 2013: A report*. India Meteorological Department, 2013.

[77] Michael Riemer, Michael T Montgomery, and Melville E Nicholls. A new paradigm for intensity modification of tropical cyclones: thermodynamic impact of vertical wind shear on the inflow layer. *Atmospheric Chemistry & Physics*, 10(7), 2010.

[78] Paul D Reasor, Michael T Montgomery, and Lewis D Grasso. A new look at the problem of tropical cyclones in vertical shear flow: Vortex resiliency. *Journal of The Atmospheric sciences*, 61(1):3–22, 2004.

[79] Jun A Zhang, Robert F Rogers, Paul D Reasor, Eric W Uhlhorn, and Frank D Marks Jr. Asymmetric hurricane boundary layer structure from dropsonde composites in relation to the environmental vertical wind shear. *Monthly Weather Review*, 141(11):3968–3984, 2013.

[80] Michael Riemer and Michael T Montgomery. Simple kinematic models for the environmental interaction of tropical cyclones in vertical wind shear. *Atmospheric Chemistry and Physics*, 11(17):9395, 2011.

[81] John M Brown. Mesoscale unsaturated downdrafts driven by rainfall evaporation: A numerical study. *Journal of the Atmospheric Sciences*, 36(2):313–338, 1979.

[82] Brian Tang and Kerry Emanuel. Midlevel ventilations constraint on tropical cyclone intensity. *Journal of the Atmospheric Sciences*, 67(6):1817–1830, 2010.

[83] Brian Tang and Kerry Emanuel. Sensitivity of tropical cyclone intensity to ventilation in an axisymmetric model. *Journal of the Atmospheric Sciences*, 69(8):2394–2413, 2012.

[84] John Molinari, Jaclyn Frank, and David Vollaro. Convective bursts, downdraft cooling, and boundary layer recovery in a sheared tropical storm. *Monthly Weather Review*, 141(3):1048–1060, 2013.

[85] M Riemer, MT Montgomery, and ME Nicholls. Further examination of the thermodynamic modification of the inflow layer of tropical cyclones by vertical wind shear. *Atmospheric Chemistry & Physics*, 13:327–346, 2013.

[86] Leon T Nguyen, Robert F Rogers, and Paul D Reasor. Thermodynamic and kinematic influences on precipitation symmetry in sheared tropical cyclones: Bertha and cristobal (2014). *Monthly Weather Review*, 145(11):4423–4446, 2017.

[87] Roger K Smith and Michael T Montgomery. Toward clarity on understanding tropical cyclone intensification. *Journal of the Atmospheric Sciences*, 72(8):3020–3031, 2015.

[88] Jun A Zhang and Frank D Marks. Effects of horizontal diffusion on tropical cyclone intensity change and structure in idealized three-dimensional numerical simulations. *Monthly Weather Review*, 143(10):3981–3995, 2015.

[89] Lloyd J Shapiro and Huch E Willoughby. The response of balanced hurricanes to local sources of heat and momentum. *Journal of the Atmospheric Sciences*, 39(2):378–394, 1982.

[90] Michael T Montgomery and Roger K Smith. Paradigms for tropical cyclone intensification. *Australian Meteorological and Oceanographic Journal*, 64:37–66, 2014.

[91] Daniel P Stern, Jonathan L Vigh, David S Nolan, and Fuqing Zhang. Revisiting the relationship between eyewall contraction and intensification. *Journal of the Atmospheric Sciences*, 72(4):1283–1306, 2015.

[92] Jonathan L Vigh and Wayne H Schubert. Rapid development of the tropical cyclone warm core. *Journal of the Atmospheric Sciences*, 66(11):3335–3350, 2009.

[93] Yoshiaki Miyamoto and Tetsuya Takemi. A triggering mechanism for rapid intensification of tropical cyclones. *Journal of the Atmospheric Sciences*, 72(7):2666–2681, 2015.

[94] TN Krishnamurti, Anu Simon, Mrinal Kanti Biswas, and Christopher Davis. Impacts of cloud flare-ups on hurricane intensity resulting from departures from balance laws. *Tellus A: Dynamic Meteorology and Oceanography*, 64(1):18399, 2012.

[95] Yoshio Kurihara. On the development of spiral bands in a tropical cyclone. *Journal of the Atmospheric Sciences*, 33(6):940–958, 1976.

[96] Christopher S Bretherton and Piotr K Smolarkiewicz. Gravity waves, compensating subsidence and detrainment around cumulus clouds. *Journal of the Atmospheric Sciences*, 46(6):740–759, 1989.

[97] Yuqing Wang. Vortex Rossby waves in a numerically simulated tropical cyclone. part ii: The role in tropical cyclone structure and intensity changes. *Journal of the Atmospheric sciences*, 59(7):1239–1262, 2002.

[98] PH Haynes and ME McIntyre. On the evolution of vorticity and potential vorticity in the presence of diabatic heating and frictional or other forces. *Journal of the Atmospheric Sciences*, 44(5):828–841, 1987.

[99] DJ Raymond and CL Carrillo. The vorticity budget of developing typhoon nuri (2008). *Atmospheric Chemistry and Physics*, 11(1):147–163, 2011.

[100] David J Raymond, Saška Gjorgjievska, Sharon Sessions, and Zeljka Fuchs. Tropical cyclogenesis and mid-level vorticity. *Aust. Meteorol. Oceanogr. J*, 64:11–25, 2014.

[101] Barry Saltzman. Equations governing the energetics of the larger scales of atmospheric turbulence in the domain of wave number. *Journal of Meteorology*, 14(6):513–523, 1957.

[102] Richard A Anthes and Donald R Johnson. Generation of available potential energy in hurricane hilda. *Monthly Weather Review*, 96(5), 1968.

[103] Roger K Smith and Michael T Montgomery. The efficiency of diabatic heating and tropical cyclone intensification. *Quarterly Journal of the Royal Meteorological Society*, 142(698):2081–2086, 2016.

[104] Roland B Stull. *An introduction to boundary layer meteorology*, volume 13. Springer Science & Business Media, 2012.

[105] Andrej Nikolaevich Kolmogorov. On the degeneration of isotropic turbulence in an incompressible viscous fluid. In *Dokl. Akad. Nauk SSSR*, volume 31, pages 319–323, 1941.

[106] David Byrne and Jun A Zhang. Height-dependent transition from 3-d to 2-d turbulence in the hurricane boundary layer. *Geophysical Research Letters*, 40(7):1439–1442, 2013.

[107] Gerald B Smith and Michael T Montgomery. Vortex axisymmetrization: Dependence on azimuthal wave-number or asymmetric radial structure changes. *Quarterly Journal of the Royal Meteorological Society*, 121(527):1615–1650, 1995.

[108] J Dominique Möller and Michael T Montgomery. Vortex rossby waves and hurricane intensification in a barotropic model. *Journal of the atmospheric sciences*, 56(11):1674–1687, 1999.

[109] John Molinari and David Vollaro. External influences on hurricane intensity. part i: Outflow layer eddy angular momentum fluxes. *Journal of the Atmospheric Sciences*, 46(8):1093–1105, 1989.

[110] John Molinari and David Vollaro. External influences on hurricane intensity. part ii: Vertical structure and response of the hurricane vortex. *Journal of the Atmospheric sciences*, 47(15):1902–1918, 1990.

[111] John Molinari, Steven Skubis, and David Vollaro. External influences on hurricane intensity. part iii: Potential vorticity structure. *Journal of the Atmospheric sciences*, 52(20):3593–3606, 1995.

[112] Kieran T Bhatia and David S Nolan. Relating the skill of tropical cyclone intensity forecasts to the synoptic environment. *Weather and Forecasting*, 28(4):961–980, 2013.

[113] Kerry Emanuel, Christopher DesAutels, Christopher Holloway, and Robert Korty. Environmental control of tropical cyclone intensity. *Journal of the Atmospheric sciences*, 61(7):843–858, 2004.

[114] Falko Judt, Shuyi S Chen, and Judith Berner. Predictability of tropical cyclone intensity: scale-dependent forecast error growth in high-resolution stochastic kinetic-energy backscatter ensembles. *Quarterly Journal of the Royal Meteorological Society*, 142(694):43–57, 2016.

[115] John Kaplan, Mark DeMaria, and John A Knaff. A revised tropical cyclone rapid intensification index for the atlantic and eastern north pacific basins. *Weather and forecasting*, 25(1):220–241, 2010.

[116] Christopher M Rozoff, Christopher S Velden, John Kaplan, James P Kossin, and Anthony J Wimmers. Improvements in the probabilistic prediction of tropical cyclone rapid intensification with passive microwave observations. *Weather and Forecasting*, 30(4):1016–1038, 2015.

[117] John Kaplan and Mark DeMaria. A simple empirical model for predicting the decay of tropical cyclone winds after landfall. *Journal of applied meteorology*, 34(11):2499–2512, 1995.

[118] Haiyan Jiang. The relationship between tropical cyclone intensity change and the strength of inner-core convection. *Monthly Weather Review*, 140(4):1164–1176, 2012.

[119] Margaret E Kieper and Haiyan Jiang. Predicting tropical cyclone rapid intensification using the 37 ghz ring pattern identified from passive microwave measurements. *Geophysical Research Letters*, 39(13), 2012.

[120] Robert Rogers, Paul Reasor, and Sylvie Lorsolo. Airborne doppler observations of the inner-core structural differences between intensifying and steady-state tropical cyclones. *Monthly Weather Review*, 141(9):2970–2991, 2013.

[121] Bo Yang, Yuqing Wang, and Bin Wang. The effect of internally generated inner-core asymmetries on tropical cyclone potential intensity. *Journal of the Atmospheric sciences*, 64(4):1165–1188, 2007.

[122] Rosimar Rios-Berrios, Tomislava Vukicevic, and Brian Tang. Adopting model uncertainties for tropical cyclone intensity prediction. *Monthly Weather Review*, 142(1):72–78, 2014.

[123] Kerry Emanuel and Fuqing Zhang. On the predictability and error sources of tropical cyclone intensity forecasts. *Journal of the Atmospheric Sciences*, 73(9):3739–3747, 2016.

[124] ZHAN Zhang and TN Krishnamurti. A perturbation method for hurricane ensemble predictions. *Monthly Weather Review*, 127(4):447–469, 1999.

[125] Tomislava Vukicevic, Eric Uhlhorn, Paul Reasor, and Bradley Klotz. A novel multiscale intensity metric for evaluation of tropical cyclone intensity forecasts. *Journal of the Atmospheric Sciences*, 71(4):1292–1304, 2014.

[126] Ronald A Fisher. The use of multiple measurements in taxonomic problems. *Annals of eugenics*, 7(2):179–188, 1936.

[127] Mark DeMaria. The effect of vertical shear on tropical cyclone intensity change. *Journal of the Atmospheric sciences*, 53(14):2076–2088, 1996.

[128] Martin LM Wong and Johnny CL Chan. Tropical cyclone intensity in vertical wind shear. *Journal of the Atmospheric sciences*, 61(15):1859–1876, 2004.

[129] William J Randel and Mijeong Park. Deep convective influence on the asian summer monsoon anticyclone and associated tracer variability observed with atmospheric infrared sounder (airs). *Journal of Geophysical Research: Atmospheres*, 111(D12), 2006.

[130] A Arriaga. Technical memorandum no. 5: Microwave humidity sounder (mhs) simulations with a radiative transfer model. Technical report, EUMETSAT technical report, 2000.

[131] Hartmut H Aumann and Robert J Pagano. Atmospheric infrared sounder on the earth observing system. *Optical Engineering*, 33(3):776–785, 1994.

[132] F Weng, X Zou, X Wang, S Yang, and MD Goldberg. Introduction to suomi national polar-orbiting partnership advanced technology microwave sounder for numerical weather prediction and tropical cyclone applications. *Journal of Geophysical Research: Atmospheres*, 117(D19), 2012.

[133] ER Kursinski, GA Hajj, JT Schofield, RP Linfield, and K Rer Hardy. Observing earth's atmosphere with radio occultation measurements using the global positioning system. *Journal of Geophysical Research: Atmospheres*, 102(D19):23429–23465, 1997.

[134] Kristopher M Bedka and John R Mecikalski. Application of satellite-derived atmospheric motion vectors for estimating mesoscale flows. *Journal of applied meteorology*, 44(11):1761–1772, 2005.

[135] David W Draper, David A Newell, Frank J Wentz, Sergey Krimchansky, and Gail M Skofronick-Jackson. The global precipitation measurement (gpm) microwave imager (gmi): Instrument overview and early on-orbit performance. *IEEE Journal of Selected Topics in Applied Earth Observations and Remote Sensing*, 8(7):3452–3462, 2015.

[136] Roy W Spencer, Robbie E Hood, Frank J Lafontaine, Eric A Smith, Robert Platt, Joe Galliano, Vanessa L Griffin, and Elena Lobl. High-resolution imaging of rain systems with the advanced microwave precipitation radiometer. *Journal of Atmospheric and Oceanic Technology*, 11(4):849–857, 1994.

[137] Ninghai Sun and Fuzhong Weng. Evaluation of special sensor microwave imager/sounder (ssmis) environmental data records. *IEEE Transactions on Geoscience and Remote Sensing*, 46(4):1006–1016, 2008.

[138] SM Hristova-Veleva, PS Callahan, RS Dunbar, BW Stiles, SH Yueh, JN Huddleston, SV Hsiao, G Neumann, BA Vanhoff, RW Gaston, et al. Revealing the winds under the rain. part i: Passive microwave rain retrievals using a new observation-based parameterization of subsatellite rain variability and intensityalgorithm description. *Journal of Applied Meteorology and Climatology*, 52(12):2828–2848, 2013.

[139] J Figa-Saldaña, J JW Wilson, E Attema, R Gelsthorpe, MR Drinkwater, and A Stoffelen. The advanced scatterometer (ascat) on the meteorological operational (metop) platform: A follow on for european wind scatterometers. *Canadian Journal of Remote Sensing*, 28(3):404–412, 2002.

[140] E Rodriguez and SM Hristova-Veleva. Multidecadal consistent ocean vector winds: From QuikSCAT to RapidScat and beyond. In *AGU Fall Meeting Abstracts*, 2014.

[141] Edward N Lorenz. The predictability of a flow which possesses many scales of motion. *Tellus*, 21(3):289–307, 1969.

[142] Edward N Lorenz. Irregularity: A fundamental property of the atmosphere. *Tellus A*, 36(2):98–110, 1984.

[143] Judith Berner, S-Y Ha, JP Hacker, Aime Fournier, and C Snyder. Model uncertainty in a mesoscale ensemble prediction system: Stochastic versus multiphysics representations. *Monthly Weather Review*, 139(6):1972–1995, 2011.

[144] Fuqing Zhang and Dandan Tao. Effects of vertical wind shear on the predictability of tropical cyclones. *Journal of the Atmospheric Sciences*, 70(3):975–983, 2013.

[145] Falko Judt and Shuyi S Chen. Predictability and dynamics of tropical cyclone rapid intensification deduced from high-resolution stochastic ensembles. *Monthly Weather Review*, 144(11):4395–4420, 2016.

[146] Peter M Finocchio and Sharanya J Majumdar. The predictability of idealized tropical cyclones in environments with time-varying vertical wind shear. *Journal of Advances in Modeling Earth Systems*, 9(8):2836–2862, 2017.

[147] TSV Vijaya Kumar, TN Krishnamurti, Michael Fiorino, and Masashi Nagata. Multimodel superensemble forecasting of tropical cyclones in the pacific. *Monthly Weather Review*, 131(3):574–583, 2003.

[148] Crawford S Holling. Resilience and stability of ecological systems. *Annual review of ecology and systematics*, 4(1):1–23, 1973.

[149] Carl Folke, Stephen R Carpenter, Brian Walker, Marten Scheffer, Terry Chapin, and Johan Rockström. Resilience thinking: integrating resilience, adaptability and transformability. *Ecology and society*, 15(4), 2010.

[150] Jeryang Park, Thomas P Seager, P S C Rao, Matteo Convertino, and Igor Linkov. Integrating risk and resilience approaches to catastrophe management in engineering systems. *Risk Analysis*, 33(3):356–367, 2013.

[151] Beatrix E Beisner, Daniel T Haydon, and Kim Cuddington. Alternative stable states in ecology. *Frontiers in Ecology and the Environment*, 1(7):376–382, 2003.

[152] Marten Scheffer, Stephen R Carpenter, Timothy M Lenton, Jordi Bascompte, William Brock, Vasilis Dakos, Johan Van de Koppel, Ingrid A Van de Leemput, Simon A Levin, Egbert H Van Nes, et al. Anticipating critical transitions. *science*, 338(6105):344–348, 2012.

[153] Jeryang Park and P Suresh C Rao. Regime shifts under forcing of non-stationary attractors: Conceptual model and case studies in hydrologic systems. *Journal of contaminant hydrology*, 169:112–122, 2014.

VITA

I am currently a doctoral student at the Department of Earth, Atmospheric, and Planetary Sciences, Purdue University. Prior to my doctoral stint, I received my Masters in Fluid Mechanics from Imperial College London, and my Bachelors in Mechanical Engineering from SASTRA University in India. I will shortly begin a post-doctoral stint at the Department of Earth System Science, Stanford University.

During my stint at Purdue, I received the Lynn fellowship, the NASA Earth Science Fellowship and the Bilsland Dissertation Fellowship. This research work has been published as five first-author articles in Geophysical Research Letters, Remote Sensing and Modeling of the Atmospheres, Oceans, and Interactions, Scientific Reports, Earth and Space Science, and the Journal of the Atmospheric Sciences. My work was presented in several international conferences, and in national labs and academic institutions as invited presentations.

An up to date vita can be found directly on my website:
`https://sites.google.com/view/saiprasanth/` and my publications can be accessed from my Google Scholar page:
`https://scholar.google.com/citations?user=tIUQDyUAAAAJ&hl=en`